Instrument Development and Plasma Measurements on a 200-Watt Hall Thruster Plume

by

Yassir Azziz

S.B., Aeronautics and Astronautics
Massachusetts Institute of Technology, 2001

SUBMITTED TO THE DEPARTMENT OF AERONAUTICS AND ASTRONAUTICS
IN PARTIAL FULFILLMENT OF THE REQUIREMENTS FOR THE DEGREE OF

MASTER OF SCIENCE IN AERONAUTICS AND ASTRONAUTICS

at the

MASSACHUSETTS INSTITUTE OF TECHNOLOGY

September 2003

Signature of Author . . . . . .
Department of Aeronautics and Astronautics
June 13, 2003

Certified by . . . . . .
Manuel Martinez-Sanchez
Professor of Aeronautics and Astronautics
Thesis Supervisor

Accepted by . . . . . .
Edward M. Greitzer
H. N. Slater Professor of Aeronautics and Astronautics
Chair, Committee on Graduate Students

Instrument Development and Plasma Measurements on a 200-Watt Hall Thruster Plume

by

Yassir Azziz

Submitted to the Department of Aeronautics and Astronautics
on June 13, 2003, in Partial Fulfillment of the
Requirements for the Degree of
Master of Science in Aeronautics and Astronautics

ABSTRACT

Plume diagnostic instruments were developed and the BHT-200 Hall thruster plume was characterized in order to support ongoing computational plume models. The instruments included a Faraday probe to measure current density, a hot emissive probe to measure plasma potential, and a cold Langmuir probe to measure electron temperature and electron density. Plasma measurements consisted of studying facility and thruster effects on the plume. Facility effects included background pressure and sweep radius, while thruster effects included discharge voltage and flow rate. Experimental results showed that current density is more sensitive to background pressure than to thruster effects, plasma potential is a more direct indicator of plasma density than current flux, and electron temperature and electron density vary substantially across the plume following a polytropic relationship. These experimental results were compared to solutions of a self-similar plume model. Data analyses were also performed using a consistency analysis of the experimental data by deducing plasma potential from Faraday and cold emissive probe data and comparing it to the measured plasma potential from the hot emissive probe. Good agreement was achieved between all experimental data and analysis except in charge exchange dominated regions, since the analyses do not take into account collision effects. Thus, the experimental data obtained can be used to validate computational results.

Thesis Supervisor: Manuel Martinez-Sanchez
Title: Professor of Aeronautics and Astronautics

ACKNOWLEDGMENTS

I would like to express my sincere and utmost gratitude to my advisor, Professor Manuel Martinez-Sanchez, who has provided me with outstanding guidance. He has been an invaluable resource throughout my research at MIT.

Special thanks to the electric propulsion team at Busek – Bruce, George, and Larry for their help with my research.

I also would like to thank everyone in SPL – Noah, Shannon, Paulo, Jorge, and Mark, you have all shared in my ups and downs and have played a positive and integral role in my experience here. Thank you for making SPL a fun place to work.

This thesis is dedicated to my mother and father, I owe them my best attributes for they have always supported me in all of my endeavors and had complete understanding of my responsibilities, despite my inability to spend as much time with them as I would like to. Also, to my brother, Issam, and my sisters Ilhame, Amal, and Samia who have shared with me all my goals and dreams and have provided me with invaluable advice. To Ania for her faith and confidence in me.

TABLE OF CONTENTS

LIST OF FIGURES

LIST OF TABLES

NOMENCLATURE

a	$4x10^5$ A/m^2/K^2
A_{en}	Area of encapsulated portion of the probe
A_f	Filament area
A_p	Probe collector area
$\underline{c}$	$4.2x10^9$ $(\Omega\,mk)^{-1}$
c_e	Electron thermal velocity
$\dot{\delta}$	Rate of deposition
D_c	Collector diameter
D_f	Filament diameter
D_r	Guard ring outside diameter
e	Electron charge
ε_o	Permittivity of vacuum $8.854x10^{-12}$ F/m
ε_i	$6.3x10^{-6}$ K$^{-3/2}$
F	Frequency
γ	Ratio of C_p to C_v
I	Current
I_b	Beam current
I_e	Electron current
I_{em}	Current due to electron emission
I_i	Ion current
I_{sp}	Specific impulse
j	Current density
j_c	Measured current density at centerline
k	Boltzmann constant
k_{th}	Thermal conduction of current
λ_D	Debye length
L_{en}	Length of encapsulated portion of probe
L_f	Filament length
$\dot{m}$	Flow rate
m_e	Electron mass
m_i	Ion mass
n_e	Electron density
η_t	Efficiency
P_b	Base pressure
P_c	Corrected pressure
P_i	Indicated pressure
ϕ	Potential
ϕ_c	Plasma potential at centerline
ϕ_p	Plasma potential
$\Delta\phi$	Difference between probe voltage and plasma potential V_{probe}-ϕ_{plasma}

Q_c	Heat conduction
Q_e	Electron collection heating
Q_{em}	Electron emission cooling
Q_i	Ion collection heating
Q_{oh}	Ohmic heating
Q_{rad}	Radiation cooling
r	Sweep radius
R	Shunt resistance
S_f	Crystal sensitivity
σ_B	5.67×10^{-8} W/m^2/K^2
T	Thrust
T_e	Electron temperature
T_f	Filament temperature
T_i	Ion temperature
T_o	Wall temperature
t	Time
t_r	Wall thickness
t_s	Spacing between collector and cylinder
τ	Film thickness
θ	Angular position
θ'	Half-angle plume divergence
$\theta_{1/2}$	Angle where plasma density falls to half centerline value
V	Voltage
V_D	Discharge voltage
V_{probe}	Probe potential
v_i	Ion velocity
$*$	Reference state
ψ	Material work function

Chapter 1

INTRODUCTION

1.1 Hall Thrusters

1.1.1 Concept

Electric propulsion systems are an attractive alternative to chemical propulsion devices on board satellites. Currently, in-orbit satellites use chemical propulsion for orbit control and guidance. These chemical propulsion systems require large quantities of propellants, which increase the weight of the payload and the cost of the mission. To address these limitations, electric propulsion systems were investigated and used on in-orbit satellites. These systems require less propellant and have enough power to control and guide the satellite. Electric propulsion systems include Hall thrusters, ion engines, and MPD thrusters.

A Hall thruster is an axisymmetric device in which plasma is created in an annular channel, as shown in Figure 1.1. The propellants used in Hall thrusters are noble gases such as xenon, argon, or krypton. Xenon is usually utilized due to its high molecular weight and low ionization potential. Inner and outer magnetic poles in the annular channel establish a radial magnetic field, whereas the anode, located at the back of the thruster, and the external cathode create an axial electric field.

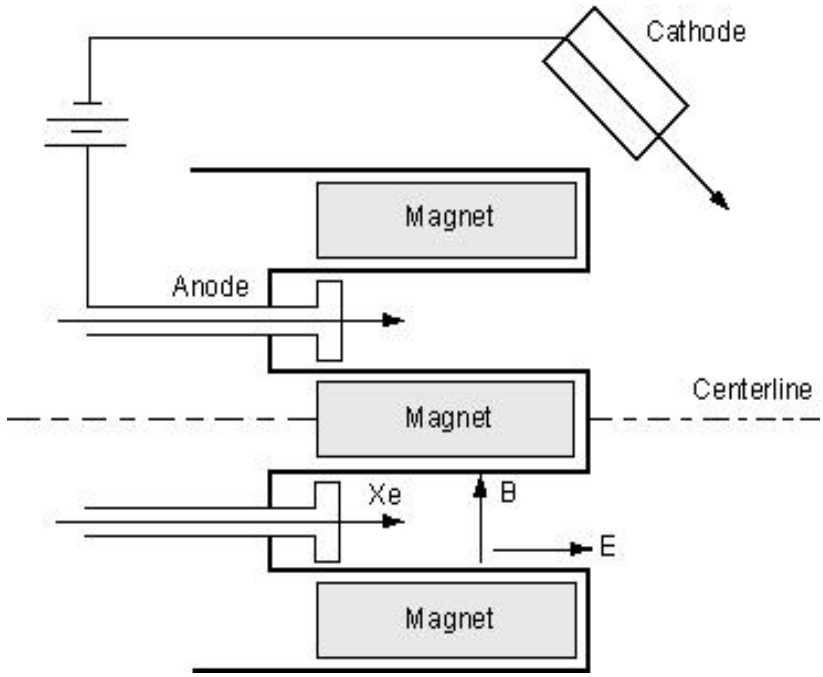

Figure 1.1 Cross-section of a Hall thruster.

Thrust is generated through electrostatic acceleration of ions. Electrons are first emitted from the external cathode and accelerated by the electric field backwards toward the anode. However, due to their small Larmor radius, electrons are trapped by the magnetic field and azimuthally drift along the magnetic field lines. Xenon, which is injected at the anode, is ionized through collisions with trapped electrons. These xenon ions, unaffected by the magnetic field due to their large Larmor radius, are axially accelerated out of the thruster by the electric field. When the electrons execute free drift, the electrostatic pull of the anode is balanced by the magnetic pressure of the magnets, resulting in a zero net force on the electrons, and leaving the electrostatic force on ions as the only source of thrust.

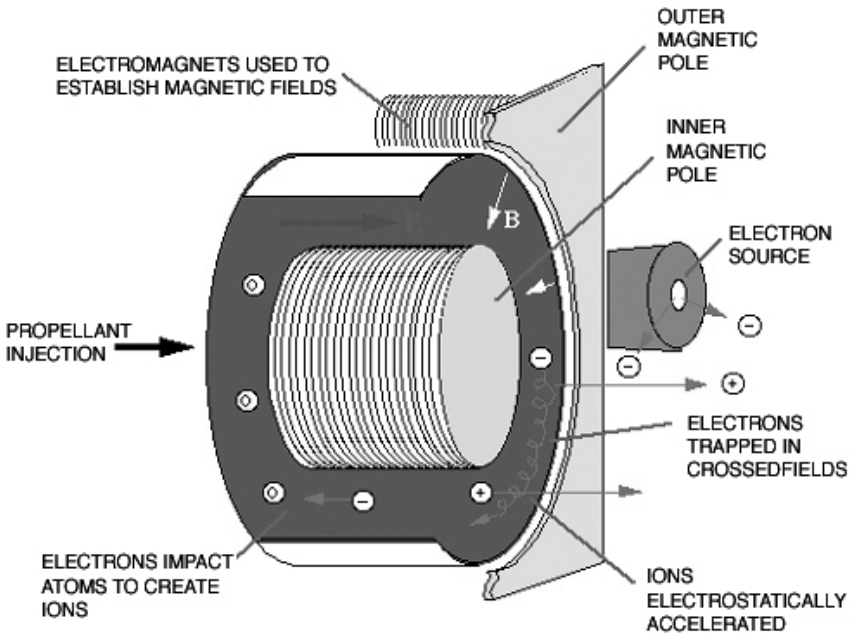

Figure 1.2 Hall thruster concept diagram.

1.1.2 Advantages

Hall thrusters offer several advantages over other propulsion systems. For example, Hall thrusters offer a wide range of thrust capabilities and generally operate at a greater than 50% thrust efficiency. Also, their capacity to deliver a high specific impulse of 1600 sec and a high thrust to power ratio of 60 mN/kW, establishes a system that provides both fuel efficiency and optimal trip time [6]. Furthermore, their simplistic design, which does not include grids as in ion engines, reduces the sputtering of materials from the thruster and enables them to operate at reasonable voltages. Hall thrusters also have a wide range of applications, including LEO satellite constellations and small Earth-orbiting satellites. Combined, these advantages make Hall thrusters an attractive alternative to conventional chemical propulsion devices.

1.1.3 Issues

Although Hall thrusters offer many advantages, several issues need to be addressed in order to successfully implement Hall thrusters on board spacecrafts. One of these issues regards the Hall thruster plume interactions with the spacecraft. Hall thruster plumes primarily consist of electrons, high energy source ions, and low energy charge exchange ions. These particles can interact with and subsequently damage the spacecraft. For example, high energy ions can impact the surface of the spacecraft resulting in material erosion. In turn, this sputtered material can contaminate solar arrays and other sensitive surfaces. Also, low energy charge exchange ions can flow back to the spacecraft and alter its potential. Plume impingement on solar arrays can result in thrust loss and torque perturbation, causing a change in spacecraft attitude. In addition, plume optical emission can interfere with sensitive optical instruments and the plume electromagnetic field can lead to distortion of communication signals. Figure 1.3 summarizes the interactions of a Hall thruster plume with spacecraft components.

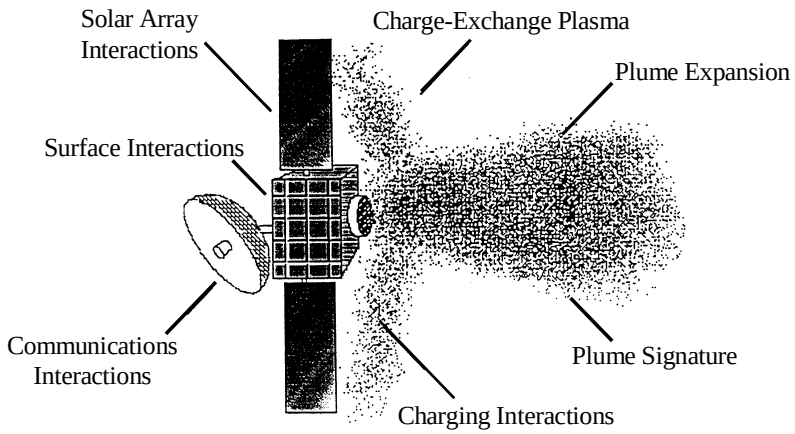

Figure 1.3 Plume-spacecraft interactions.

1.2 Status of Hall Thruster Plume Research

The concept of a Hall thruster was first envisioned in the United States [2, 8]. However, it was in the former Soviet Union where the Hall thruster concept was successfully implemented as a propulsion device. A. I. Morozov was the lead scientist on this endeavor, and through his efforts, Hall thrusters transitioned from a laboratory experimental device to a propulsion system used on Soviet satellites [12].

Both experimental and computational research have been conducted to resolve issues pertaining to Hall thruster plume interactions with the spacecraft. This research helps increase the physical understanding of the plume, allowing better integration of the Hall thruster with the spacecraft.

D. Oh, for example, developed a hybrid PIC-DSMC three-dimensional simulation to characterize a Hall thruster plume. His computational model investigates the expansion of partially ionized plasma in three dimensions and its interaction with surfaces. He concluded that the plume is unmagnetized and is a quasi neutral plasma in which charge exchange collisions have a dominant negative effect [13].

On the other hand, several experiments have been conducted to study the Hall thruster plume. These efforts were led by both industry and academia, and have been documented in several publications [1, 4, 15]. In these experiments, many instruments were used for mapping the Hall thruster plume, including retarding potential analyzers, Faraday cups, and Langmuir probes. However, no standard design for these instruments exists, and thus the ability to compare data among various research groups is compromised. Additionally, variations between experimental facilities in which the research is conducted adds further complexity for data comparison.

Plume interaction with the spacecraft remains an important issue despite the considerable flight heritage of Hall thrusters. The results obtained from both experiments and computational models increase understanding of plume expansion in relation to the spacecraft.

However, in-flight experience data characterizing Hall thruster plumes in the space environment, without the presence of facility artifacts, is necessary to accurately predict plume effects. This is useful to optimize thruster location in the satellite in order to prevent damage from the plume.

1.3 Motivation and Objectives

The first objective of this research is to develop and test plume diagnostic instruments. The instruments include a Faraday probe to measure current density, an emissive probe to measure plasma potential, and a Langmuir probe to measure electron temperature and electron density. The design requirements consist of miniaturizing the probes to a millimeter scale and ensuring measurement repeatability within a 10% range. Miniature probes minimize plasma perturbations and provide better measurement resolution, which is especially important for small thrusters, such as the BHT-200 used in this work.

The second objective of this research is to map the plume of the BHT-200 Hall thruster. Experiments are conducted to characterize facility and Hall thruster effects on the plume. Facility effects include background pressure and sweep radius, while thruster effects include discharge voltage and flow rate. These experiments will in turn increase physical understanding of the BHT-200 Hall thruster plume.

To verify the experimental results, several analyses are conducted. Analyses include performing a consistency study between current density and plasma potential and between electron density and plasma potential. Also, a comparison of the experimental results to the self-similar model is conducted. The validation of these experimental results will establish a database of measurements to support ongoing computational models.

1.4 Thesis Outline

Chapter 2 provides a general overview of several plume diagnostic instruments. Chapter 3 then presents a detailed description of Faraday probe design and its experimental setup. The results of the Faraday probe measurements are discussed in Chapter 4. Similarly, Chapter 5 provides a detailed description on emissive probe design and its experimental setup, and Chapter 6 presents the results of emissive probe measurements. Chapter 7 discusses a consistency study between current density and plasma potential and between electron density and plasma potential. It also presents a comparison of the experimental results to self-similar model solutions. A detailed description of the BHT-200 thruster, as well as performance measurements, are shown in Appendix A. Appendix B presents design and testing of other Faraday probes that were unsuccessful. Finally, a detailed derivation of the self-similar solutions is described in Appendix C.

Chapter 2

OVERVIEW OF PLUME DIAGNOSTIC INSTRUMENTS

A plume is an unmagnetized quasi-neutral plasma primarily composed of electrons, single ions, Xe^{+}, double ions, Xe^{++}, and neutral particles. To fully understand the dynamics of plume components, various diagnostic experiments have been performed by researchers [5, 15]. These tests involved measurement of plasma potential, electron temperature and density, current density distribution, ion energy distribution, and particle deposition. Due to the inability of a single instrument to fully characterize the plume, different instruments were used to measure specific plume parameters. In this chapter, several instruments are introduced to provide an overview of plume diagnostics, including a Langmuir probe, an emissive probe, a Faraday probe, a retarding potential analyzer, and a quartz crystal microbalance. Of the instruments described in this chapter, only the Faraday, Langmuir, and emissive probes were used in this research.

2.1 Langmuir Probe

A Langmuir probe is a diagnostic instrument that is used to measure electron temperature, electron density, floating potential, and plasma potential. It consists of a single wire, usually tungsten, inside a single-bore alumina tube, as shown in Figure 2.1. Due to the small amount of metal that is inserted in the plasma, only minor plasma perturbations are caused. The probe is connected to a power supply and its potential is swept over negative and positive values with respect to the plasma potential. For each applied voltage, a cur-

rent is measured, yielding a current-voltage (I-V) characteristic curve. Electron temperature, electron density, floating potential, and plasma potential are deduced from the I-V curve using classic Langmuir probe theory [7], which assumes a stationary plasma and a thin sheath. The general appearance of the I-V characteristic curve in stationary plasma is shown in Figure 2.1.

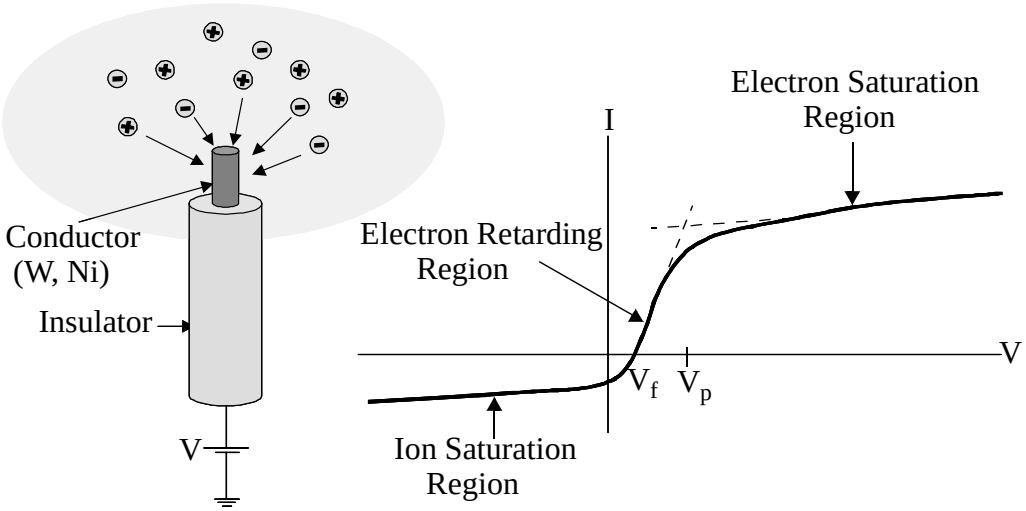

Figure 2.1 Schematic of a Langmuir probe and general appearance of the I-V characteristic curve in stationary plasma. V is measured with respect to the vacuum tank walls, which are at a generally unknown potential (usually negative) with respect to the plasma.

The current collected by the probe is the sum of electron and ion currents. When net current is zero, the applied voltage to the probe is known as the floating potential and is smaller than the plasma potential. When the probe is sufficiently negatively biased, all electrons are repelled and the ions are accelerated towards the probe. The current collected by the probe attains a nearly constant value, which is termed the ion saturation current.

As the applied voltage is increased past the floating potential, ions and high energy electrons are collected. Most of the electrons, however, are repelled and only the high energy electrons are able to travel down the potential gradient to be collected by the probe, resulting in positive current. This is termed the electron retarding regime. The inverse slope of

the logarithmic plot of the electron retarding regime provides the electron temperature using

$$\frac{d\ln I}{dV} = \frac{e}{kT_e} \tag{2.1}$$

where e is electron charge, k is Boltzmann's constant, and T_e is electron temperature.

When the probe is biased at high positive potentials, ions are repelled and electrons are accelerated towards the probe. The current collected by the probe attains a nearly constant value, called the electron saturation current. The intersection point of the tangents to the electron retarding regime and the electron saturation current provides the plasma potential.

Another plasma parameter that can be deduced from the I-V characteristic curve is the electron density, n_e, which is determined by

$$(I_e)_{sat} = \frac{1}{4} A_p e n_e \sqrt{\frac{8kT_e}{\pi m_e}} \tag{2.2}$$

where I_e is the electron saturation current, A_p is the area of the probe, n_e is electron density, and m_e is the mass of electron. In practice, electron current does not really saturate, due to growth of the sheath with voltage, and one uses in equation (2.2) the electron current at the plasma potential instead [7]. The presence of flow brings additional complications because the wake portion of the probe does not collect current, as shown in Figure 2.2. Therefore, the true collecting area is difficult to estimate accurately.

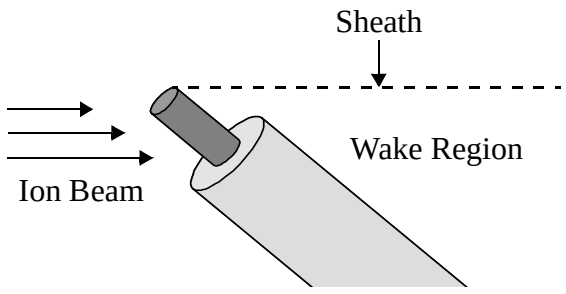

Figure 2.2 Langmuir probe in flowing plasma.

Figure 2.3 shows a schematic of a real probe characteristic when the plasma density is low enough to invalidate the thin-sheath analysis. A linear growth of electron current beyond the plasma potential reflects a 3D Orbital Motion Limit (OML) regime. A square-root growth would instead reflect a 2D OML regime [4].

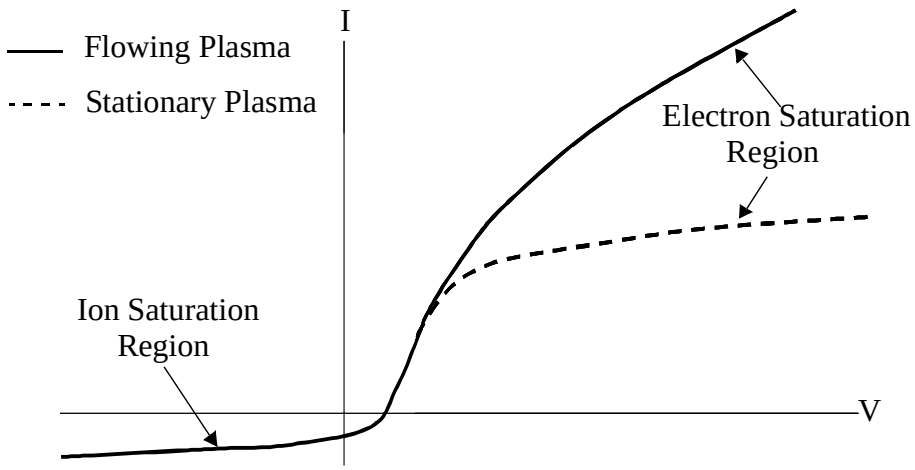

Figure 2.3 Comparison of the I-V characteristic curve in a stationary and flowing plasma.

2.2 Emissive Probe

An emissive probe is a diagnostic instrument that only measures plasma potential. It consists of a small loop of tungsten wire in a double-bore ceramic tube, as shown in Figure 2.4. The tungsten wire, in this research, is 125μm in diameter with 6 mm of exposed filament in the plasma. This small amount of metal causes only minor plasma perturbations.

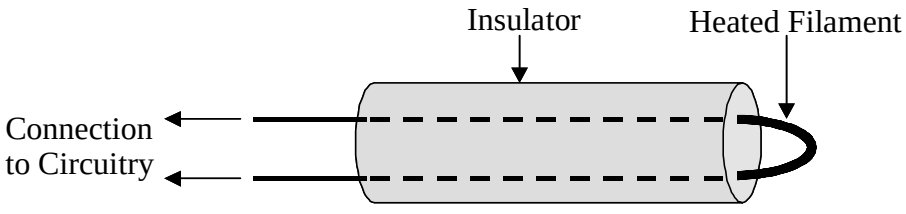

Figure 2.4 Schematic of an emissive probe.

The tungsten filament is heated by an external current source to initiate the emission of electrons. Since electrons travel up potential gradients, emission only occurs when the probe is biased negatively with respect to the plasma potential. In the electron saturation regime, the emissive probe behaves similarly to a Langmuir probe because no emission occurs. Figure 2.5 is a schematic of the emissive probe concept.

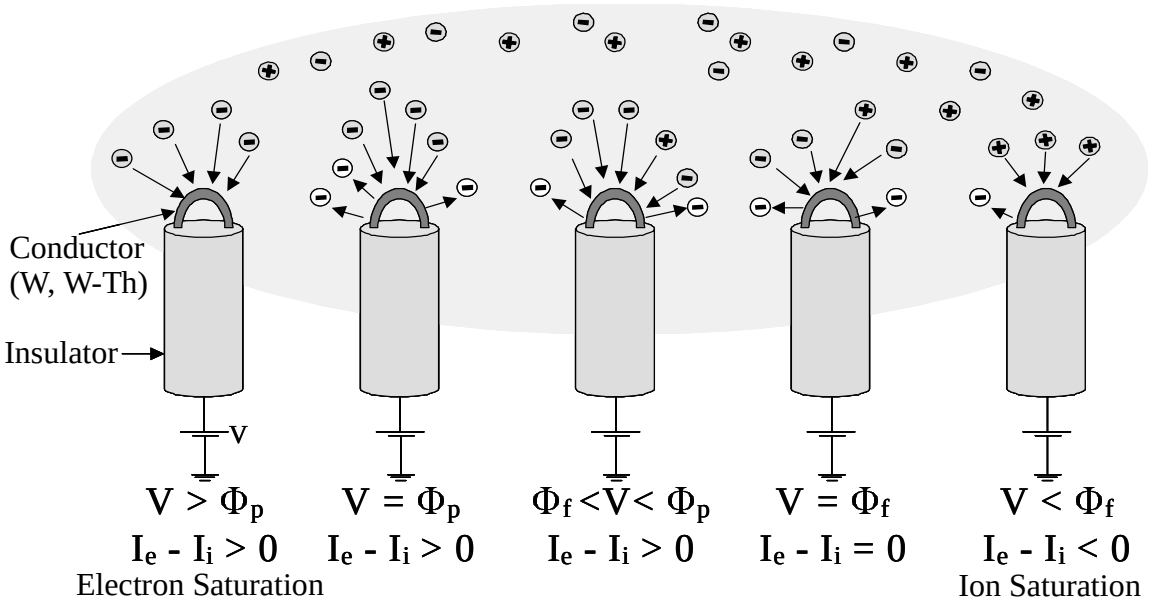

Figure 2.5 Emissive probe concept.

The I-V characteristic curve of the emissive probe is the same as the I-V characteristic curve of a Langmuir probe when the probes are biased positively with respect to the plasma potential. As the emissive probe potential is biased negatively, electron emission occurs in an amount depending on filament temperature, which leads to a sharp drop in collected current in the electron retarding regime. This phenomenon does not happen in a Langmuir probe because the tungsten filament is not hot enough to incite electron emission. Thus, Langmuir probes are commonly referred to as “cold probes,” whereas emissive probes are referred to as “hot probes.” A distinct “knee” is more noticeable in the I-V curve of the emissive probe than of the Langmuir probe, as shown in Figure 2.6. The volt-

age at which the “knee” occurs corresponds to the plasma potential. This technique, which consists of directly determining the plasma potential from the I-V curve of the emissive probe, is called the inflection point method [17].

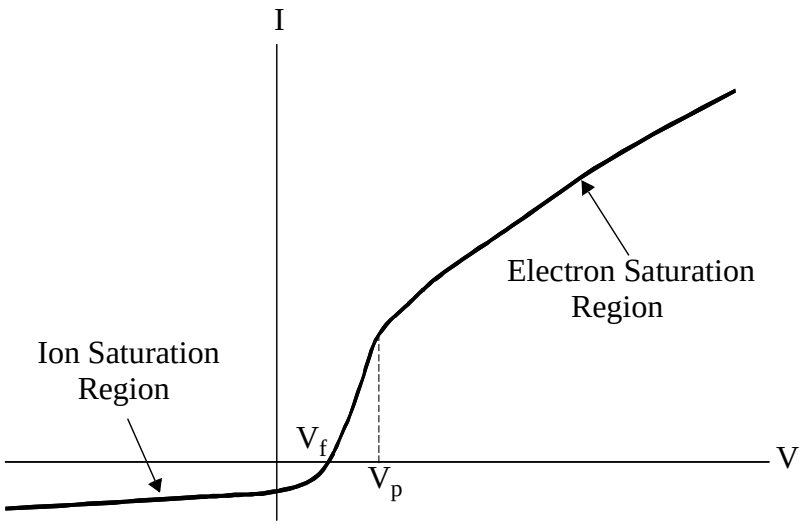

Figure 2.6 General appearance of the I-V characteristic for an emissive probe.

Another method for deducing plasma potential is through the use of a floating emissive probe. This technique consists of measuring the floating potential at various heating currents. As the heating current increases, the floating potential increases until it saturates at the plasma potential. The advantage of this method is the simplicity of the circuitry since no sweeping voltage is required. However, in practice, the floating potential does not occur exactly at the plasma potential. A fraction of the emitted electrons backstream to the probe because of a potential minimum that appears between the probe surface and the plasma. Thus, this prevents the emissive probe from floating at the plasma potential [7].

2.3 Faraday Probe

The Faraday probe is a diagnostic instrument that measures current density. It consists of a flat plate collector that is biased at potentials between −12V and −20V, which repels electrons from the plasma. The collector is generally made of stainless steel and sprayed

with tungsten to reduce secondary electron emission. In addition, a guard ring is placed around the collector, as seen in Figure 2.7, to shield it from low energy ions arriving from non axial directions, and also to reduce electrostatic edge effects.

Several Faraday probe design issues need to be considered. The design issues include probe voltage bias, material choice, spacing between collector and guard ring, and sizing of the collector. To minimize edge effects around the collector, a flat uniform sheath is created by biasing the collector and the guard ring at the same potential [19]. The spacing between the collector and the guard ring is minimized to overlap the collector and the guard ring sheaths.

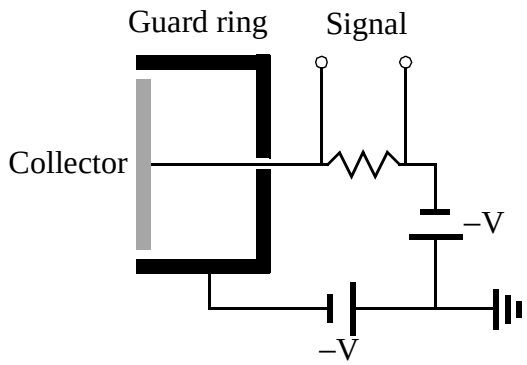

Figure 2.7 Schematic of a Faraday probe with the same voltage bias applied to both the collector and the guard ring [18].

Faraday probe data is measured in the following ways. As ions hit the face of the collector, electrons contained within the metal of the Faraday probe stream to the probe's face to neutralize the collected ions. These moving electrons make up the probe current, which is equal to the ion current. Current density is determined by measuring the ion current and dividing by the area of the collector. This current density is measured for different angular positions to obtain a current density distribution, which is integrated to find beam current. Finally, the beam current can be used to determine plume divergence.

2.4 Retarding Potential Analyzer

A retarding potential analyzer (RPA) is a diagnostic instrument that measures current density and ion energy. It is composed of a current collector that is shielded by biased grids. Positively biased grids repel low energy ions, while negatively biased grids repel electrons. The positively biased grid potential is varied from 0 to 500V and current is measured simultaneously. Four grids are typically used in RPAs, of which the first grid is floated to reduce plasma perturbation, the second grid is positively biased to repel electrons, the third grid is negatively biased to only repel selected ions, and the fourth grid is positively biased with respect to the collector to repel secondary electrons. The spacing of the grids is optimized to minimize space charging effects. Figure 2.8 portrays an RPA, as well as a schematic of the grids' bias.

Despite their ease of use, RPAs have several design issues. For example, the internal pressure of the RPA may cause the ion to collide before reaching the collector, thus leading to a decreased energy peak and a widened energy distribution towards lower ion energy.

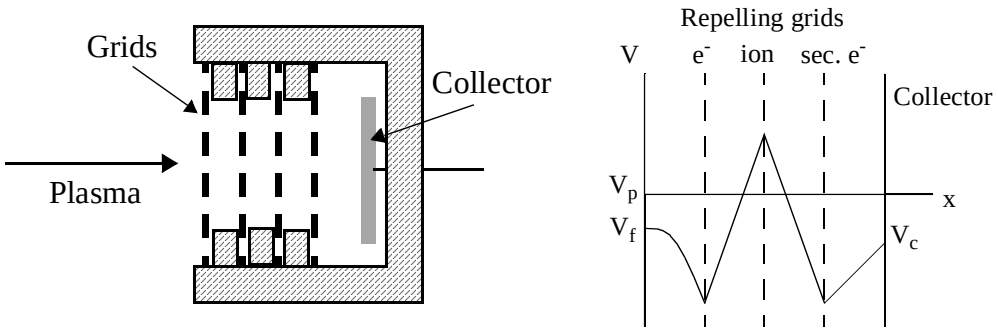

Figure 2.8 Schematic of a retarding potential analyzer [18].

2.5 Quartz Crystal Microbalance

A Quartz Crystal Microbalance (QCM) is an instrument that measures material deposition. QCMs, pictured in Figure 2.9, require little power and are light, small, and have a considerable flight heritage. To measure material deposition, two quartz crystals are used, where one is exposed to the plume and the other is shielded for reference. The amount of material deposited is indicated by the change in frequency between the two crystals. The QCM sensitivity is on the order of a monolayer of atoms and is determined experimentally by the variation of the crystals' fundamental frequency. Assuming a uniform condensate density, ρ, the rate of deposition is determined by

$$\Delta F = S_f\left(\frac{\Delta m}{A}\right) = S_f(\rho \dot{\delta} \Delta t) \tag{2.3}$$

where S_f is the crystal sensitivity, $\frac{\Delta m}{A}$ is the change in mass per unit area, Δt is time, and $\dot{\delta}$ is the rate of deposition.

Figure 2.9 Picture of a QCM [14].

Chapter 3

FARADAY PROBE EXPERIMENTAL METHODS

3.1 Faraday Probe Development

3.1.1 Probe Requirement

To ensure an adequate Faraday probe design, several necessary requirements were met. A Faraday probe can cause plasma perturbations due to the large amount of metal present in the probe, as opposed to a Langmuir probe. Miniaturization of the probe was required to minimize these perturbations. Furthermore, a miniature probe would improve measurement resolution. In addition, the spacing between the collector and the guard ring was optimized to allow overlap between the sheaths, which is necessary to produce a smooth surface over the collector.

Another requirement involved electron rejection by the collector, which was achieved by applying a negative voltage bias to the probe. This bias should be small enough so that it would not substantially turn the ion trajectories and increase ion collection. The probe voltage bias was chosen so that the ion flux was still nearly constant as the probe bias was increased. This choice ensured that the probe was operating in the ion saturation regime. Finally, to minimize edge effects around the collector, a flat uniform sheath over the collection area was created by biasing both the guard ring and collector to the same negative potential.

3.1.2 Probe Design

To satisfy the requirements regarding Faraday probe miniaturization, both the guard ring and collector dimensions were minimized. The guard ring consists of a hollow metal cylinder spotwelded to a washer, where the hollow cylinder dictates the dimensions of the guard ring. On other hand, the collector consists of a thin metallic disc. The miniaturization requirement of the guard ring and collector is coupled to the spacing requirement discussed in Section 3.1.1.

The spacing between the guard ring and the collector was determined by calculating the plume Debye length. The minimum spacing was approximated as 5 to 10 Debye lengths. The plume Debye length, λ_D, is determined by

$$\lambda_D = \sqrt{\frac{\varepsilon_0 k T_e}{n_e e^2}} = 69.025\sqrt{\frac{T_e}{n_e}} \tag{3.1}$$

where T_e is in Kelvin and n_e is in m^{-3}. Using equation (3.1), the Debye length varies from 0.1 mm to 1 mm at a radius of 25 cm, the radius of interest in this research. Therefore, the probe sheath thickness, which is also the spacing between the collector and the guard ring, varies from 0.5-1 mm to 5-10 mm. Thus, the minimum spacing between the collector and the guard ring should be smaller than 0.5 mm.

The main component of the guard ring, the hollow cylinder, has an outside diameter of 6.35 mm, a length of 2.54 mm, and a wall thickness of 0.51 mm. These dimensions represented the smallest cylinder available from Kimball Physics Inc., a provider of high temperature materials and high purity insulators.

The minimum collector diameter was calculated by using the spacing between the collector and guard ring and the dimensions of the hollow cylinder, using

$$D_c = D_r - 2t_r - 2t_s \tag{3.2}$$

where D_r is the outside diameter of the hollow cylinder, t_r is the wall thickness of the cylinder, and t_s is the spacing between the collector and the cylinder. From these parameters, a collector diameter of 4.45 mm was calculated, and in turn the spacing, t_s, was determined to be 0.45 mm, which lies in the required range for sheath thickness.

The material of choice for both the guard ring and collector was 304 stainless steel due to its high melting point of 1700K, its ease in machining, and its relatively low cost compared to other metals used in Faraday probes, such as tungsten. Secondary electron emission was not a serious issue at the ion energies used here (< 400eV).

Thus, the final Faraday probe design consisted of a 4.45 mm diameter stainless steel collector and a 6.35 mm diameter stainless steel guard ring. Figure 3.1 shows a 3-view drawing of the nude Faraday probe. The appropriate probe voltage bias that satisfied the above requirements is discussed in Section 3.3.4.

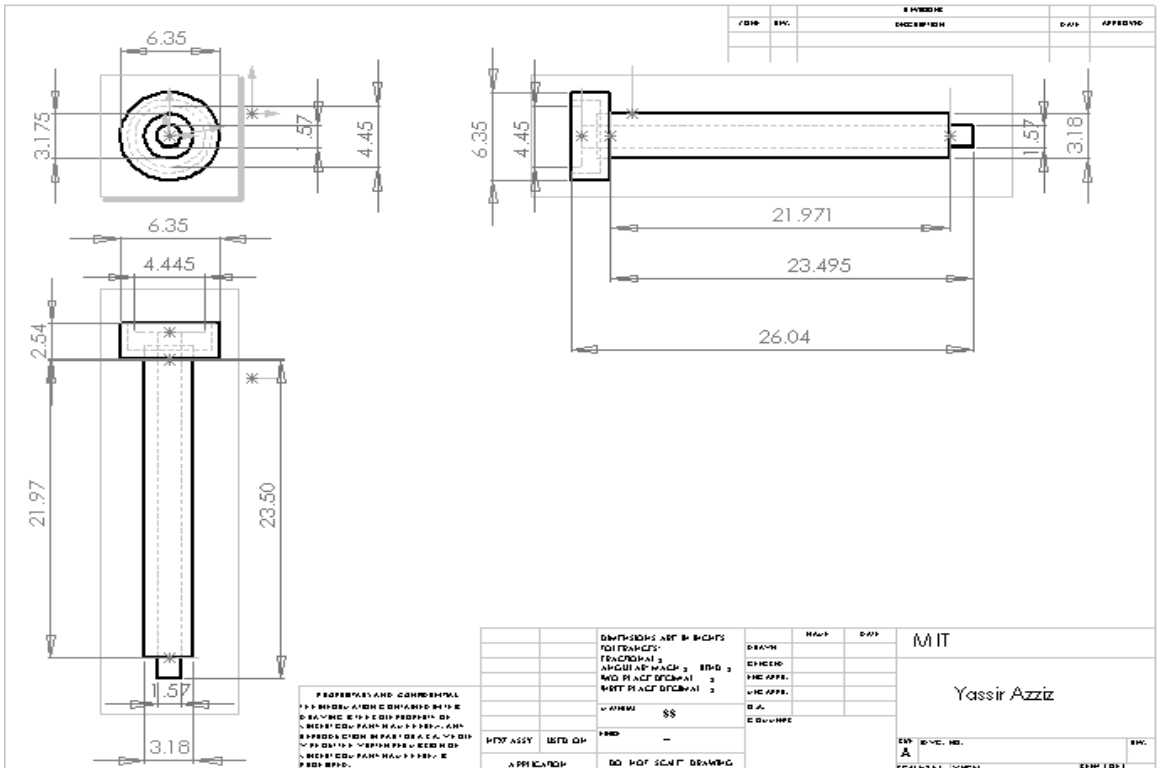

Figure 3.1 3-view drawing of the Faraday probe.

3.1.3 Probe Construction

Probe construction requires several consecutive steps for ease of manufacturing. The first step involves guard ring construction. The guard ring consists of a hollow cylinder with a 6.35 mm outside diameter, a 2.54 mm length, and a 0.051 mm wall thickness, a wire ring with a 6.35 mm outside diameter and a 0.79 mm thickness, and a washer with a 6.35 mm outside diameter and a 3.23 mm inside diameter. To construct the guard ring, the washer was first spotwelded to the wire ring in four locations 90° apart. The washer was then attached to the cylinder by spotwelding the wire ring to the cylinder in four locations 45° from the first spotwelded points. The end result was a guard ring that resembled a cup with a 3.23 mm hole diameter at its base.

The guard ring was inserted 1.3 mm into a single-bore ceramic tube. The ceramic tube consists of 99.8% alumina and has a 3.18 mm outside diameter and is 102 mm in length. The guard ring was fixed on the alumina tube using a lock ring, a stainless steel low-compliance spring. The back face of the guard ring, the washer, was then spotwelded to the lock ring at four locations 90° apart. Also, to provide voltage bias to the guard ring, a stainless steel wire was wound around and spotwelded to the guard ring.

The collector was spotwelded to a 3.18 mm diameter stainless steel rod, which enabled current to flow from the collector to the power supply. The stainless steel rod was also used to provide voltage bias to the collector. To spotweld the collector to the rod, a stainless steel wire was wound at the tip of the rod and then spotwelded at four locations 90° apart. The collector was then spotwelded to the stainless steel wire at four locations, 45° from the first spotwelded points.

To provide insulation to the stainless steel rod, it was inserted into the alumina-guard ring combination. The stainless steel rod was slightly bent during insertion to cause friction between the stainless steel rod and the inner wall of the alumina tube. This friction prevented the stainless steel rod from slipping inside the alumina tube once it was in place. The stainless steel rod was positioned inside the alumina tube to ensure the collector was

flush with the exit surface of the guard ring. Specifically, there was a 1.3 mm clearance between the collector and the tip of the alumina tube. This gap was necessary to prevent the sputtering of alumina on the collector, which can affect current density measurements. Figure 3.2 displays the final Faraday probe design.

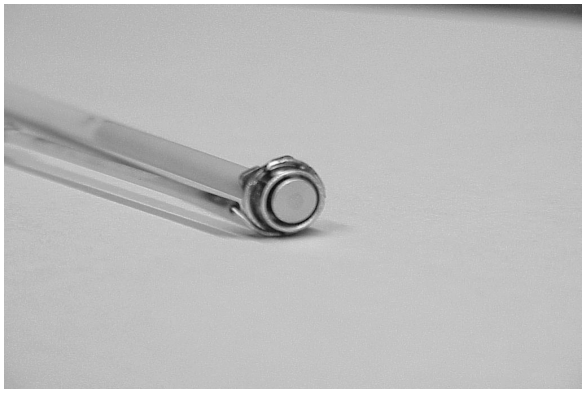

Figure 3.2 Final Faraday probe design.

3.2 Faraday Probe Design Verification

To ensure the MIT Faraday probe yields accurate data, it was cross-calibrated at the University of Michigan Plasmadynamics and Electric Propulsion Laboratory (PEPL) against a larger Jet Propulsion Laboratory (JPL) probe. This experiment consisted of taking both probes' current density measurements concurrently. Setup and data collection was conducted by University of Michigan Ph.D. student M. Walker. The measure of success for the MIT Faraday probe is based on the degree of similarity between current density measurements from the MIT and JPL probes. A good agreement between the measurements obtained from the two probes would indicate that the MIT probe is reliable for mapping Hall thruster plumes. This is due to the fact that the JPL probe is extensively tested and proven to yield accurate results [19].

3.2.1 Experimental Setup[1]

The experiment was conducted in the University of Michigan's Large Vacuum Test Facility (LVFT), shown in Figure 3.3. The LVFT is a stainless steel vacuum chamber, with a diameter of 6 m and a length of 9 m. The facility is equipped with seven CVI TM-1200 re-entrant cryopumps, each of which is surrounded by a LN_2 baffle. With seven pumps operating, the pumping speed of the facility is 240,000 L/s on Xenon with a base pressure of 2.5×10^{-7} Torr. The chamber pressure is monitored by two hot-cathode ionization gauges. The first gauge is a Varian model 571 gauge with HPS model 919 Hot Cathode Controller. The second is a Varian model UHV-24 nude gauge with a Varian UHV senTorr Vacuum Gauge Controller. Pressure measurements from both gauges were corrected for xenon using

$$P_c = \frac{P_i - P_b}{2.87} + P_b \tag{3.3}$$

where P_c is the corrected pressure, P_b is the base pressure, and P_i is the indicated pressure during the flow of xenon into the vacuum chamber. In this experiment, the LVFT was operated with four and seven cryopumps corresponding to pumping speeds of 140,000 L/s and 240,000 L/s respectively.

1. Details of the Michigan experimental setup were obtained primarily from Reference [19].

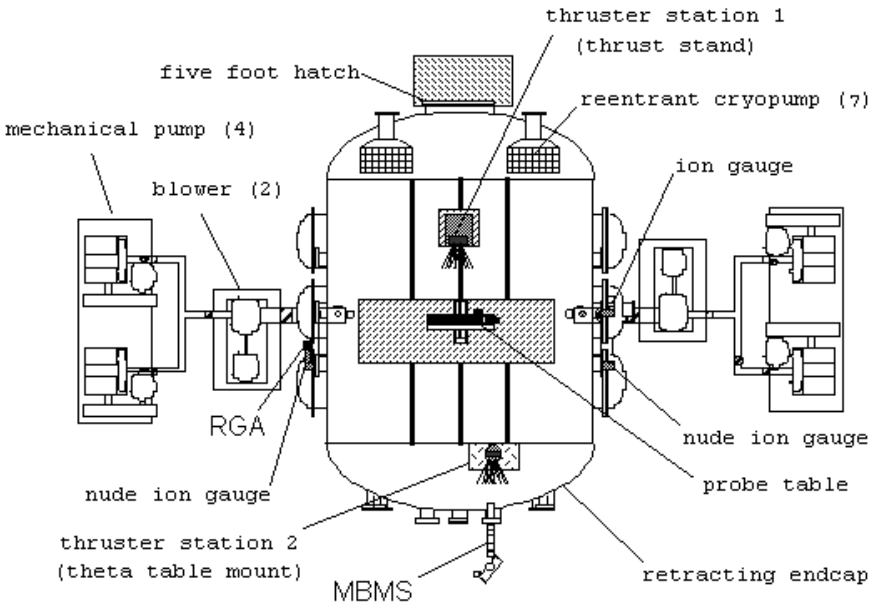

Figure 3.3 Schematic of the LVFT.

Current density measurements of the two probes were conducted on the P5-2 Hall thruster. The thruster was mounted in the LVTF at thruster station 1 as shown in Figure 3.3. The P5-2, shown in Figure 3.4, has a mean diameter of 148 mm and a channel width of 25 mm, with a nominal power of 5 kW. In this experiment, the thruster was run in a single stage mode at 1.5 kW. Further details and performance measurements about the P5-2 can be found in Reference [19].

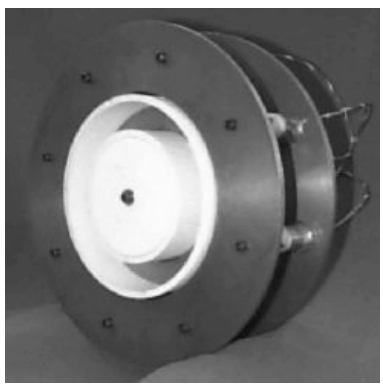

Figure 3.4 The Michigan P5-2 Hall thruster.

The JPL Faraday probe consists of a 23.11 mm diameter collection electrode enclosed within a 25.4 mm diameter guard ring. Figure 3.5 shows a cross-section and a picture of the probe. The collector is made of aluminum and spray-coated with tungsten to minimize secondary electron emission. Table 3.1 summarizes the JPL Faraday probe dimensions. This probe has an extensive testing heritage both at JPL and at the University of Michigan. It has been proven to yield accurate current density measurements. The results of the JPL Faraday probe measurements with a more detailed description of this probe can be found in Reference [19].

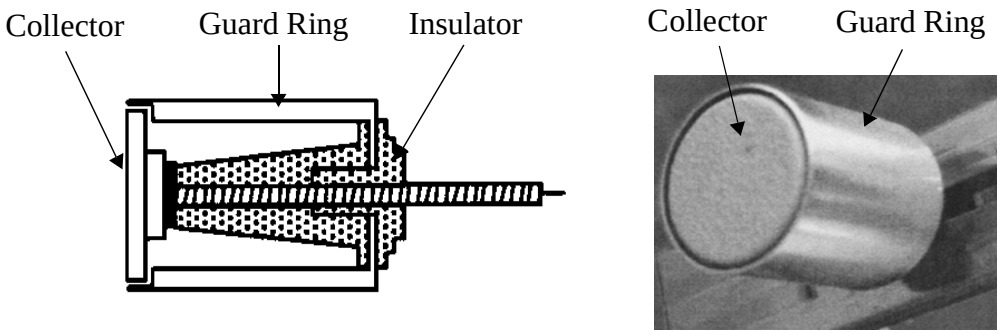

Figure 3.5 Cross-section and picture of the JPL Faraday Probe [19].

TABLE 3.1 Dimensions of the JPL Faraday probe [19].

Part Name	Dimensions (mm)
Collector	
Outer Diameter	23.1
Gap Thickness	2.3
Guard Ring	
Outer Diameter	25.4
Thickness	0.74

The MIT and JPL probes were mounted 18° apart on an overhead rotating arm in the LVTF. The probes' collectors were facing the exit plane of the thruster, as shown in Figure 3.6. The arm is attached to a Parker Daedal 20600RT rotary table, which is driven by an Empire Magnetics VSU23 stepper motor. A National Instruments NuDrive 4SX-411 powers the stepper motor, and control of the table is provided by a National Instruments PCI-7344 stepper controller through a LabView 6 interface. The probes were placed 1 m downstream of the exit plane of the P5-2. They were swept ±100° from the thruster centerline through the plume in 1° increments. Looking downstream from the thruster exit plane, angles become increasingly positive when the arm is moved clockwise from centerline. Both probes were biased at –20V. Current drawn by the Faraday probes was determined by measuring the voltage across a current shunt, as shown in Figure 3.7.

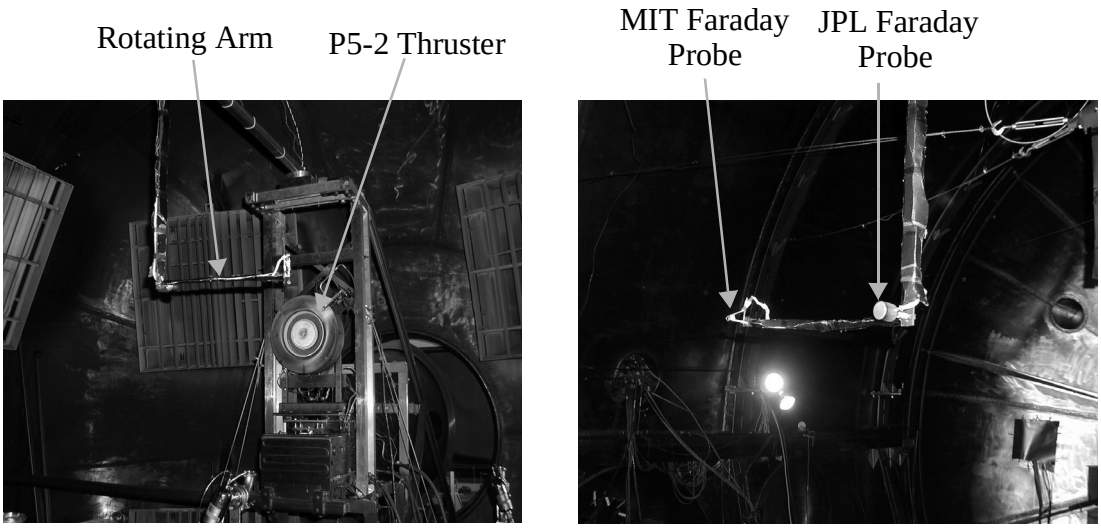

Figure 3.6 Setup of the MIT and JPL Faraday probes on an arm facing the P5-2 Hall thruster.

Probe data were acquired using a 22-bit Agilent Data Logger head unit (HP34970A) with a 20-channel multiplexer (HP34901A) through the same LabView interface used to control the rotary table. The data logger was used to measure and store the voltage drop across the two current shunts. The ion current density is then computed by using

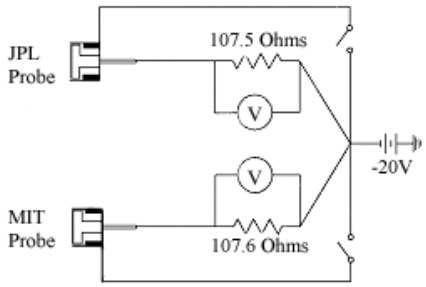

Figure 3.7 Electrical schematic of the JPL and MIT Faraday probes [19].

$$j = \frac{V}{RA_p} \tag{3.4}$$

where V is the measured voltage, R is the shunt resistance, and A_p is the probe collector area. A scan of the thruster plume from $-100°$ to $100°$ took approximately 6 minutes. The results of the scans are presented in the following section.

3.2.2 Results

Figures 3.8 and 3.9 represent current density distributions for the MIT and JPL Faraday probes at background pressures of 7.6×10^{-6} Torr and 4.6×10^{-6} Torr respectively. The current density distributions for both probes in both cases are identical, indicating good agreement. As discussed earlier, the JPL probe has an extensive testing heritage and is proven to yield accurate current density measurements. Thus, it can be concluded that the MIT Faraday probe also produces accurate measurements of current density. Therefore, it is a reliable Faraday probe that can be used to map the plume of the BHT-200 Hall thruster with confidence.

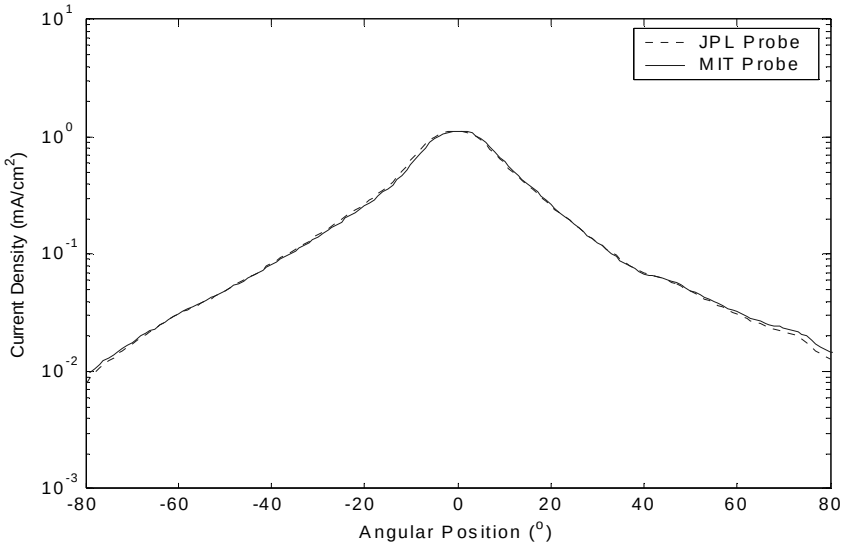

Figure 3.8 Current density distribution for the JPL and MIT Faraday probes. V_D = 300V, I_D = 5.42A, and P = 7.6x10^{-6} Torr.

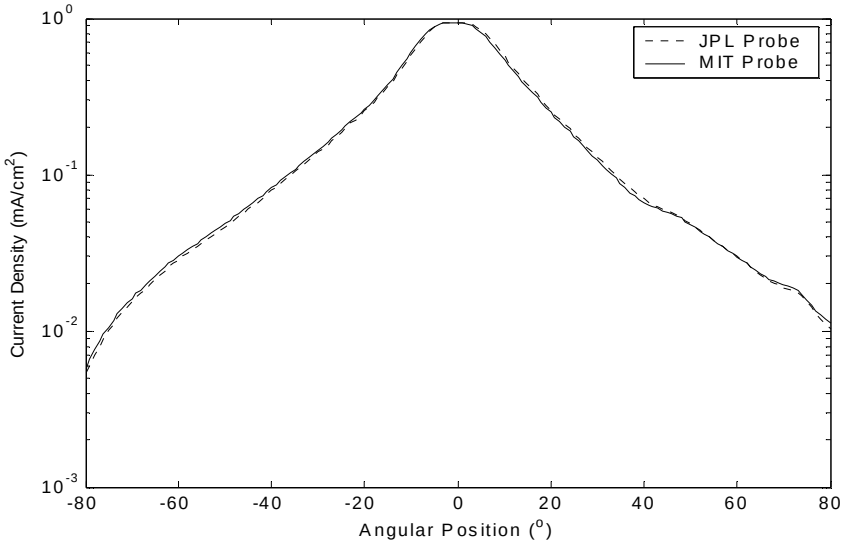

Figure 3.9 Current density distribution for the JPL and MIT Faraday probes. V_D = 300V, I_D = 5.12A, and P = 4.6x10^{-6} Torr.

3.3 Faraday Probe Experimental Setup

Once the designed Faraday probe was proven to be reliable, it was used to map the BHT-200 Hall thruster plume. This section describes the experimental procedure for using the Faraday probe in testing the plume. The results of the Faraday probe measurements will be discussed in detail in Chapter 4.

3.3.1 The Busek Vacuum Facility

Current density measurements were conducted in the Busek vacuum facility. The nature of the tests that were conducted included studying the effects of background pressure on current density. The Busek facility provides vacuum chambers where background pressure could be varied. The experiments were performed in the T6 tank. The T6 tank, shown in Figure 3.10, consists of two liquid nitrogen LN_2 cooled sections, an experimental apparatus section, and a pumping section. The experimental apparatus section is 1.8 m in diameter and 1.8 m in length, and the pumping section is 2.4 m in diameter and 1.2 m in length. The T6 tank is equipped with a 0.8 m diameter oil diffusion pump used to remove low molecular weight gases. The diffusion pump is capable of a pumping speed of 8,000 L/s of xenon. The T6 tank is also equipped with four cryo-panels. With the diffusion pump and the cryo-panels operating, the vacuum tank is capable of a pumping speed of 90,000 L/s of Xenon. In addition, an LN_2 baffle, located above the diffusion pump, is used to prevent any hot oil vapor from reaching the experimental section of the tank. The chamber pressure is monitored by a hot-cathode ionization gauge. Pressure measurements from the gauge were corrected for xenon using equation (3.3).

Figure 3.10 Busek T6 vacuum chamber.

3.3.2 Hall Thruster Setup

The BHT-200, shown in Figure 3.11, was mounted in the T6 tank in the experimental section. It was installed on the top of a two-shelved bridge, so that the centerline of the thruster coincided with the center of the vacuum chamber. The thruster was positioned so that the plume was allowed to freely expand approximately 2 m along the centerline axis.

The thruster was operated for an hour before any data collection to allow the discharge chamber walls to outgas and reach a thermal steady-state. The Faraday probe measurements were taken at different thruster operating conditions. Table 3.2 summarizes the thruster operating conditions at which data were acquired.

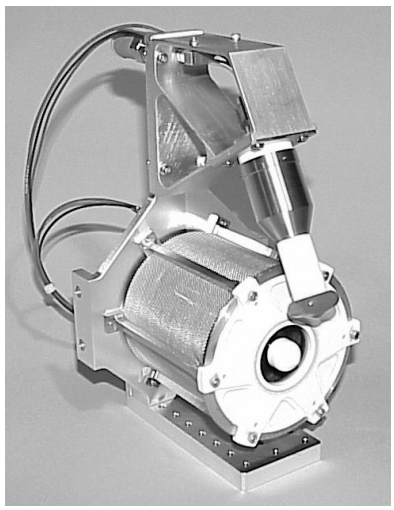

Figure 3.11 Busek BHT-200 Hall thruster.

TABLE 3.2 BHT-200 operating conditions for Faraday probe measurements.

V_D (V)	I_D (A)	Anode Flow (mg/s)	Cathode Flow (mg/s)	Pressure (Torr)
225	0.888	0.85	0.1	8.0×10^{-5}
225	0.824	0.85	0.1	2.2×10^{-5}
225	0.792	0.85	0.1	4.0×10^{-6}
250	0.878	0.85	0.1	8.0×10^{-5}
250	0.797	0.85	0.1	2.2×10^{-5}
250	0.795	0.85	0.1	4.0×10^{-6}
300	0.878	0.85	0.1	8.0×10^{-5}
300	0.817	0.85	0.1	2.2×10^{-5}
300	0.800	0.85	0.1	4.0×10^{-6}

3.3.3 Faraday Probe Setup

The probe was mounted on a rotating arm facing the exit plane of the thruster inside the Busek vacuum chamber, as shown in Figure 3.12. The arm was attached and driven by a Motion Group stepper motor model 5609M with a resolution of $0.9°$. The stepper motor was attached to the bottom shelf of the bridge. A SID 2.0^{TM} controller powered the stepper motor, which was connected to a computer through a serial link. The SID controller was commaded by a BASIC program to move the stepper motor and place the arm in the desired position. The probe was placed 25 cm downstream of the exit plane of the BHT-200. It was swept $\pm 90°$ from the thruster centerline through the plume in $2°$ increments. -12V was applied to both the collector and guard ring throughout the entire experiment. The selection of this probe voltage bias is discussed in more detail in the next section. Probe data were acquired using a 22-bit Agilent Data Logger head unit. The data logger was used to measure and store the voltage drop across the current shunt, as shown in Figure 3.13. The ion current density was then computed by using equation (3.4). A scan of the thruster plume from $-90°$ to $90°$ took approximately 30 minutes.

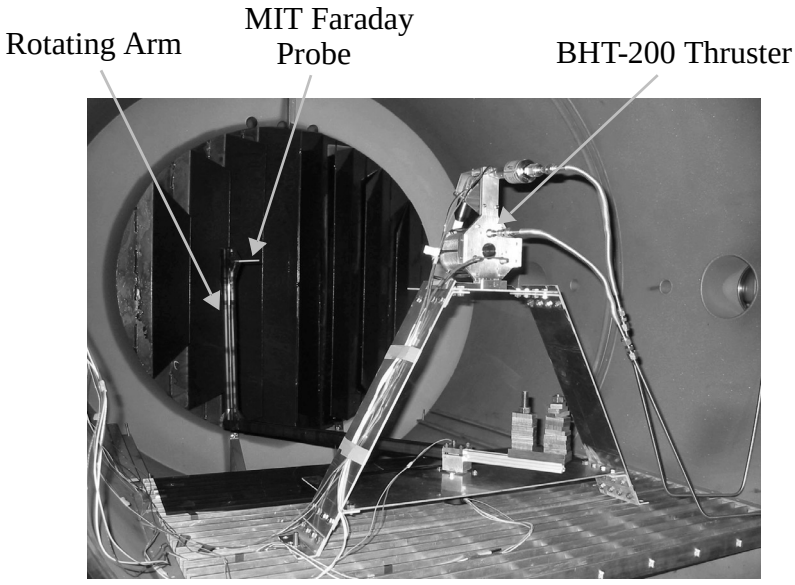

Figure 3.12 Setup inside the vacuum chamber of the MIT Faraday probe on a rotating arm facing the BHT-200 Hall thruster.

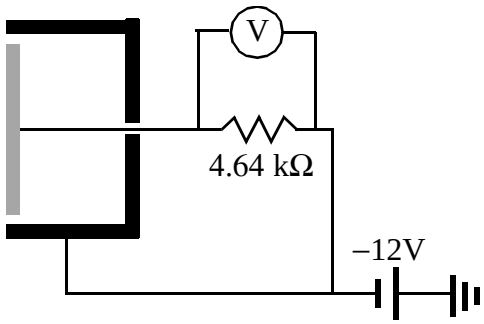

Figure 3.13 Electrical schematic of the MIT Faraday probe.

3.3.4 Probe Voltage Bias Study

Several voltage biases were applied to the probe to determine the appropriate value. The probe's voltage bias was swept from 0V to –30V in 1V increments. At each increment, the current density was measured. The arm was positioned at 0°, 45°, and 90° with respect to the centerline. The thruster was operated at its nominal conditions of 250V discharge voltage, 0.85 mg/s flowrate to the anode, and 1A magnet current. The probe was positioned 25 cm away from the exit plane of the thruster. Figures 3.14 through 3.16 show the effect of varying the probe bias at different angular positions.

Figures 3.14 through 3.16 illustrate that the onset of current density saturation occurs at –8V for all angular positions. The probe collection is in the ion saturation regime starting at a voltage bias of –8V. The ion saturation regime is the region of interest since the current density is insensitive to the increase of the probe bias. Therefore, –12V was arbitrarily chosen as the probe bias, which is not high enough to disturb the plasma. This probe bias was used throughout the Faraday probe experiments for both the collector and guard ring, as shown in Figure 3.13.

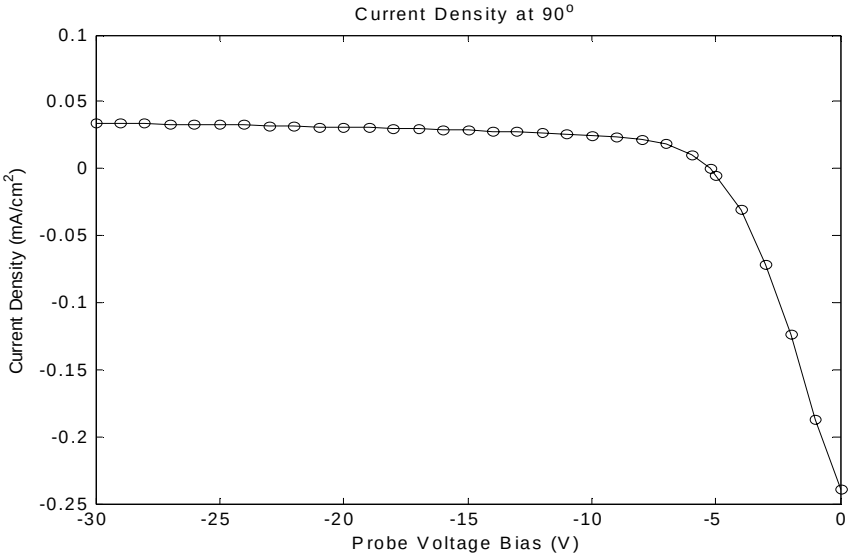

Figure 3.14 Current density for various probe voltage biases at the 90° position; onset of current density occurs at −8V.

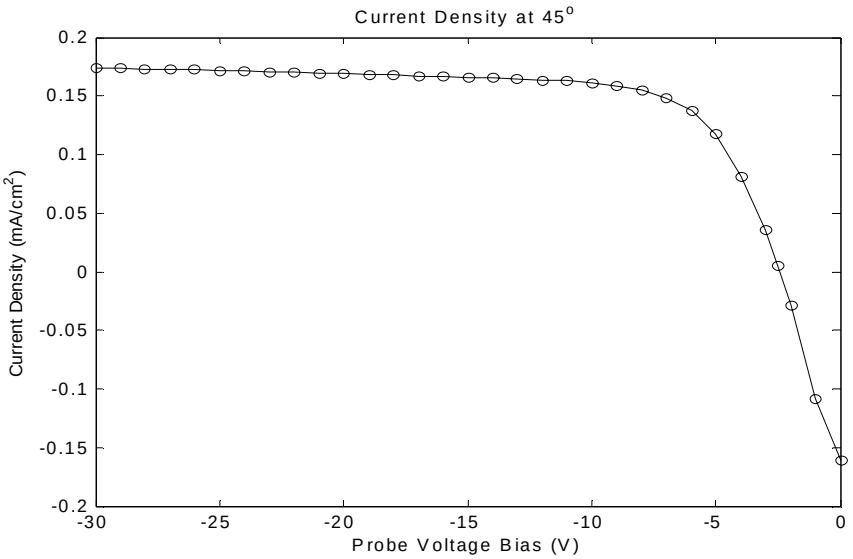

Figure 3.15 Current density for various probe voltage biases at the 45° position; onset of current density occurs at −7V.

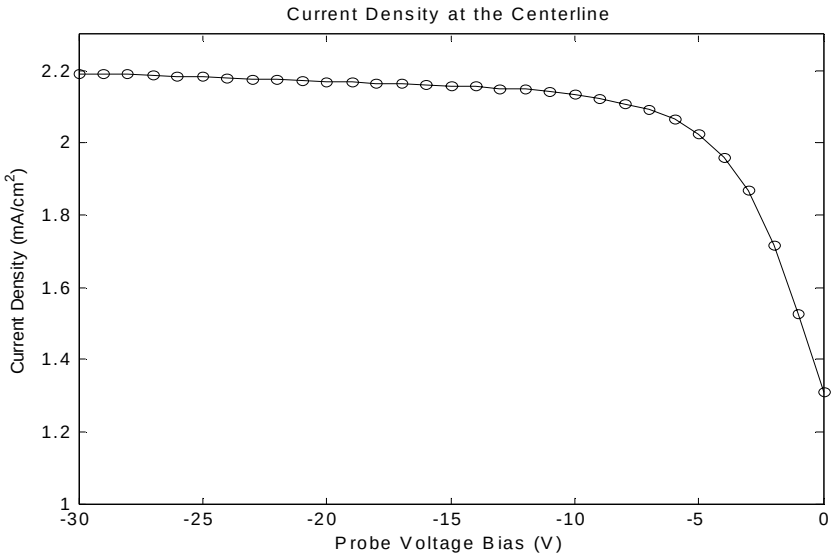

Figure 3.16 Current density for various probe voltage biases at the centerline; onset of current density occurs at –6V.

Chapter 4

FARADAY PROBE RESULTS

4.1 Overview

This chapter presents Faraday probe results at the thruster operating conditions described in Chapter 3. The effects of background pressure, discharge voltage, flow rate, and sweep radius on the current density distribution were investigated. The chapter also presents analyses performed to verify hypotheses, which were used to explain phenomena observed in the experimental results. These results serve as a database to verify plume computational models.

4.2 Current Density Distribution

Figures 4.1 and 4.2 portray a typical current density distribution for the BHT-200 thruster plume. It was conducted at the following conditions: discharge voltage of 250V, discharge current of 0.8A, flow rate of 0.85 mg/s, pressure of 2.2×10^{-5} Torr, and sweep radius of 25cm. The distribution is symmetric with respect to the centerline with "shoulders" at the wings and a double hump at the peak. The maximum current density occurs at the centerline, whereas the minimum current density occurs at the wings, with a maximum to minimum ratio of 180. Figures 4.1 and 4.2 display the current density distribution using a logarithmic and normal scale respectively. The logarithmic scale provides more information regarding the wings of the curve. In particular, shoulders are observed at the wings on

the log scale curve, which are not displayed in the normal scale curve due to the high maximum to minimum current density ratio.

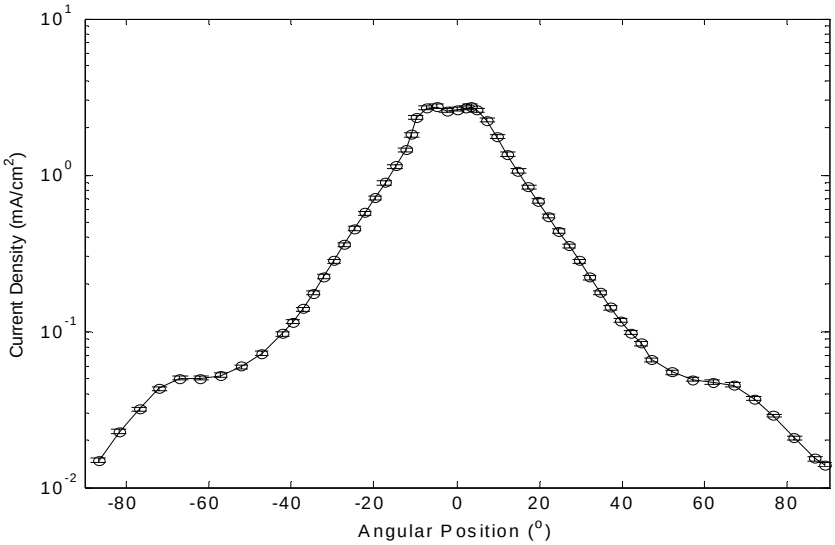

Figure 4.1 Typical current density distribution for the BHT-200 Hall thruster plume in a logarithmic scale. V_D = 250V, I_D = 0.8A, P = 2.2x10^{-5} Torr, $\dot{m}$ = 0.85 mg/s, and sweep radius = 25cm.

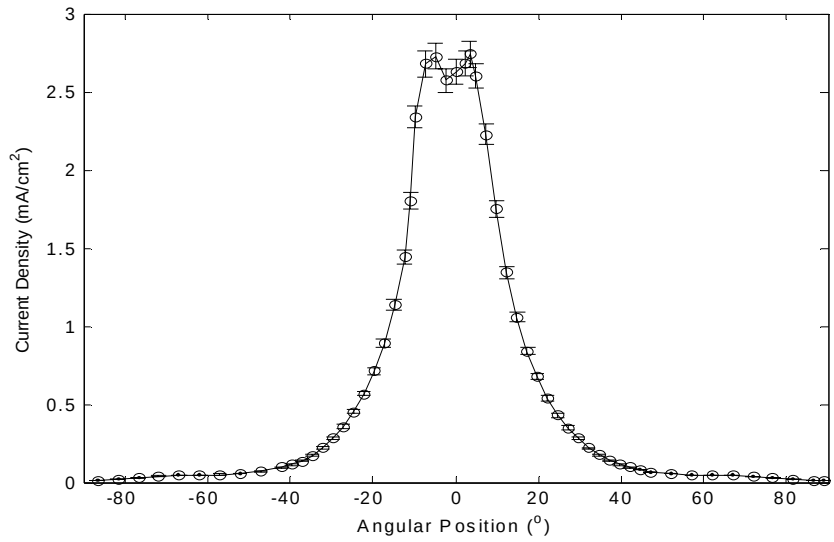

Figure 4.2 Typical current density distribution for the BHT-200 Hall thruster plume in a normal scale. V_D = 250V, I_D = 0.8A, P = 2.2x10^{-5} Torr, $\dot{m}$ = 0.85 mg/s, and sweep radius = 25cm.

Each data point shown in Figures 4.1 and 4.2 is an average of three measurements. The data taken with the probe rotated clockwise and counterclockwise was averaged. The standard deviation about the average value for these measurements was less than 5%, indicating good reproducibility.

The double hump at the peak of the current density distribution occurs because of the annular discharge channel. The magnetic field of the Hall thruster is designed to focus the annular discharge to a single beam by the canting of the magnetic field. This focusing leads to the angling of the plasma exhaust at the exit plane towards the centerline. In turn, this angling causes plume crossing at the centerline, which produces a "swallow tail" plume configuration. The "swallow tail" consists of a V-shaped plume jet at the centerline, causing the double hump of the current density distribution at the peak.

The shoulders, which are present at the wings in the current density distribution, are probably explained by charge exchange collisions. An exchange of charge occurs when a fast moving ion collides with a slow moving neutral, causing the fast moving ion to become a fast moving neutral and the slow moving neutral to become a slow moving ion. The potential in the plume is greatest at the centerline and lowest at the wings. Therefore, the slow moving ions, do not have enough energy to overcome the plume potential, and are pushed to the side, creating an accumulation of charge exchange ions in the wings.

4.2.1 Effect of Background Pressure

To study facility effects on current density, the background pressure was varied at 8.0×10^{-5} Torr, 2.2×10^{-5} Torr, and 4.0×10^{-6} Torr, and current density measurements were taken at each background pressure. Figures 4.3 through 4.5 depict the effect of background pressure on current density at discharge voltages of 225V, 250V, and 300V respectively. The flow rate to the anode for all cases was 0.85 mg/s. A logarithmic scale was used to plot the figures.

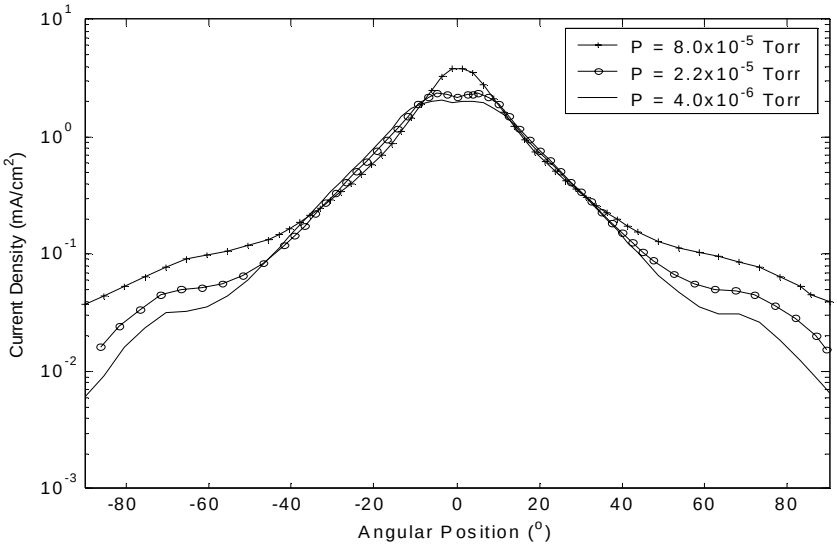

Figure 4.3 Effect of background pressure on the current density distribution. V_D = 225V, $\dot{m}$ = 0.85 mg/s, and sweep radius = 25cm.

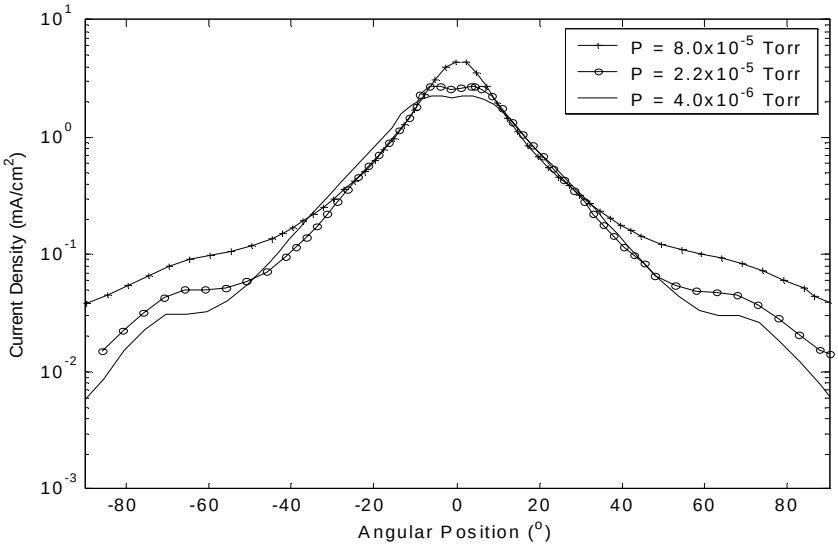

Figure 4.4 Effect of background pressure on the current density distribution. V_D = 250V, $\dot{m}$ = 0.85 mg/s, and sweep radius = 25cm.

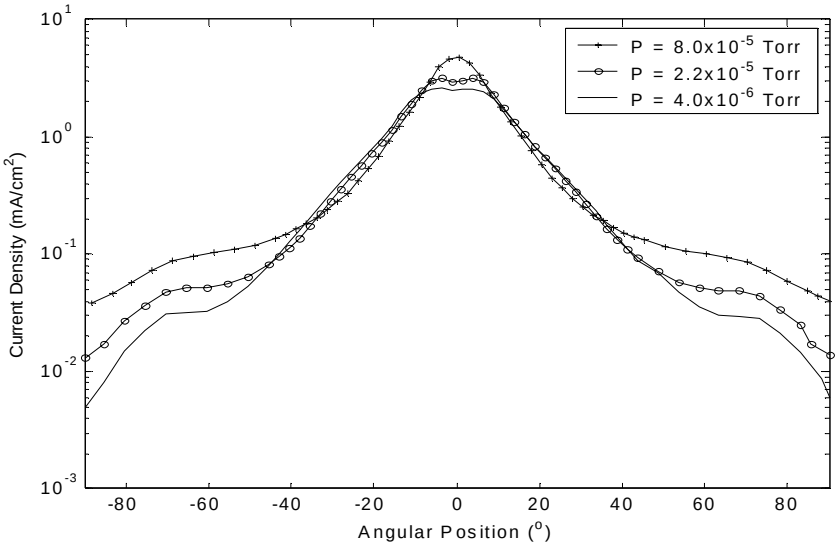

Figure 4.5 Effect of background pressure on the current density distribution. V_D = 300V, $\dot{m}$ = 0.85 mg/s, and sweep radius = 25cm.

The current density distributions in Figures 4.3 through 4.5 are symmetric about the centerline. A relationship between increased background pressure and increased current density at the centerline is seen from the profile. An increase in background pressure leads to an increase in the number of background neutrals in the vacuum tank. These background neutrals, which are unaffected by the electric and magnetic fields of the thruster, travel freely into the ionization region and are ionized. These ionized background neutrals act similarly to ions from the thruster, through the acceleration channel traveling straight down the potential gradient, leading to a higher current density at the centerline. This phenomenon also leads to increased thrust, as explained in the following section.

As seen in the figures, a relationship also exists between increased background pressure and increased current density at the wings. This effect is due to an increase in charge exchange collisions. The increase in background pressure leads to a greater probability of collisions between neutrals and ions, leading to a higher number of charge exchange ions. These charge exchange ions are pushed to the wings as explained earlier, and cause the rise of the wings in the current density distribution at higher pressures.

4.2.2 Effect of Discharge Voltage

To understand the effects of the thruster on the plume, measurements of current density were taken at different discharge voltages. Figures 4.6 through 4.8 portray the effect of discharge voltage on the current density distribution at background pressures of 8.0×10^{-5} Torr, 2.2×10^{-5} Torr, and 4.0×10^{-6} Torr respectively. The flow rate to the anode for all cases was 0.85 mg/s. The figures shown are plotted using a normal scale.

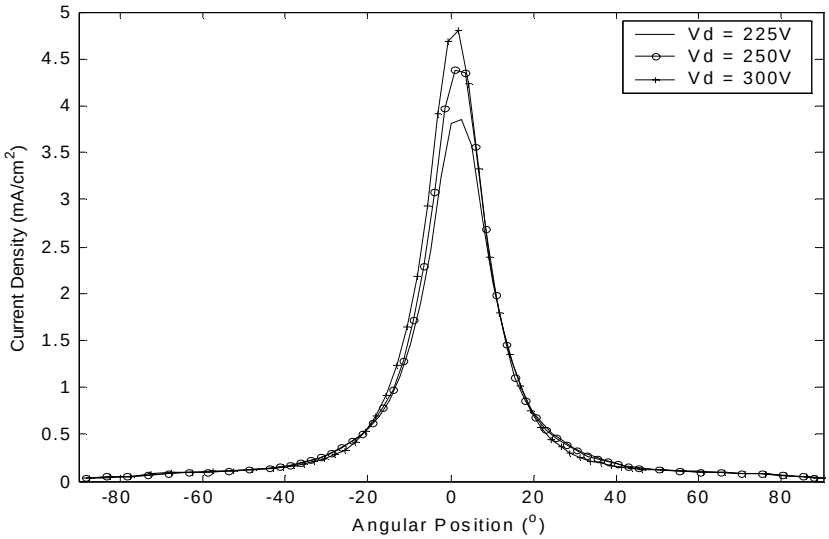

Figure 4.6 Effect of discharge voltage on the current density distribution. P = 8.0x10^{-5} Torr, $\dot{m}$ = 0.85 mg/s, and sweep radius = 25cm.

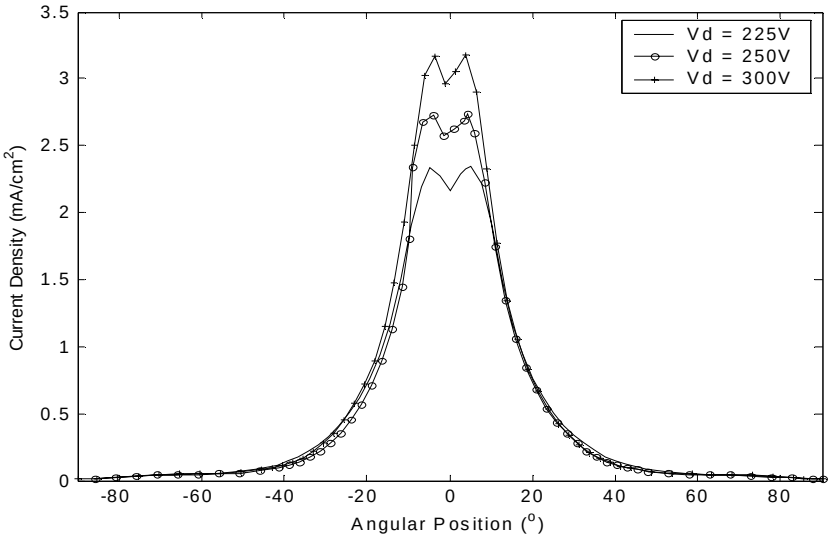

Figure 4.7 Effect of discharge voltage on the current density distribution. P = 2.2x10^{-5} Torr, $\dot{m}$ = 0.85 mg/s, and sweep radius = 25cm.

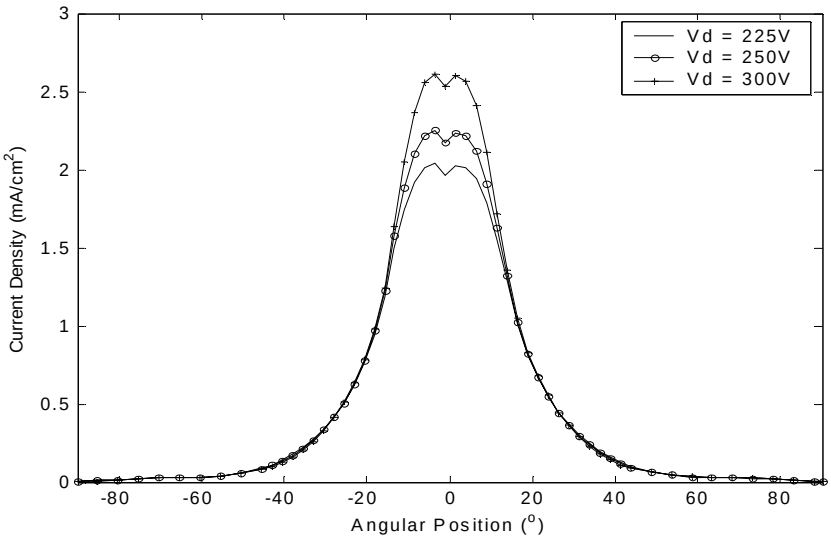

Figure 4.8 Effect of discharge voltage on the current density distribution. P = 4.0x10^{-6} Torr, $\dot{m}$ = 0.85 mg/s, and sweep radius = 25cm.

An increase in discharge voltage causes an increase in current density at the centerline. At higher discharge voltages, electrons emitted by the cathode acquire more energy, thereby increasing the utilization efficiency, the ionization rate of the xenon propellant leading to a higher current density at the centerline. In addition to higher ionization rate of the xenon propellant, the current density at the centerline also increases due to ionization from the presence of background neutrals. Therefore, an increase in discharge voltage leads to an increase in the number of ions at the centerline, which corresponds to an increase in thrust. This effect is more apparent at higher background pressures when comparing Figures 4.6 through 4.8. However, this increase in thrust is artificial since ionization of background neutrals is significantly decreased in the space environment. Therefore, measurements of thrust in vacuum tanks should be performed at the lowest possible pressures depending on the particular Hall thruster.

The discharge voltage does not affect the wings of the current density distributions. The wings are mainly affected by the accumulation of charge exchange ions, whose density is dependent on the density of background neutrals. However, an increase in discharge voltage does not increase the density of background neutrals, thus the wings are unchanged.

4.2.3 Effect of Flow Rate

To further characterize thruster effects on the plume, measurements of current density were taken at flow rates of 0.69 mg/s and 0.85 mg/s. Figures 4.9 through 4.11 display the effects of flow rate on current density distribution at background pressures of 8.0×10^{-5} Torr, 2.2×10^{-5} Torr, and 4.0×10^{-6} Torr respectively. The discharge voltage for all cases was 300V.

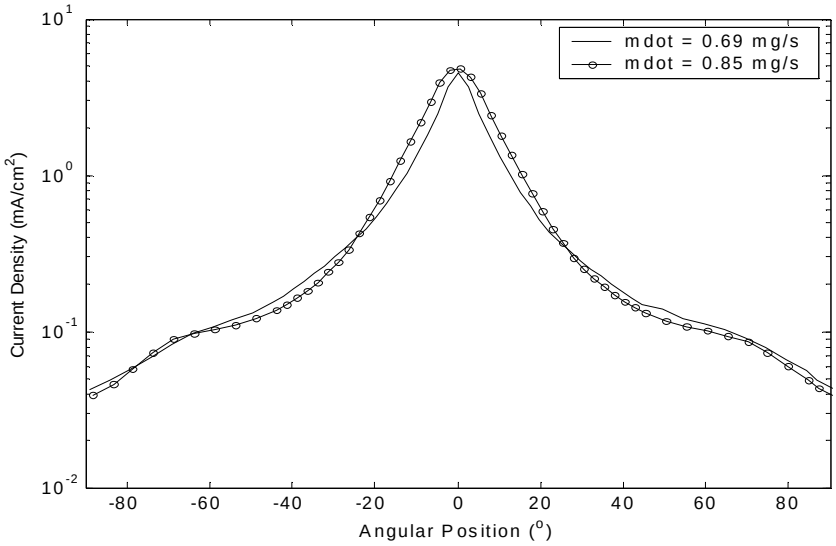

Figure 4.9 Effect of flow rate on the current density distribution. V_D = 300V, P = 8.0x10^{-5} Torr, and sweep radius = 25cm.

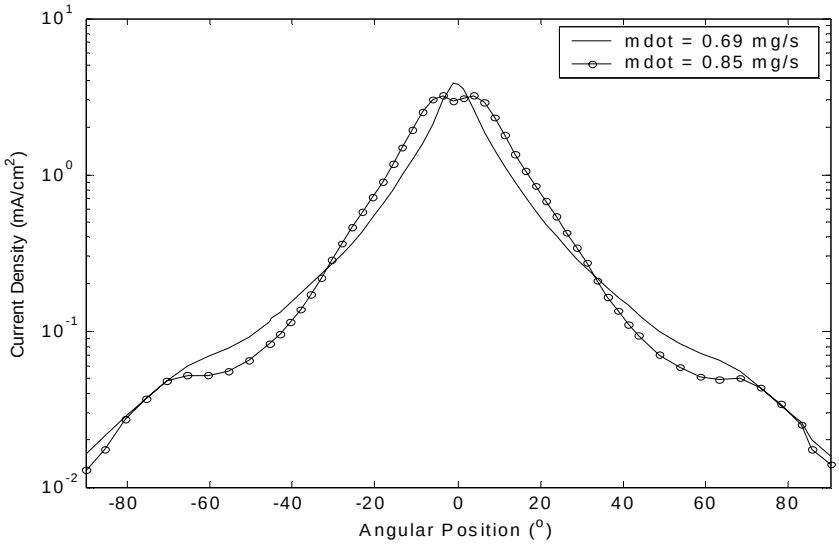

Figure 4.10 Effect of flow rate on the current density distribution. V_D = 300V, P = 2.2x10^{-5} Torr, and sweep radius = 25cm.

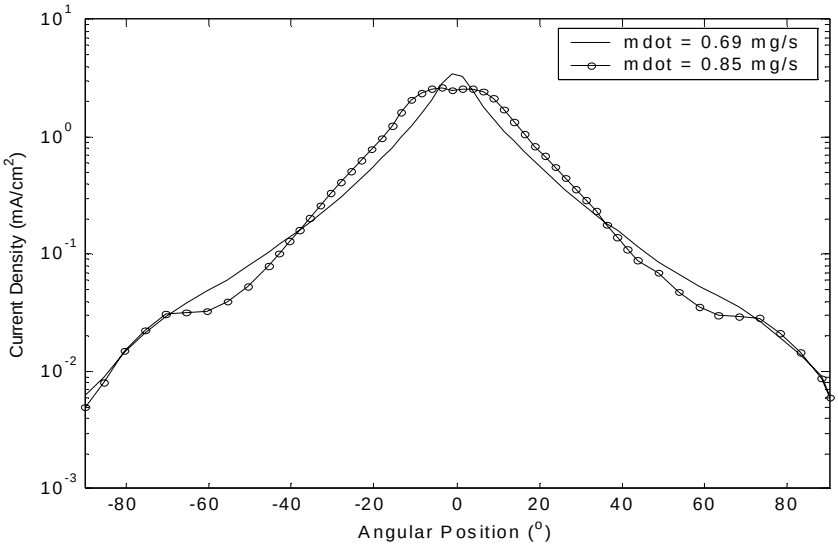

Figure 4.11 Effect of flow rate on the current density distribution. V_D = 300V, P = 4.0×10^{-6} Torr, and sweep radius = 25cm.

At higher flow rates, more xenon propellant is ionized causing a higher current density to be attained. While there is good agreement with this phenomenon in the mid-angle region, this pattern is not consistent at the wings and at the centerline.

It can be deduced from Figures 4.9 through 4.11 that the flow rate does not affect the wings of the current density distributions. As explained previously, the wings are mainly affected by the accumulation of charge exchange ions, whose density is dependent on the density of neutrals. There are two populations of neutrals in the vacuum tank, background neutrals and neutral xenon propellant. Non-ionized xenon propellant accounts for only 10-15% of the total propellant. This amount is significantly smaller than the density of background neutrals that are available in the vacuum tank. Therefore, the charge exchange ions are mostly dependent on the density of background neutrals.

However, at the centerline, an increase in flow rate brings about a decrease in current density, probably due to elastic collisions of high energy ions. Elastic collisions occur when a fast moving ion collides with a neutral, and scatters without charge exchange. With a high flow rate, a greater density of high energy ions is created, which increases the probability

of elastic collisions. The scattering of high energy ions leads to a decrease in current density at the centerline and an increase in another position of the distribution. Figure 4.9 shows an exception to the above mentioned phenomenon. Since this exception occurs at the highest background pressure, it can be explained by the fact that background neutrals are ionized, thus increasing the current density at the centerline and compensating for the loss of current density due to scattering.

4.2.4 Effect of Sweep Radius

Current density measurements were taken at radii of 25 and 47 cm. Figures 4.12 and 4.13 display the effects of sweep radius on current density distribution at flow rates of 0.69 mg/s and 0.85 mg/s respectively and discharge voltages of 300V and 250V respectively. The background pressure for all cases was 2.2×10^{-5} Torr.

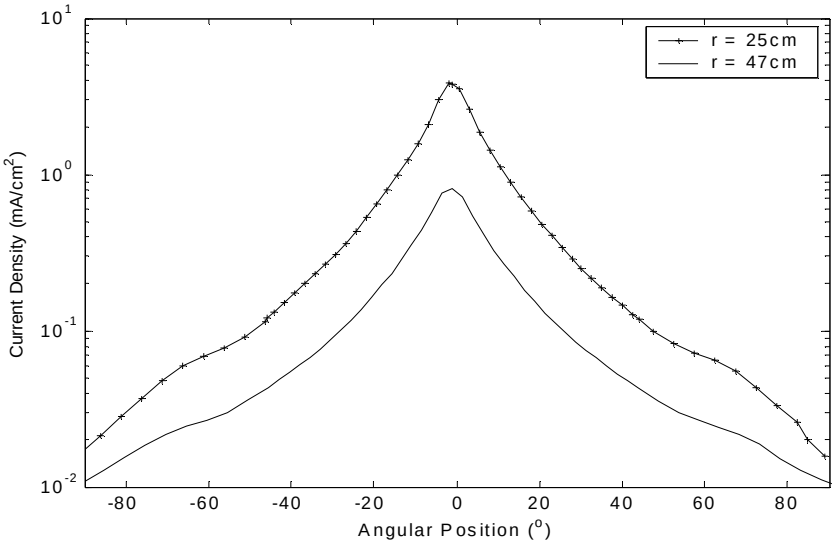

Figure 4.12 Effect of sweep radius on the current density distribution. V_D = 300V, $\dot{m}$ = 0.69 mg/s, and P = 2.2x10^{-5} Torr.

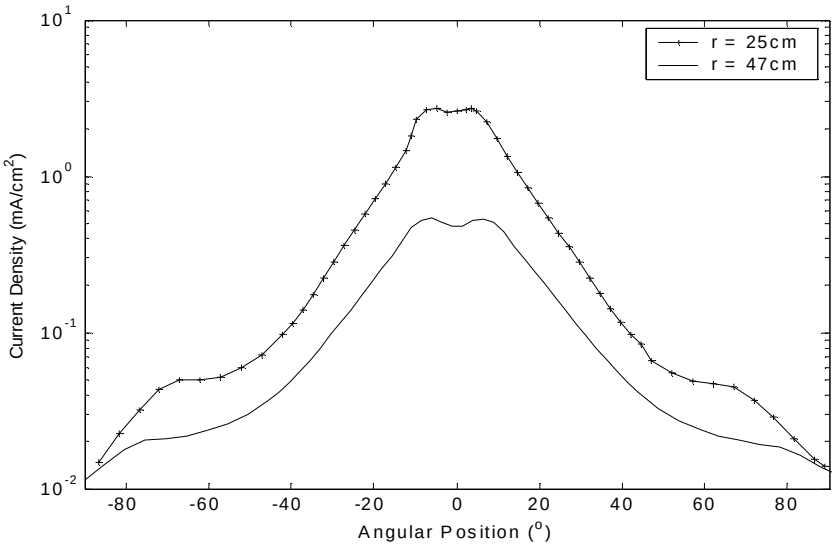

Figure 4.13 Effect of sweep radius on the current density distribution. V_D = 250V, $\dot{m}$ = 0.85 mg/s, and P = 2.2x10^{-5} Torr.

As seen from Figures 4.12 and 4.13, the current density decreases with an increase in sweep radius. In each figure, the profile has the same characteristics for both radii. In Figure 4.13, both distributions have a double hump at the centerline and shoulders at the wings, while in Figure 4.12 both distributions have a peak at the centerline and slightly less distinct shoulders at the wings.

It is expected that current density decreases with an increase in sweep radius. Current density is represented as ion flux through a given solid angle $d\Omega$

$$j(r) = \frac{1}{r^2}\frac{dI}{d\Omega} \tag{4.1}$$

where $j(r)$ is current density at a sweep radius r and I is current. Therefore, assuming conical flow (i.e., ions remain within the same $d\Omega$ at different radii), the relationship between current densities at different radii is

$$\frac{j(r_1)}{j(r_2)} = \left(\frac{r_2}{r_1}\right)^2 \tag{4.2}$$

Current density measurements at a 25 cm sweep radius were scaled to current density at a 47 cm sweep radius using equation (4.2) compared to measurements at 47 cm. Figures 4.14 and 4.15 represent a comparison of scaled and measured current density at a sweep radius of 47 cm for flow rates of 0.69 mg/s and 0.85 mg/s respectively.

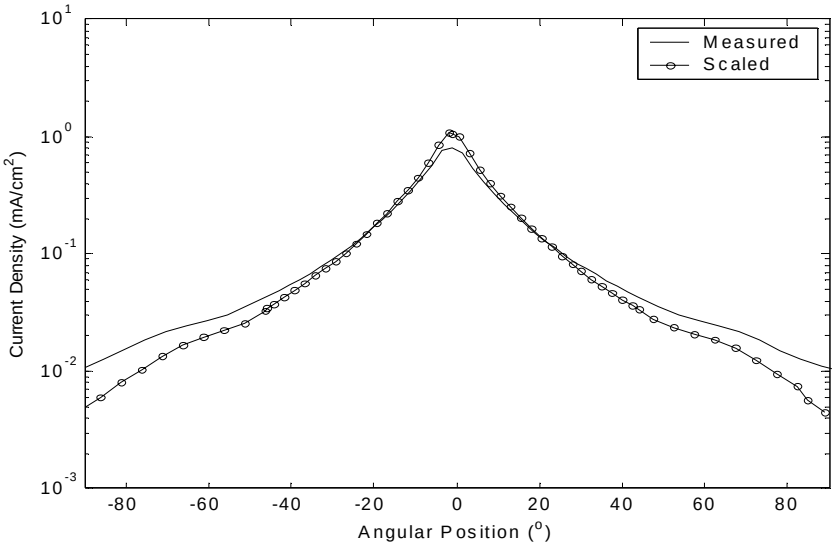

Figure 4.14 Comparison of scaled and measured current density distributions. V_D = 300V, $\dot{m}$ = 0.69 mg/s, P = 2.2x10^{-5} Torr, and sweep radius = 47cm.

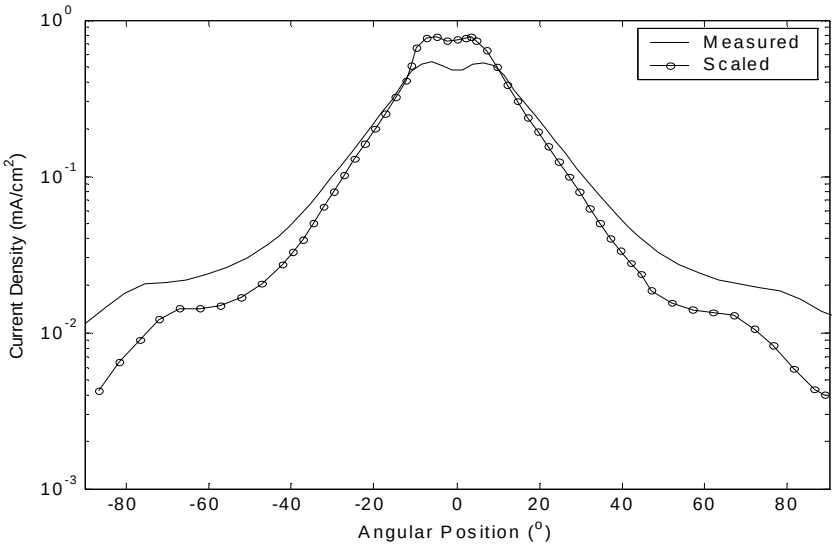

Figure 4.15 Comparison of scaled and measured current density distributions. V_D = 250V, $\dot{m}$ = 0.85 mg/s, P = 2.2x10^{-5} Torr, and sweep radius = 47cm.

As seen from Figures 4.14 and 4.15, the scaling relationship from equation (4.2), does not hold at the wings of the current density distribution, where charge exchange collisions dominate. The assumption that flow remains conical is not correct because charge exchange collisions peak at $\pm 70°$. Therefore, charge exchange flux is not scalable by equation (4.2).

Figure 4.14 shows good agreement, whereas Figure 4.15 shows poor agreement, between scaled and measured current density in the mid-angle region. The deficiency in measured current density is probably due to elastic collisions, as explained in section 4.2.3. This deficiency occurs at the higher flow rate case, where there is an increased probability of elastic collisions, thereby reducing current density.

4.3 Plume Divergence

4.3.1 Beam Current

The current density distribution is integrated to produce the total plume beam current. The distribution is symmetric with respect to the centerline throughout the tests. Using an axi-symmetric plume, the beam current, I_b, is calculated by

$$I_b = 2\pi r^2 \int_0^{\frac{\pi}{2}} j(\theta) \sin\theta d\theta \tag{4.3}$$

where r, sweep radius, is 25 cm, j is current density, and θ is angular position. Table 4.1 shows the beam current results for the BHT-200 operating conditions, shown in Table 3.2.

TABLE 4.1 Beam current results for the BHT-200 Hall thruster

V_D (V)	I_D (A)	I_{beam} (A)	I_{beam}/I_D	Pressure (Torr)
225	0.888	0.819	0.92	8.0×10^{-5}
225	0.824	0.717	0.87	2.2×10^{-5}
225	0.792	0.679	0.85	4.0×10^{-6}
250	0.878	0.822	0.94	8.0×10^{-5}
250	0.797	0.666	0.83	2.2×10^{-5}
250	0.795	0.688	0.87	4.0×10^{-6}
300	0.878	0.824	0.94	8.0×10^{-5}
300	0.817	0.74	0.91	2.2×10^{-5}
300	0.800	0.711	0.89	4.0×10^{-6}

A general characteristic of Hall thrusters is that about one-third of the electron current emitted by the cathode will flow into the discharge channel and will be collected by the anode, while the remaining two-thirds will flow away from the thruster to neutralize the

beam. Therefore, the beam current in the plume is approximately 67% of the discharge current [15]. However, the results of this research show that the ratio of beam current to discharge current ranges from 80% to 93%. This ratio is higher than expected because of the additional current provided by the ionization of background neutrals and charge exchange ions. To reach the expected beam current to discharge current ratio of 67%, it is necessary to repel low energy ions. However, the Faraday probe used in this research does not repel any low energy ions. Attempts to repel these ions were made using a Faraday probe with a positively biased grid in front of the collector. A detailed description of its results are provided in Appendix B.

4.3.2 Half-Angle Plume Divergence

The half-angle plume divergence is based on 95% of the beam current and is calculated using the following equation:

$$0.95 I_b = 2\pi r^2 \int_0^{\theta'} j(\theta) \sin\theta d\theta \tag{4.4}$$

where θ' is the half-angle plume divergence. The plume divergence angle ranges from 60° at a pressure of 4.0×10^{-6} Torr to 75° at a pressure of 8.0×10^{-5} Torr. These divergence angles are relatively larger than others found in Hall thruster plume literature, [10], because the instrument used to measure them is a nude Faraday probe that does not repel low energy ions as discussed previously. The actual divergence angles of the BHT-200 plume may be smaller, if measured in hard vacuum and beyond the radius at which charge exchange ions from engine neutrals concentrate.

Figure 4.16 shows the half-angle plume divergence versus the discharge voltage as the background pressure increases. The plume divergence increases as the pressure increases because of the ionization of background neutrals and the increase of charge exchange ions, which are pushed further radially by the positive potential of the beam. On the other hand,

increasing the discharge voltage has only a small and not fully understood effect on divergence.

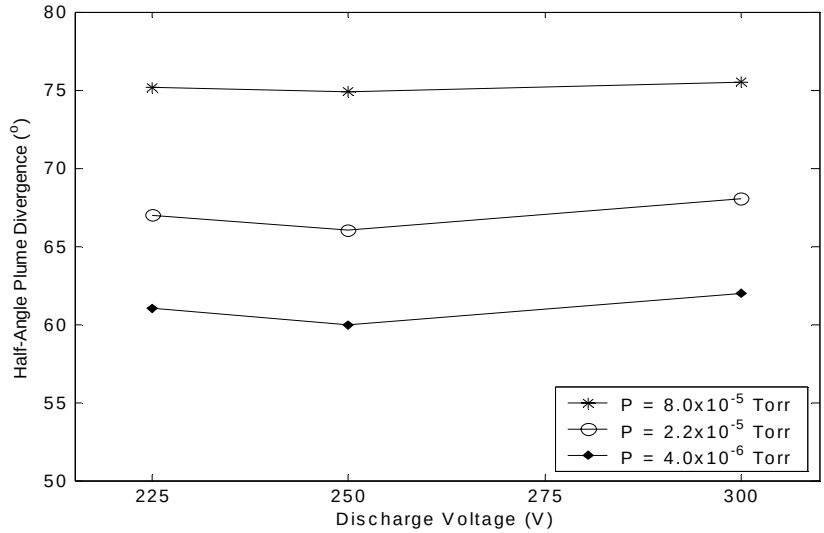

Figure 4.16 Results of 95% current plume divergence half-angle at various discharge voltages and background pressures

4.4 Comparison to Simulation Results

S. Cheng et al. performed a simulation to characterize the BHT-200 Hall Thruster plume in a vacuum tank [3, 16]. This simulation is a Hybrid-PIC model with neutrals and ions modeled as particles and electrons modeled as a fluid. It uses a 3-D unstructured tetrahedral grid. The source model includes separate distributions for different ion populations. The electric potential is calculated by assuming either constant or polytropic electron temperature in quasi-neutral regions. Both the elastic and charge exchange collisions are modeled using a No-Time-Counter Direct Simulation Monte Carlo (NTC DSMC) model. Further details of this simulation are described in reference [16].

Figure 4.17 shows a comparison of current density distributions for the simulation and experimental results. The data in the figure represent measurements taken at a discharge voltage of 300V, pressure of 2.2×10^{-5} Torr, and sweep radius of 25cm. As can be seen in

the figure, there is good agreement between simulation and experimental results. The simulation current density is slightly under-predicted at the wings. There are still some gridding and source model issues in the simulation, which may explain the discrepancy in current density at the wings.

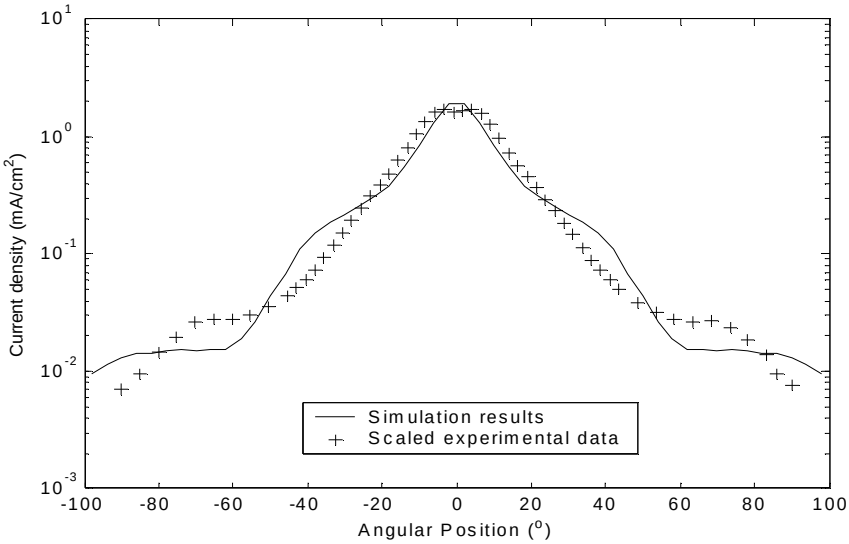

Figure 4.17 Comparison of simulation and experimental results. V_D = 300V, P = 2.2x10^{-5} Torr, and sweep radius = 25cm.

4.5 Analytical Estimation of CEX Flux

In this section, a simple model is used for estimating the amount of charge exchange (CEX) flux produced in a vacuum tank from a Hall thruster plume. This estimated CEX flux will be compared to measured flux.

The CEX current is given by

$$I_{CEX} = \int_0^L dx \int_A e n_i \sigma_{CEX} \upsilon_i n_n dA \tag{4.5}$$

Since $\sigma_{CEX} = const$ and $\int_A e n_i \upsilon_i dA = I_b$ (independent of x), the CEX current is

$$I_{CEX} = I_b \sigma_{CEX} \int_0^L \overline{n_n} dx \tag{4.6}$$

where I_b is beam current, $\sigma_{CEX} \cong 55 \times 10^{-20} m^2$ is the CEX collision cross-section, $\overline{n_n}$ is the neutral density averaged in the cross-section of the ion beam, and L is the length of the vacuum chamber. As described earlier and shown in equation (4.6), CEX flux is dependent on neutrals. There are two populations of neutrals, engine and background neutrals. The current in equation (4.6) will be divided into two parts, CEX current produced from engine neutrals and CEX current produced from background neutrals.

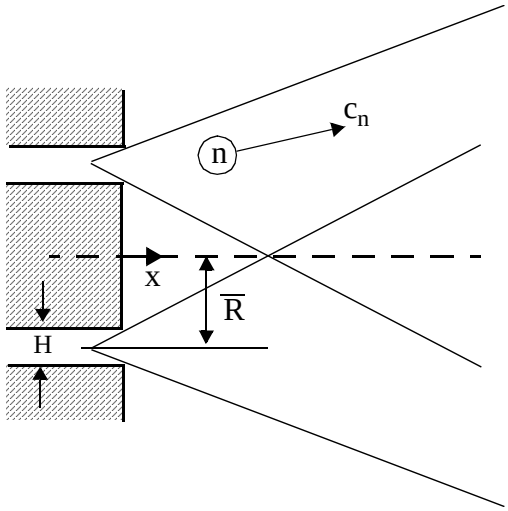

Figure 4.18 Hall thruster cross-section defining some geometry parameters.

4.5.1 CEX Flux from Engine Neutrals

Engine neutrals are the portion of the propellant that is not ionized. These neutrals are ejected from the engine at a rate given by

$$\dot{m}_n = (1 - \eta_u)\dot{m} \tag{4.7}$$

where η_u is the utilization efficiency, and $\dot{m}$ is the total flow rate. The engine neutral density is then calculated by

$$n_n^{eng} \cong \frac{1-\eta_u}{\eta_u} \frac{1}{2\pi \bar{R} H e c_n} \frac{I_b}{\left(1+\frac{x}{H}\right)^2} \tag{4.8}$$

where $\bar{R}$ is shown in Figure 4.18, H is engine channel height, c_n is the speed of the neutrals, and the factor $\left(1+\frac{x}{H}\right)^2$ is an approximation to the ratio $\frac{A(x)}{A(0)}$ of beam areas. Equation (4.8) is substituted in equation (4.6) to yield CEX current produced from engine neutrals. Since most of the CEX production from engine neutrals occurs near the engine and $L \gg \bar{R}$, therefore setting $L \to \infty$, an expression for the CEX current produced from engine neutrals is obtained:

$$I_{CEX}^{eng} \cong \frac{1-\eta_u}{\eta_u} \frac{I_b^2 \sigma_{CEX}}{2\pi \bar{R} e c_n} \tag{4.9}$$

Assuming CEX ions from engine neutrals issue from a small region uniformly into the forward hemisphere, the CEX flux at a distance r is given by

$$j_{CEX}^{eng} = \frac{I_{CEX}^{eng}}{2\pi r^2} \tag{4.10}$$

Substituting equation (4.9) into equation (4.10), the expression for CEX flux due to engine neutrals is

$$j_{CEX}^{eng} = \frac{1-\eta_u}{\eta_u} \left(\frac{I_b}{2\pi r}\right)^2 \frac{\sigma_{CEX}}{\bar{R} e c_n} \tag{4.11}$$

At a distance of 25 cm, the CEX flux due to engine neutrals is estimated to be 0.00244 mA/cm^2, where $\eta_u = 0.8$, $I_b = 0.666$ A, and $c_n = 180$ m/s.

It must be noted that the assumption of uniform emission of CEX ions in the forward hemisphere is very rough. Numerical results suggest a “cylindrical dipole” type of distribution, centered about the 90° position.

4.5.2 CEX Flux from Background Neutrals

The presence of background neutrals is solely dependent on the background pressure of the vacuum tank. Their density is calculated using

$$n_n^{bkg} = \frac{P^{bkg}}{kT^{bkg}} \tag{4.12}$$

where P^{bkg} and T^{bkg} are the background pressure and temperature respectively and k is the Boltzmann constant.

The CEX emission due to background neutrals is evenly distributed along the beam of the plume. By superimposing emissions from differential source elements distributed between $x = 0$ and $x = L\cos\theta$, each emitting uniformly into the forward hemisphere, it can be shown that CEX flux at a distance r due to background neutrals is determined by

$$j_{CEX}^{bkg} \cong \frac{n_n^{bkg}\sigma_{CEX}I_b}{2\pi r\tan\theta} \tag{4.13}$$

At a distance of 25 cm and a background pressure of 2.2×10^{-5} Torr, the calculated CEX flux due to background neutrals is plotted in Figure 4.19 for angles between $60°$ and $90°$, where charge exchange collisions dominate.

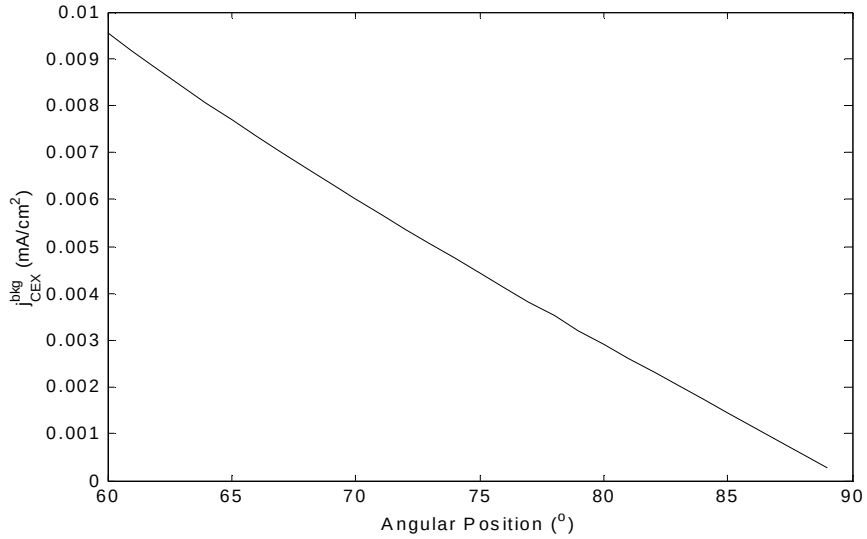

Figure 4.19 Contribution of background neutrals to the CEX flux. P = $2.2\text{x}10^{-5}$ and sweep radius = 25cm.

4.5.3 Comparison of Estimated and Measured CEX Flux

The total estimated CEX flux, which consists of summing the flux from equations (4.10) and (4.12), was compared to measured flux at angles between $60°$ and $90°$ for a background pressure of 2.2×10^{-5} Torr, as shown in Figure 4.20.

From Figure 4.20, the experimental flux is 5 times greater than the estimated CEX flux. This discrepancy is partly due to CEX emission being distributed at the wings rather than being forward isotropic. In addition, the measured flux between $60°$ and $90°$ is not entirely CEX flux, but also consists of ions that were scattered to the wings.

The main usefulness of equations (4.11) and (4.13) resides in their scaling dependences. For example, by comparing them, one can estimate a minimum vacuum level for tank measurements to be representative of space operation:

$$n_n^{bkg} \ll \frac{1-\eta_u}{\eta_u}\frac{I_b \tan\theta}{2\pi r \bar{R}ec_n} \tag{4.14}$$

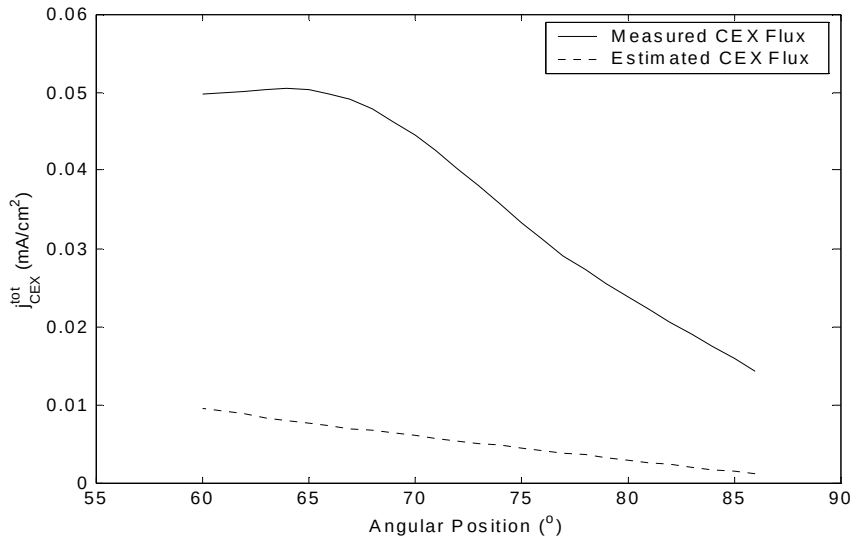

Figure 4.20 Comparison between measured and estimated CEX flux. V_D = 250V, P = 2.2x10^{-5}, and sweep radius = 25cm.

For this case, it would require that n_n^{bkg} « 2.4×10^{16} m^{-3}, or P^{bkg} « 7.5×10^{-7} Torr, which is a difficult task. This might be reachable with "pumping speeds" of 290,000 L/s. However, there are only a few tanks in the US that have high pumping speeds capable of maintaining pressures under 10^{-7} Torr.

Chapter 5

EMISSIVE PROBE EXPERIMENTAL METHODS

5.1 Probe Requirement

In addition to current density measurements obtained with the Faraday probe, plasma potential, electron temperature, and electron density are needed to further map the BHT-200 thruster plume. As explained in Chapter 2, accurate measurements of plasma potential are obtained using an emissive probe, and measurements of electron temperature and density are obtained using a Langmuir probe. An emissive probe measures plasma potential when its filament is heated to start electron emission. However, when the emissive probe filament is cold, the probe is equivalent to a Langmuir probe. Therefore, an emissive probe was used to measure plasma potential in its heated state and electron temperature and density in its cold state.

The emissive probe consists of a filament, a small loop of conducting wire at the tip of the probe, in a double bore ceramic tube. The filament, the emitting portion of the probe that is usually made of tungsten, is heated by an external current to start electron emission and needs to withstand high temperatures in order to avoid melting. Therefore, the amount of external current applied should be small in order to avoid melting the filament, yet, it should be large enough to start and sustain electron emission. The emissive probe emits electrons when the probe bias is smaller than plasma potential, and collects electrons when the probe bias is larger than the plasma potential. Both electron collection and emission are dependent on the size of the filament. A large filament would lead to a large electron

collection, which could perturb the plasma. However, a small filament size might at low heating currents. Therefore, an optimal filament size is required to minimize electron collection and ensure adequate electron emission.

5.2 Probe Thermal Model

To satisfy the probe requirements, a thermal model was developed to determine an optimal emissive probe design, which encompasses an appropriate filament size and heating current. This thermal model consists of heat transfer analysis of the probe's filament, which is in thermal balance between ohmic heating, plasma heating, radiation, emissive cooling, and heat conduction.

The heat transfer analysis models the thermal balance of the filament in two regimes, an emissive regime where the probe potential is smaller than the plasma potential and the collecting regime where the probe potential is larger than the plasma potential. This model predicts the temperature of the filament as a function of the probe potential.

Electrons are collected by the filament when the probe voltage is larger than the plasma potential because electrons travel up the potential gradient. When the probe potential is smaller than the plasma potential, the electrons are retarded and the filament collects only the high energy electrons. Therefore, the electron collection is dependent on the difference between the probe voltage and the plasma potential, and is described by

$$I_e = \begin{cases} e\frac{n_e \bar{c}_e}{4} e^{\frac{e\Delta\phi}{kT_e}} \pi D_f L_f & (\Delta\phi < 0) \\ e\frac{n_e \bar{c}_e}{4} \pi D_f L_f & (\Delta\phi > 0) \end{cases} \tag{5.1}$$

where n_e is electron density, D_f and L_f are filament diameter and length, T_e is electron temperature, k is the Boltzmann constant, $\Delta\phi = V_{probe} - \phi_{plasma}$ is the difference

between probe potential and plasma potential, and $\bar{c}_e$, the thermal velocity of electrons, is determined by $\bar{c}_e = \sqrt{\frac{8kT_e}{\pi m_e}}$.

Therefore, the heating contributed by the electron collection is

$$Q_e = \begin{cases} e\frac{n_e \bar{c}_e}{4} e^{\frac{e\Delta\phi}{kT_e}} \pi D_f L_f \left(\frac{2kT_e}{e} - \Delta\phi\right) & (\Delta\phi < 0) \\ e\frac{n_e \bar{c}_e}{4} \pi D_f L_f \left(\frac{2kT_e}{e} + \Delta\phi\right) & (\Delta\phi > 0) \end{cases} \tag{5.2}$$

Ions are collected by the filament only when the probe voltage is smaller than the plasma potential because ions travel down the potential gradient. The current due to ion collection is described by

$$I_i = \begin{cases} 0.61 e n_e \upsilon_B \pi D_f L_f & (\Delta\phi < 0) \\ 0 & (\Delta\phi > 0) \end{cases} \tag{5.3}$$

where υ_B, the Bohm velocity, is determined by $\upsilon_B = \sqrt{\frac{kT_e}{m_i}}$.

From equation (5.3), the heating contributed by the ions is

$$Q_i = \begin{cases} 0.61 e n_e \upsilon_B \pi D_f L_f \left(\frac{2kT_i}{e} - \Delta\phi\right) & (\Delta\phi < 0) \\ 0 & (\Delta\phi > 0) \end{cases} \tag{5.4}$$

where T_i is ion temperature.

The probe is also heated by the external current. Since the metal's resistivity is temperature-dependent according to $\frac{1}{\sigma} = \frac{T}{c}$, this ohmic heating is calculated by

$$Q_{oh} = \frac{L_f I^2}{c A_f} T_f \tag{5.5}$$

where $c = 4.2\times10^{9}(\Omega mK)^{-1}$, T_f and A_f are the temperature and area of the filament respectively, and I is the heating current.

In addition to electron, ion, and ohmic heating, the filament is also subject to cooling by electron emission, radiation, and heat conduction. Electron emission occurs when the probe potential is smaller than the plasma potential. The current due to emission is calculated by

$$I_{em} = \begin{cases} a\pi D_f L_f T_f^2 e^{-\frac{e\psi}{kT_f}} & (\Delta\phi < 0) \\ 0 & (\Delta\phi > 0) \end{cases} \tag{5.6}$$

where $a = 4\times10^{5}A/m^2/K^2$ and ψ is the material work function of the filament.

Therefore, cooling by electron emission is

$$Q_{em} = \begin{cases} a\pi D_f L_f T_f^2 e^{-\frac{e\psi}{kT_f}}\left(\frac{2kT_f}{e} + \psi\right) & (\Delta\phi < 0) \\ 0 & (\Delta\phi > 0) \end{cases} \tag{5.7}$$

Radiative cooling is calculated (including a temperature-dependent emissivity of tungsten $\varepsilon = \varepsilon_1 T^{3/2}$) by

$$Q_{rad} = \varepsilon_1 \sigma_B \pi D_f L_f T_f^{\frac{11}{2}} \tag{5.8}$$

where $\varepsilon_1 = 6.3\times10^{-6}K^{-\frac{3}{2}}$ and $\sigma_B = 5.67\times10^{-8}W/m^2/K^4$.

The final term is heat conduction, where heat is conducted away from the filament to the encapsulated portion of the probe. Assuming a constant thermal conductivity, $K_{th} = 81w/m/K$ and metal's resistivity is dependent on temperature according to $\frac{1}{\sigma} = \frac{T}{c}$, the temperature distribution in the encapsulated portion of the probe is determined by,

$$\frac{\mathrm{d}^2 T}{\mathrm{d}x^2} + \frac{1}{\lambda^2} T = 0 \tag{5.9}$$

where $\lambda = \sqrt{\frac{K_{th} A_{en}^2 c}{I^2}}$, A_{en} is the area of the encapsulated portion of the probe, and I is the heating current. Using equation (5.9), the heat conduction is determined by

$$Q_c = 2K_{th}\left(\frac{\mathrm{d}T}{\mathrm{d}x}\right)_L \tag{5.10}$$

Using the boundary conditions defined by the temperatures, T_0 and T_f at the wall and the filament respectively, the heat conduction is solved:

$$Q_c = 2\frac{K_{th} A_{en}}{\lambda \sin\frac{L_{en}}{\lambda}}\left(T_f \cos\frac{L_{en}}{\lambda} - T_0\right) \tag{5.11}$$

where L_{en} are the length of the encapsulated portion of the probe respectively.

As explained earlier, the filament is modeled to be in a thermal balance so that

$$Q_e + Q_i + Q_{oh} = Q_{em} + Q_{rad} + Q_c \tag{5.12}$$

An iterative process is performed to solve equation (5.12) for the temperature of the filament. This temperature is a function of the probe voltage and heating current. For a particular filament size, filament material, and heating current, the filament temperature is iterated until a solution is found for each probe voltage. For each filament size, the process is repeated for different materials and heating currents. The filament sizes that were considered ranged from 0.125 mm to 0.5 mm in diameter and 1 mm to 10 mm in length. The materials considered were tungsten for its high melting point and thoriated tungsten for its low work function, which enables electron emission at low temperatures. The heating current applied in the model ranged from 0A to 6A. Figure 5.1 shows the temperature-voltage profile of a thoriated tungsten filament 0.125 mm in diameter and 6 mm in length as the heating current is increased. A pool of filament sizes and heating currents were

selected after each computational run, based on the requirement that the temperature did not exceed the melting point of the filament material.

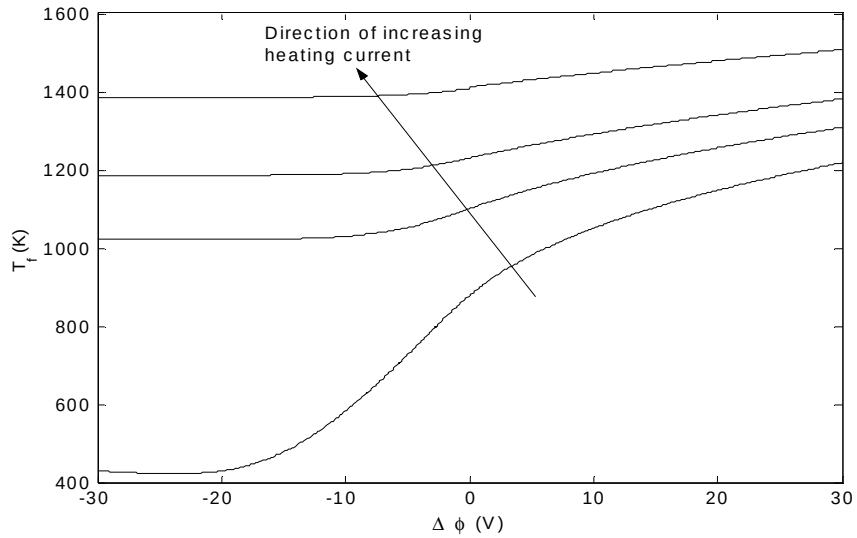

Figure 5.1 Filament temperature profile at different heating currents. An increase in heating current increases the filament temperature. The thoriated tungsten filament is 0.125 mm in diameter and 6 mm in length.

From equations (5.1) and (5.3), both electron and ion currents are independent of heating current and are directly proportional to filament size. Therefore, minimizing the electron current in order to avoid plasma perturbations leads to a small filament size.

The electron emission current is also proportional to the filament size. Since it is desired to minimize the filament size in order to minimize electron current, the small filament size might melt due to excessive heating. However, from equation (5.6), the emitted current is also dependent on the work function. Therefore, a low work function would increase emitted current without the need for high heating currents. Therefore, the selected design should be a small filament size with a low work function and a heating current that would not bring the temperature of the filament to the melting point.

After several iterations, the designed emissive probe was a 1% thoriated tungsten filament with a 2.65 eV work function that is 0.125 mm in diameter and 6 mm in length, which is exposed to the plasma. The heating current needed for adequate emission is 2A. Figures 5.2 and 5.3 portray collected and emitted current versus voltage for the designed emissive probe respectively, at different heating currents.

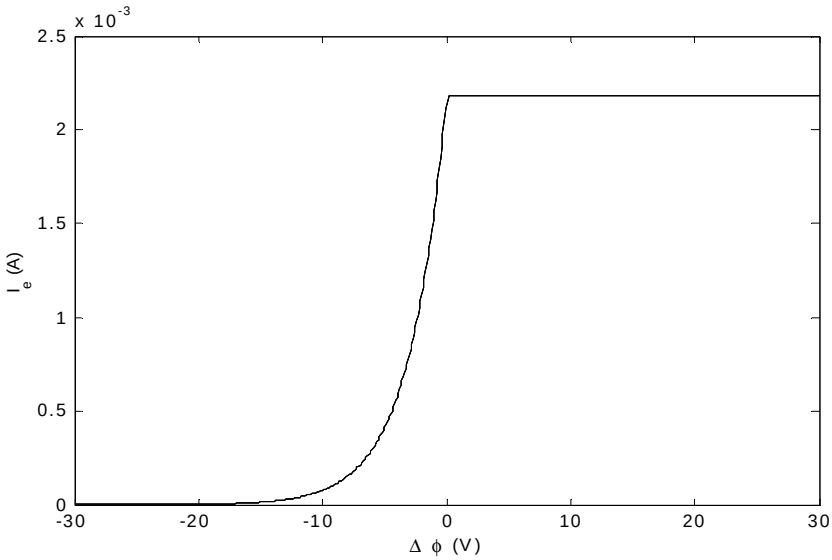

Figure 5.2 Collected current profile for a 0.125 mm diameter and a 6 mm length filament. The collector current is not affected by the heating current.

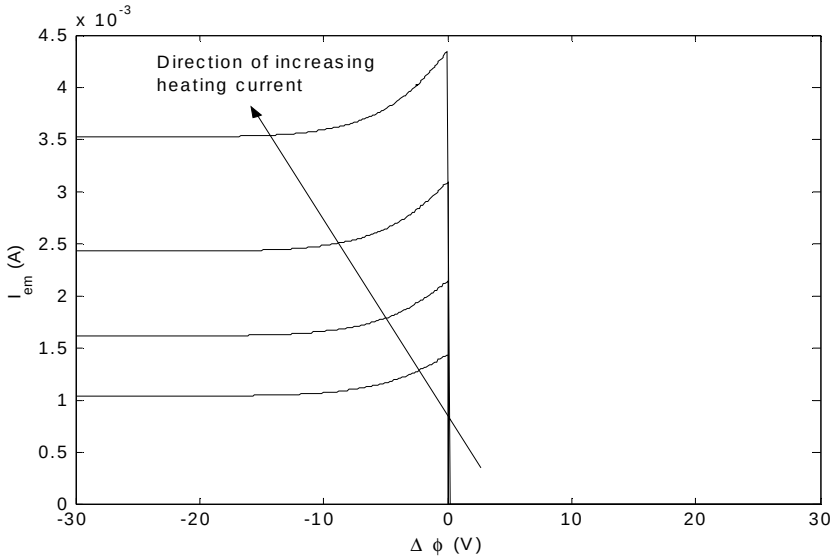

Figure 5.3 Emitted current profile for a 0.125 mm diameter and a 6 mm length filament. The emitted current increases with an increase in heating current.

To plot the I-V characteristic curve, the total current is calculated by

$$I_{tot} = I_e - I_i - I_{em} \tag{5.13}$$

Figure 5.4 portrays the I-V characteristic curve of the designed probe at different heating currents. After several iterations, the heating current needed for a visible "knee" in the I-V characteristic curve was found to be 2A.

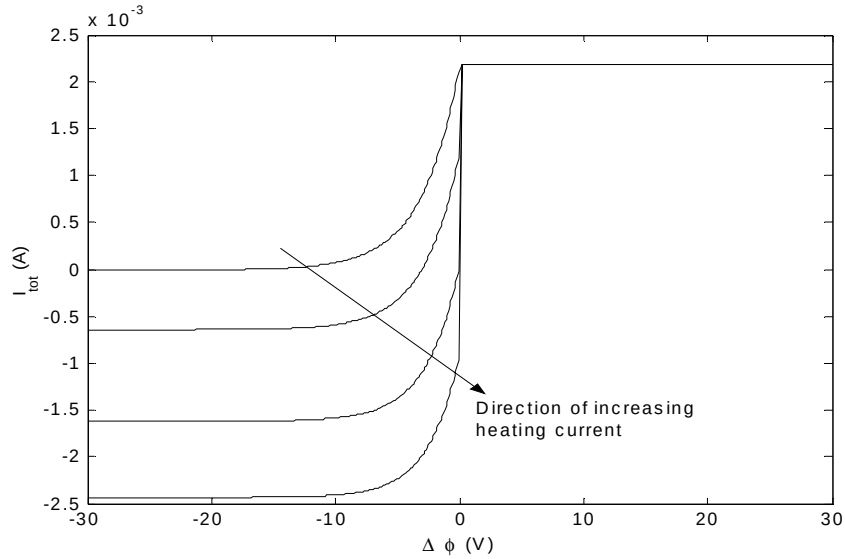

Figure 5.4 I-V characteristic curve for the emissive probe at different heating currents. The increase in heating current leads to a steep drop in current at the plasma potential. The filament is 0.125 mm in diameter and 6 mm in length.

This thermal model can only be used as a tool for design of the emissive probe. The I-V curve obtained cannot be compared to experimental results because of certain assumptions made in the model. For example, the current collected is modeled to attain a constant value when the potential of the probe is larger than the plasma potential. However, experimentally, the magnitude of the current slowly increases which reflects a 3-D orbital motion regime as mentioned in Chapter 2.

5.3 Probe Construction

The construction of the emissive probe is straightforward and does not require spotwelding. Figure 5.5 portrays a schematic of the emissive probe. A 1% thoriated tungsten wire passes through the entire length of a double-bore ceramic tube and forms a loop at the tip of the probe. The thoriated tungsten wire is 0.125 mm in diameter with 6 mm of exposed filament in the plasma. The ceramic tube is 99.8% pure alumina with an inside diameter of 0.79 mm, an outside diameter of 3.18 mm, and a length of 107 mm. A nickel lead, with a diameter of 0.5 mm, was inserted in each bore of the ceramic tube for electrical connec-

tions. Once the thoriated tungsten wire and the nickel leads were placed inside the ceramic tube, additional thoriated tungsten wire was inserted into the bores to ensure good contact between the thoriated tungsten wire and the nickel leads.

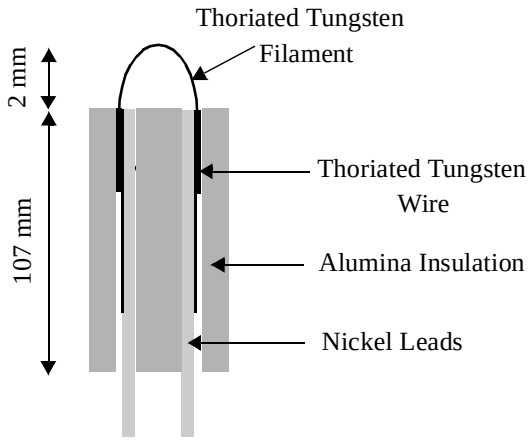

Figure 5.5 Schematic of the emissive probe design.

5.4 Experimental Setup

5.4.1 Vacuum Facility

Plasma potential, electron temperature and density measurements were conducted at the MIT Space Propulsion Laboratory (SPL) vacuum facility. The vacuum chamber, shown in Figure 5.6, is 1.5 m in diameter and 2 m in length. The vacuum chamber is equipped with a mechanical pump for roughing, and two cryopumps, CT-10 and OB-400, to achieve an Ultra-High Vacuum. The cryopumps are capable of a 7000 L/s pumping speed for xenon with a base pressure of 2×10^{-8} Torr. The chamber pressure is monitored by a thermocouple gauge for a pressure range greater than 10^{-3} Torr, and by a cold-cathode gauge for pressures ranging from 10^{-4} to 10^{-9} Torr. Both pressure gauges are controlled by a Varian Multi Gauge Controller. Pressure measurements from the cold-cathode gauge were corrected for xenon by equation (3.3).

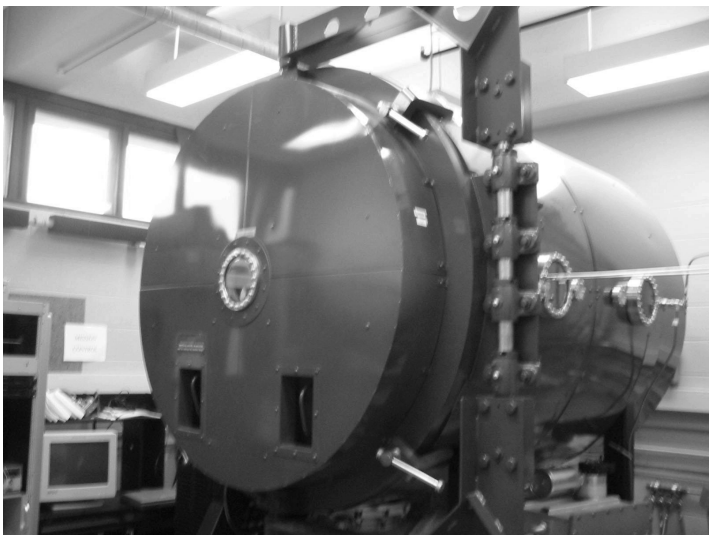

Figure 5.6 MIT vacuum chamber.

The vacuum chamber is also equipped with five windows, five feedthroughs for electrical connections, and six fluid feedthroughs. A target, which is a cooling plate, is installed at the back of the chamber to remove the BHT-200 heat load from the chamber. The target is also intended to catch the sputtered material in the thruster plume and to inhibit material deposition on the chamber walls.

The xenon flow system, depicted in Figure 5.7, consists of a xenon tank, a regulator, three needle valves, and two flow meters. Xenon is delivered at 40 psi from a 25L tank using a two-stage regulator, and flows through two 1/4 in diameter stainless steel tubes to the thruster anode and cathode respectively. The flow rate is regulated by an Omega Engineering flow meter with a 0.1 to 1 mg/s range for xenon.

5.4.2 Hall Thruster Setup

Similar to the thruster setup described in Section 3.3.2, the BHT-200 was mounted inside the MIT vacuum tank on top of a two-shelved bridge. The thruster was positioned so that the plume was allowed to freely expand approximately 1.5 m along the centerline axis. The thruster was operated for an hour before any data collection to allow the discharge

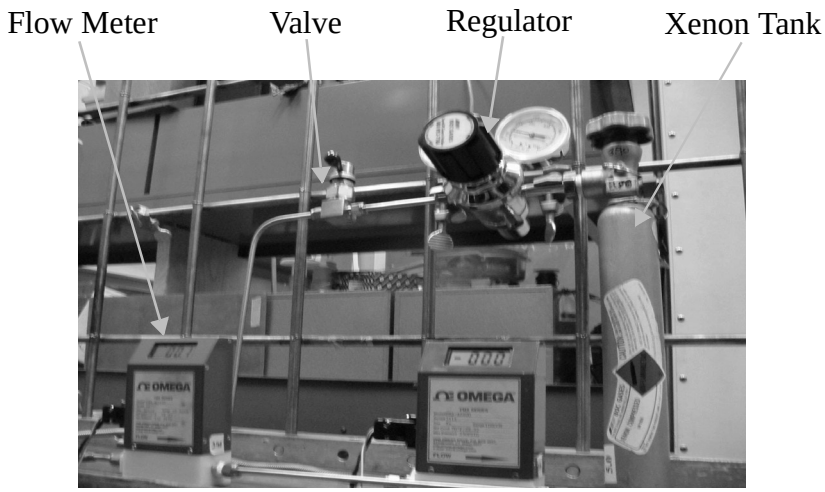

Figure 5.7 Xenon flow system for the BHT-200 Hall thruster.

chamber walls to outgas and reach a thermal steady-state. The emissive probe measurements were taken at different thruster operating conditions. Table 5.1 summarizes the thruster operating conditions at which data were acquired.

TABLE 5.1 BHT-200 operating conditions for emissive probe measurements.

V_D (V)	I_D (A)	Anode Flow (mg/s)	Cathode Flow (mg/s)	Pressure (Torr)
200	0.805	0.85	0.1	3.2×10^{-5}
250	0.800	0.85	0.1	3.2×10^{-5}
300	0.773	0.85	0.1	3.2×10^{-5}

5.4.3 Emissive Probe Setup

Similar to the Faraday probe setup described in Section 3.3.3, the probe was mounted on a rotating arm facing the exit plane of the thruster. The probe was oriented such that the plane of the emitting loop was perpendicular to the arm's radial direction. The arm was swept $\pm 90^\circ$ from the thruster centerline through the plume in 20° increments at a radius of 25cm. Also, the emissive probe was heated by a half-wave rectified sine wave. The heating voltage was provided by a Variac that was connected to an isolation transformer,

which provided high AC currents at low voltages. To avoid a voltage drop across the probe's filament due to the heating current, measurements were taken during the off-heat half cycle. Figure 5.8 provides the electrical schematic of the emissive probe. The current-voltage scans were performed using a Hiden Analytical SourceMeter. The data was recorded using an ESPion software from Hiden Analytical. Each current-voltage scan was completed in less than one minute, and the arm was swept across the thruster plume from –90° to 90° in 45 minutes.

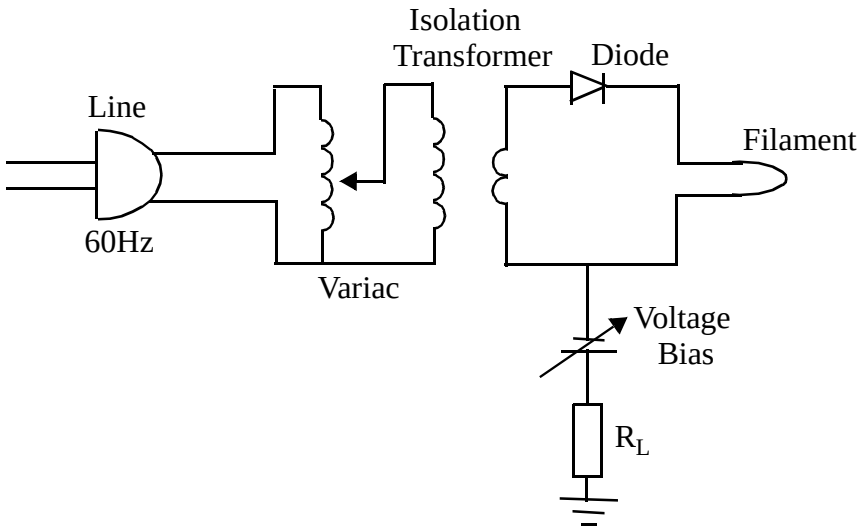

Figure 5.8 Electrical schematic of an emissive probe [9].

Chapter 6

EMISSIVE PROBE RESULTS

6.1 Overview

This chapter presents emissive probe results at the thruster operating conditions described in Chapter 5. Plasma potential measurements were acquired with the emissive probe, which was heated with an external current. Electron temperature and density measurements were acquired with the cold probe, in which no heating current was supplied to the emissive probe. The effects of discharge voltage and sweep radius on plasma potential were investigated. Additionally, this chapter presents a comparison of experimental and simulation data.

6.2 I-V Characteristic Curves

Emissive probe data collection was performed using current-voltage scans, which consisted of sweeping the probe voltage from –50V to 50V and measuring current collected at each voltage. The measured current was plotted against the probe voltage to produce an I-V characteristic curve. Also, the emissive probe was swept across the BHT-200 thruster plume from –90° to 90° in 20° increments. I-V characteristic curves were produced for each angular position. This process was repeated for each of the thruster operating conditions described in Table 5.1.

Figure 6.1 is a sample plot that displays an I-V curve for both the heated and non-heated emissive probe at a 250V discharge voltage, 0.85mg/s flow rate to the anode, a 3.2×10^{-5} Torr background pressure, and a $50°$ angular position. For the emissive probe, a 2A heating current was supplied for electron emission.

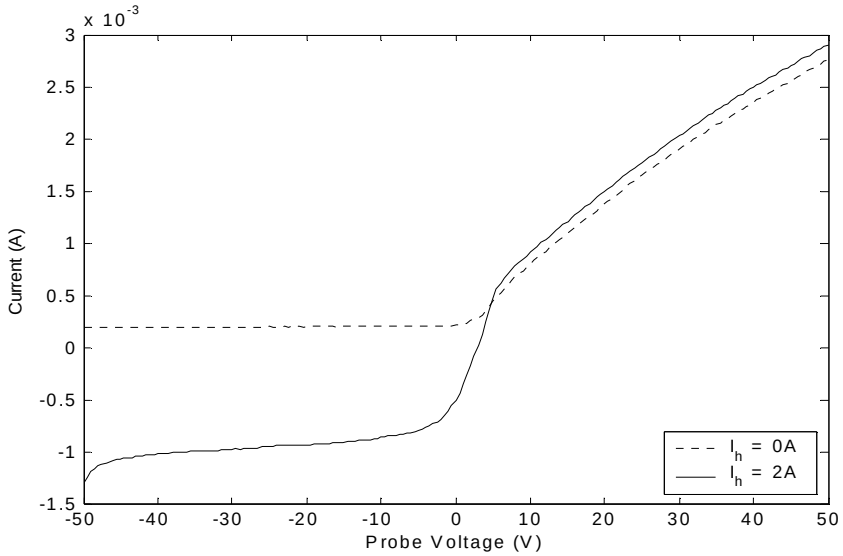

Figure 6.1 Sample I-V characteristic curve for hot and cold emissive probe. Knee is easily visible in the I-V curve of the hot probe. V_D = 250V, $\dot{m}$ = 0.85 mg/s, P = 3.2x10^{-5} Torr, angular position = 50°, and sweep radius = 25cm.

As can be seen from Figure 6.1, the knee in the I-V characteristic curve is more distinct for the heated emissive probe. As explained earlier, when the probe is heated, electrons are emitted, which leads to a distinct drop in current at the plasma potential. The knee is not easily visible in the cold probe I-V characteristic curve due to the absence of emitted current.

Several current-voltage scans were performed at each angular position to ensure measurement reproducibility. The probe was swept clockwise across the plume from $-90°$ to $90°$ in $20°$ increments. At each angular position, five current voltage scans were performed consecutively. The probe was then swept counterclockwise across the plume from $90°$ to $-90°$ in $20°$ increments and five current-voltage scans were performed consecutively at

each angular position. Thus a total of ten measurements for each angular position were averaged to produce Figure 6.1. The standard deviation about the average value for these measurements was less than 2%, indicating good reproducibility.

6.3 Plasma Potential Distribution

Plasma potential measurements were deduced from the I-V characteristic curve of the emissive probe using the inflection point method. Figure 6.2 displays the plasma potential distribution for a 250V discharge voltage, 0.8A discharge current, 0.85 mg/s flow rate to the anode, and 3.2×10^{-5} Torr background pressure.

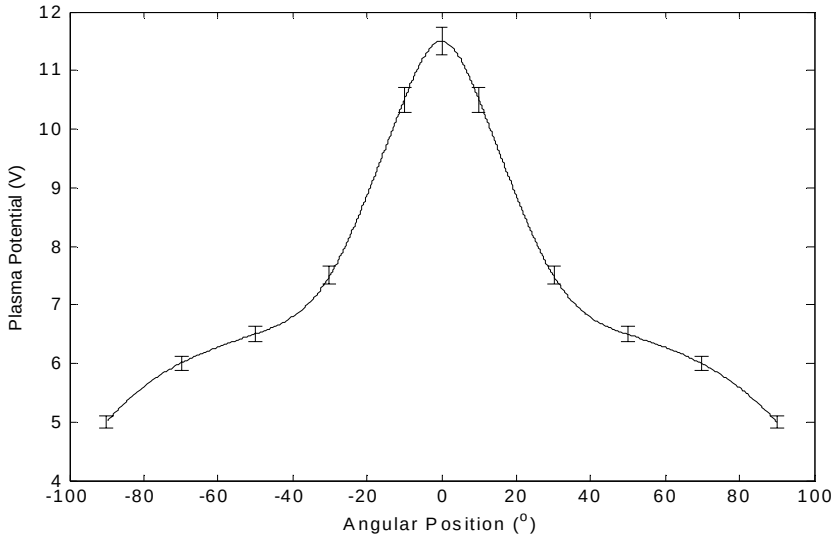

Figure 6.2 Plasma potential distribution for the BHT-200 Hall thruster plume. V_D = 250V, I_D = 0.8A, P = $3.2x10^{-5}$ Torr, and sweep radius = 25cm.

The plasma potential distribution is symmetric about the centerline with its maximum at the centerline and its minimum at the wings. The potential drop between the centerline and the wings is approximately 7V. Shoulders are present at the wings, similar to the current density distribution of Figure 4.1. These shoulders are explained by charge exchange collisions as stated previously. Plasma potential is a more direct indicator of plasma den-

sity than current flux, and thus Figure 6.2 directly displays the additional plasma wings due to charge exchange ions.

6.3.1 Effect of Discharge Voltage

The thruster's effects on plasma potential were investigated by taking measurements at 200V, 250V, and 300V discharge voltages. The background pressure was 3.2×10^{-5} Torr and the flow rate to the anode was 0.85mg/s for all cases.

Figure 6.3 portrays the effect of discharge voltage on the plasma potential distribution. As the discharge voltage increases, the plasma potential increases. Increasing the discharge voltage provides ions in the discharge chamber with a higher start potential, which leads to a higher end potential. However, this increase in plasma potential is less than proportional to the increase in discharge voltage.

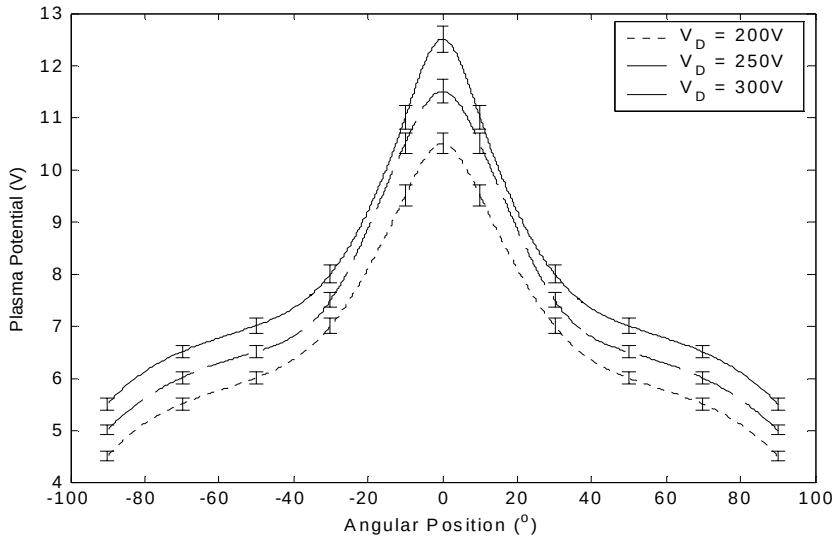

Figure 6.3 Effect of discharge voltage on the plasma potential distribution. P = $3.2\text{x}10^{-5}$ Torr, $\dot{m}$ = 0.85 mg/s, and sweep radius = 25cm.

6.3.2 Effect of Sweep Radius

Plasma potential measurements were taken at radii of 25 and 47cm. Figure 6.4 displays the effects of sweep radius on current density at a 250V discharge voltage, 0.8A discharge current, 0.85 mg/s flow rate to the anode, and a 3.2×10^{-5} Torr background pressure.

As can be seen from Figure 6.4, the plasma potential decreases with an increase in sweep radius due to similar reasons as those explained in Section 4.2.4. The plasma potential distributions for both radii have the same characteristics, a peak at the centerline and shoulders at the wings. The potential drop from the centerline to the wings is approximately 7V and 4V for a 25 and 47 cm sweep radius respectively. The decrease in plasma potential with an increase in sweep radius is not proportional.

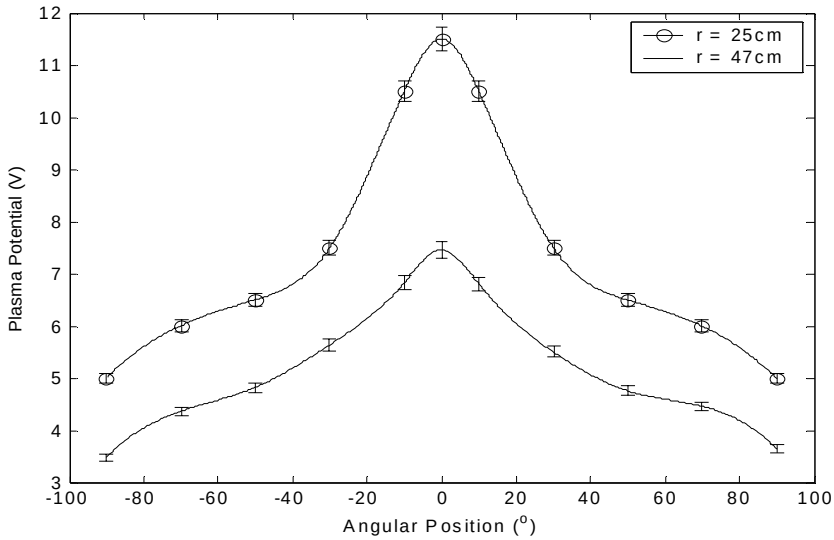

Figure 6.4 Effect of sweep radius on the plasma potential distribution. V_D = 250V, $\dot{m}$ = 0.85 mg/s, and P = $3.2x10^{-5}$ Torr.

6.3.3 Comparison to Simulation Results

Figure 6.5 shows a comparison of the plasma potential distribution for experimental and computational results. The computational results are produced from the simulation

described in Section 4.4. The data in the figure represent measurements taken at a 300V discharge voltage and a 3.2×10^{-5} Torr background pressure. As can be seen from the figure, there is relatively good agreement between the simulation and experimental results. In particular, the simulation potential drop from the centerline to the wings is approximately 7V, which is consistent with the experimental measurements [16].

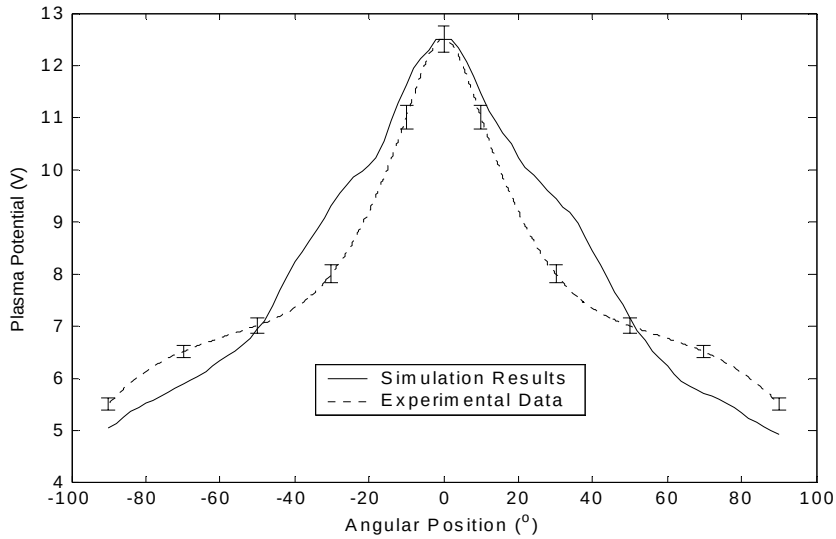

Figure 6.5 Comparison of simulation and experimental results. V_D = 300V, P = $3.2x10^{-5}$ Torr, and sweep radius = 25cm.

6.4 Electron Temperature Distribution

Electron temperature measurements were deduced from the I-V characteristic curves of the cold probe. Using equation (2.1), electron temperature was calculated from the slope of the I-V characteristic curve in the region between floating and plasma potential. Figure 6.6 displays the electron temperature distribution at a 250V discharge voltage and a 3.2×10^{-5} Torr background pressure. The electron temperature varies substantially across the plume, ranging from 2.8eV at the centerline to 1.2eV at the wings.

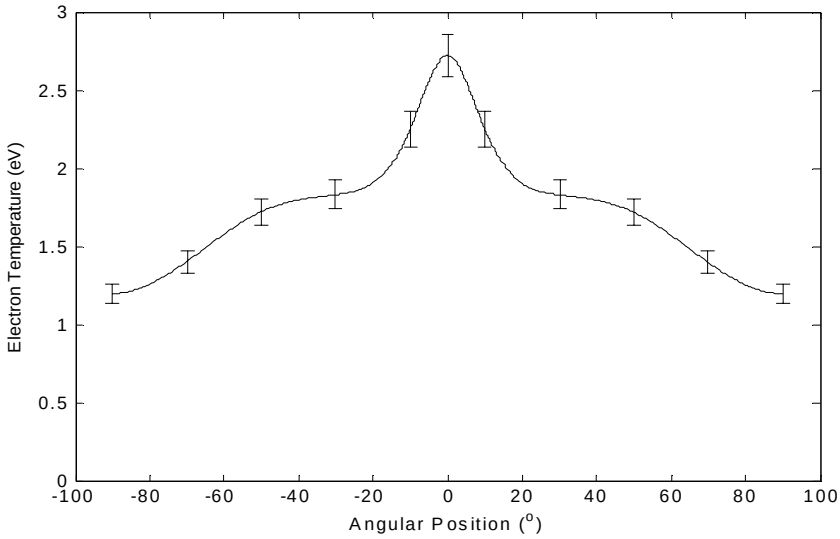

Figure 6.6 Electron temperature distribution for the BHT-200 Hall thruster plume. V_D = 250V, I_D = 0.8A, P = $3.2x10^{-5}$ Torr, and sweep radius = 25cm.

6.5 Electron Density Distribution

Electron density measurements were also deduced from the I-V characteristic curves of the cold probe using equation (2.2). Figure 6.7 portrays the electron density distribution at a 250V discharge voltage and a 3.2×10^{-5} Torr background pressure. The electron density falls from 2×10^{16} m^{-3} at the centerline to 1.3×10^{15} m^{-3} at the wings. Shoulders are present at the wings of the electron density distribution, which indicates accumulation of charge exchange ions.

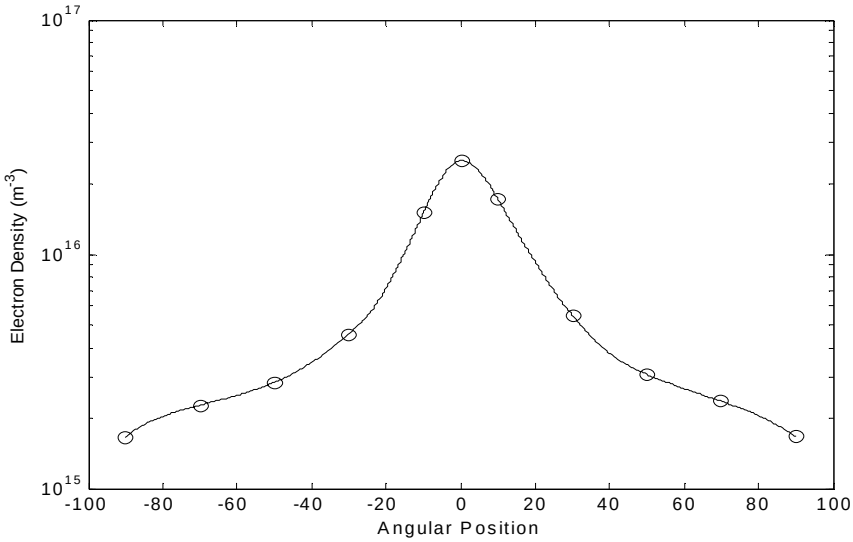

Figure 6.7 Electron density distribution for the BHT-200 Hall thruster plume. V_D = 250V, I_D = 0.8A, P = 3.2x10^{-5} Torr, and sweep radius = 25cm.

Using the electron temperature and density distribution, a relationship can be formulated by assuming the electrons behave like an ideal gas. Therefore the electron temperature and density can be related such that

$$\frac{T_e}{T_{e_c}} = \left(\frac{n_e}{n_{e_c}}\right)^{\gamma-1} \tag{6.1}$$

where T_{e_c} and n_{e_c} are electron temperature and density respectively at the centerline. This electron temperature variation roughly follows a polytropic law. γ is determined by taking the natural logarithm of both sides

$$\gamma = 1 + \frac{\ln(T_e/T_{e_c})}{\ln(n_e/n_{e_c})} \tag{6.2}$$

Plugging the values of electron temperature and electron density into equation (6.2), γ is obtained. γ is found to be approximately 1.3, which falls roughly half-way between an adiabatic expansion $\left(\gamma = \frac{5}{3}\right)$ and an isothermal, heat conduction limit $(\gamma = 1)$.

Chapter 7

ANALYSIS

7.1 Overview

The BHT-200 plume was mapped using a Faraday and emissive probe to measure current density, plasma potential, electron temperature, and electron density. This chapter will describe a consistency analysis between hot and cold emissive probe data. Specifically, plasma potential will be deduced from cold probe electron temperature and density measurements. This deduced plasma potential will be compared to the measured plasma potential from the emissive probe. A similar analysis, which consists of determining plasma potential from Faraday probe current density measurements, will be used to perform a consistency analysis between Faraday and hot emissive probe data. Finally, the experimental data were compared to solutions of a self-similar plume model.

7.2 Consistency Analysis between Hot and Cold Emissive Probe Data

In order to extract the plasma potential distribution from the cold probe electron temperature and density measurements, a modified form of the common Boltzmann relation was used. Neglecting collision and magnetic effects, the electron momentum balance is

$$\nabla(n_e k T_e) = e n_e \nabla\phi \tag{7.1}$$

Using the polytropic relationship between electron temperature and density defined by equation (6.1), the potential, ϕ, is then determined by

$$\phi = \phi_c - \frac{\gamma}{\gamma - 1}\frac{kT_{e_c}}{e}\left(1 - \left(\frac{n_e}{n_{e_c}}\right)^{\gamma - 1}\right) \tag{7.2}$$

where ϕ_c, T_{e_c}, and n_{e_c} are plasma potential, electron temperature, and electron density respectively at the beam centerline, which is used as a reference state. The electron density distribution, shown in Figure 6.7, was substituted into equation (7.2) to yield a plasma potential distribution. This distribution was compared to the measured plasma potential from the hot emissive probe. Figure 7.1 portrays a comparison of the measured and calculated plasma potential at a 250V discharge voltage, a 3.2×10^{-5} Torr background pressure, and $\gamma = 1.3$, which was determined in Section 6.5.

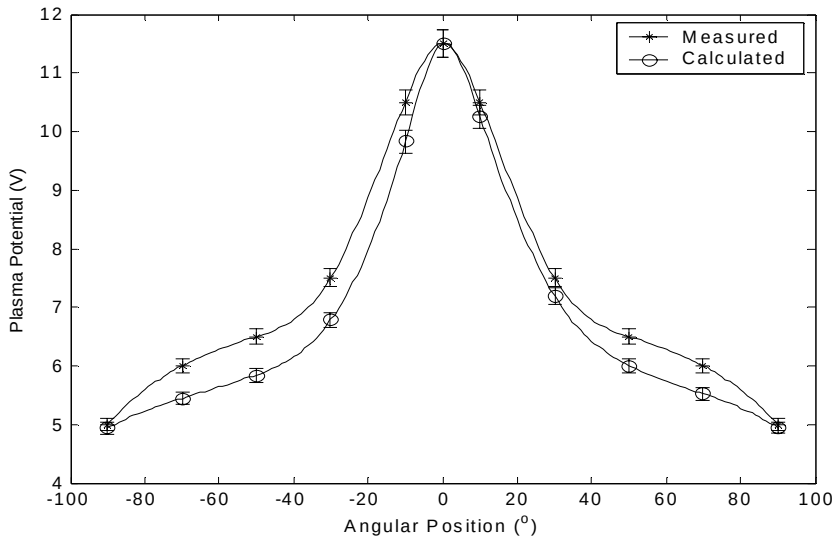

Figure 7.1 Comparison between the measured plasma potential from the hot emissive probe and the calculated plasma potential from measurements of the cold emissive probe. V_D = 250V, sweep radius = 25cm, and γ = 1.3.

Figure 7.1 shows a relatively good agreement between measured and calculated plasma potential, which demonstrates consistency between cold and emissive probe measure-

ments. This agreement also indicates that the assumption of a polytropic relationship between electron temperature and density is reasonable.

7.3 Consistency Analysis between Faraday and Emissive Probe Data

Using Faraday probe current density measurements, electron density was calculated by

$$n_e = \frac{j}{ev_i} \tag{7.3}$$

where j is current density and v_i is the speed of ions. This speed is estimated using the energy equation, in the form

$$\frac{1}{2}m_i v_i^2 = e(V_D - \phi_p) \tag{7.4}$$

where V_D is the discharge voltage and ϕ_p is the local plasma potential.

Using the electron density from equation (7.3) and the polytropic relationship in equation (6.1), the calculated electron density was substituted into equation (7.2) to obtain the plasma potential. This calculated plasma potential from Faraday probe measurements was compared to the measured emissive probe plasma potential, as shown in Figure 7.2.

Figure 7.2 shows poor agreement between the measured and the calculated plasma potential, especially at the wings. This poor agreement is due to the fact that this analysis neglects collisional effects, which are dominant at the wings. For example, equation (7.4) does not apply to charge exchange ions, which obtain their velocities from the much smaller potential differences across the plume. These charge exchange ions have a small speed corresponding to a v_i of roughly 2000 m/s [3]. In addition to charge exchange ions, elastic collisions also explain the difference between measured and calculated plasma potential at the mid-angle region.

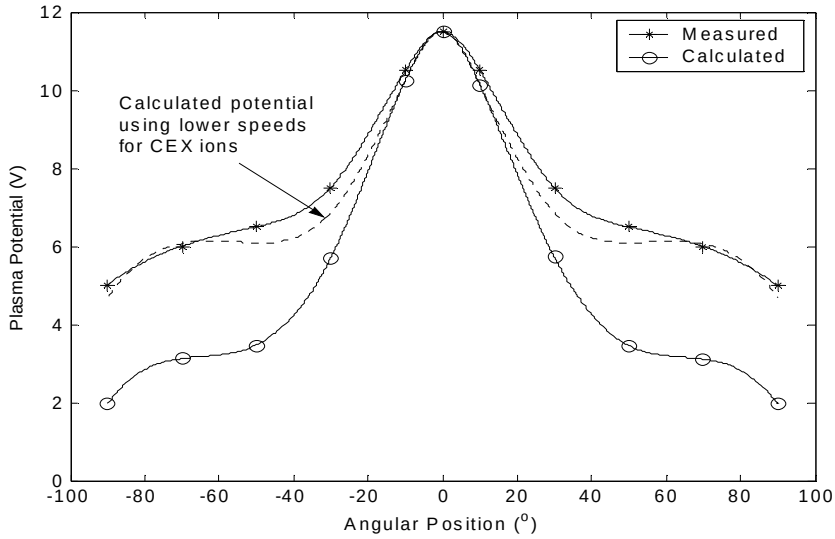

Figure 7.2 Comparison between the measured plasma potential from the hot emissive probe and the calculated plasma potential from measurements of the Faraday probe. V_D = 250V, sweep radius = 25cm, and γ = 1.3. The dotted curve is a qualitative approximation for the calculated potential using a low speed, roughly 2000 m/s, in the CEX region.

The analysis described earlier in this section was performed to determine an angular distribution of the plasma potential. However, this analysis can also be applied to determine the plasma potential drop between different axial positions, except in charge exchange dominated regions. To accomplish this, equations (7.3) and (7.4) are used to calculate electron density at various axial positions such that

$$\frac{n_e}{n_e^*} = \frac{j}{j^*}\sqrt{\frac{V_D - \phi_p^*}{V_D - \phi_p}} \tag{7.5}$$

where * indicates a reference state, which can be located anywhere in the plume. Substituting equation (7.5) into equation (7.2), a relationship between plasma potential at different axial positions is defined by

$$\phi^* - \phi = \frac{\gamma}{\gamma - 1}\frac{kT_e^*}{e}\left(1 - \left(\frac{j}{j^*}\sqrt{\frac{V_D - \phi_p^*}{V_D - \phi_p}}\right)^{\gamma - 1}\right) \tag{7.6}$$

Current density measurements were taken at sweep radii of 25 and 47cm. These measurements were then substituted into equation (7.6) to determine the potential drop for varying angular positions, using the 25 cm data as the reference state. Since plasma potential measurements were also taken at sweep radii of 25 and 47cm, results from equation (7.6) were compared to the measured potential drop between radii of 25 and 47 cm for varying angular positions. Figure 7.3 portrays a comparison of the measured and calculated potential drop at a 250V discharge voltage and a 3.2×10^{-5} Torr background pressure.

Figure 7.3 shows moderate agreement in the mid-angle region between the measured and calculated plasma potential drop. This analysis was not applied to the wings because it neglects collisional effects.

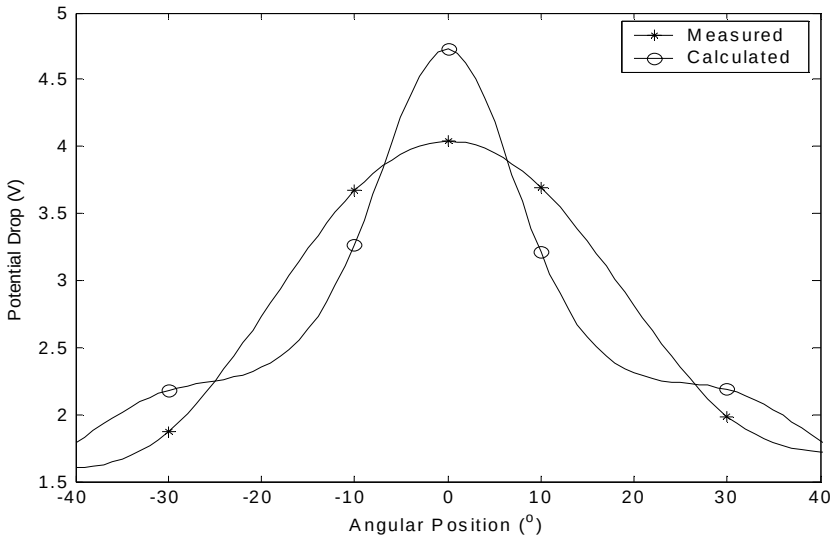

Figure 7.3 Comparison between the measured potential drop between radii of 25cm and 47cm from the hot emissive probe and the calculated potential drop from measurements of the Faraday probe. V_D = 250V, sweep radius = 25cm, and γ = 1.3.

7.4 Comparison of Experimental Data with Self-Similar Plume Model Solutions

Experimental measurements from both the Faraday and emissive probes were compared to self-similar solutions developed by A. Korsun and E. Tverdokhlebova [11] and red-erived by M. Martinez-Sanchez. The self-similar model does not assume collision effects and therefore can only be applied to the mid-angle region. A detailed derivation of the self-similar solutions is described in Appendix C.

7.4.1 Comparison with Faraday Probe Data

The self-similar solution of current density is given by

$$j = \frac{j_c}{\cos^3\theta\left(1 + \frac{\tan^2\theta}{\tan^2\theta_{1/2}}\right)^{1+\gamma/2}} \tag{7.7}$$

where $\theta_{1/2}$ is the angle corresponding to half the plasma density value at the centerline. To compare this self-similar solution to the measured current density, $\left(\frac{j_c}{j\cos^3\theta}\right)^{2/(2+\gamma)}$ was plotted against $\tan^2\theta$ as shown in Figure 7.4, where j is the measured current density distribution and j_c is the measured current density at the centerline. A linear relationship would indicate a good agreement between the self-similar model and the measured current density.

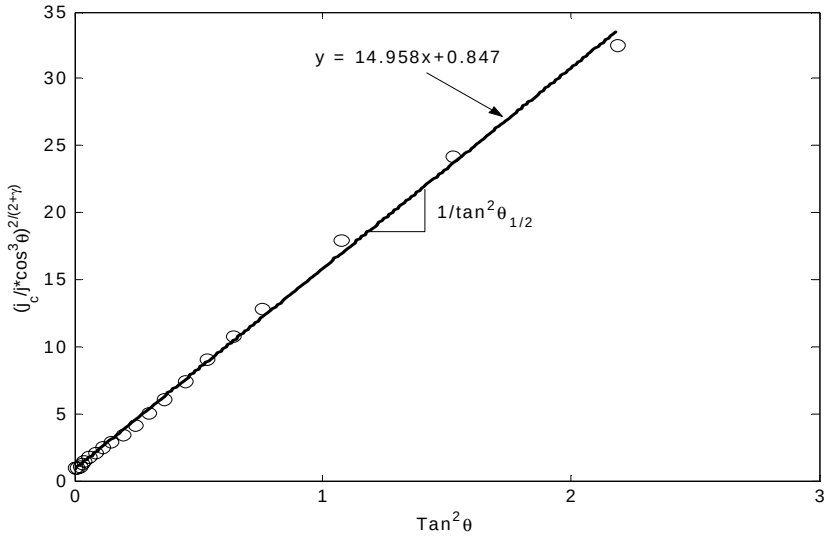

Figure 7.4 Comparison between the measured current density from the Faraday probe and the calculated current density from the solutions of the self-similar model. V_D = 250V, sweep radius = 25cm, and γ = 1.3.

Figure 7.4 shows a linear relationship between the plotted parameters at a discharge voltage of 250V for θ values ranging from the centerline to $60°$. This indicates good agreement. The slope in Figure 7.4 is $\frac{1}{\tan^2\theta_{1/2}}$, which corresponds to $\theta_{1/2} = 14.5°$.

The self-similar model also predicts a solution for the value of current density at the centerline and is given by

$$j_c = \frac{\gamma}{2\pi R^2}\frac{I_b}{\tan^2\theta_{1/2}} \tag{7.8}$$

Substituting $\gamma = 1.3$, $\theta_{1/2} = 14.5°$, $R = 25cm$, and $I_b = 0.666A$ into equation (7.8), the self-similar predicted value of current density at the centerline is 3.30 mA/cm^2. The measured current density at the centerline for the same thruster operating conditions is 2.62 mA/cm^2, indicating reasonable agreement with the self-similar plume model solution, and confirming the reliability of current density measurements.

7.4.2 Comparison with Emissive Probe Data

The self-similar solution to electron density is given by

$$n_e = \frac{n_{e_c}}{1 + \frac{\tan^2\theta}{\tan^2\theta_{1/2}}} \tag{7.9}$$

where $\theta_{1/2}$ is the angle obtained in Section 7.4.1. Substituting the measured electron density at the centerline in equation (7.9), the self-similar solution of electron density was calculated and compared to the cold emissive probe electron density, as shown in Figure 7.5.

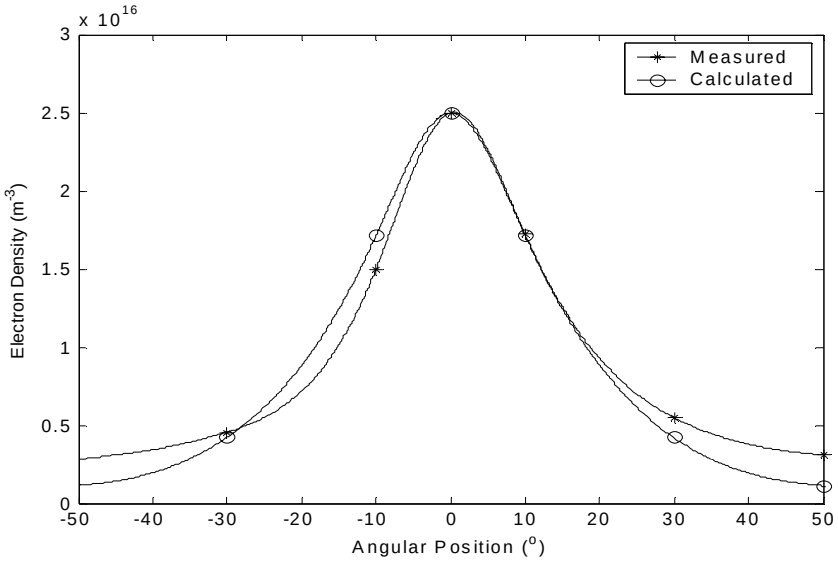

Figure 7.5 Comparison between the measured electron density from the cold emissive probe and the calculated electron density from the solutions of the self-similar model. V_D = 250V and sweep radius = 25cm.

Figure 7.5 shows good agreement between the self-similar and measured electron density. The self-similar model also predicts a solution to the electron density at the centerline and is given by

$$n_{e_c} = \frac{j_c}{e v_{i_c}} \tag{7.10}$$

where j_c is the self-similar predicted value of current density at the centerline defined by equation (7.8) and v_{i_c} is the speed of ions at the centerline defined by equation (7.4). For a discharge voltage of 250V, the self-similar value of electron density is 1.1×10^{16} m^{-3}. This predicted value is two times smaller than the cold emissive probe electron density. This disparity leads to the conclusion that electron density measurements from the cold probe are questionable, possibly due to the imperfect knowledge of the effective collecting area in a fast cross-flow.

7.4.3 Discussion

Since Faraday probe measurements are consistent with the self-similar solutions, an alternative way to measure electron density is to acquire current density at the centerline with a Faraday probe, and use equations (7.9) and (7.10) to deduce the electron density, shown in Figure 7.6.

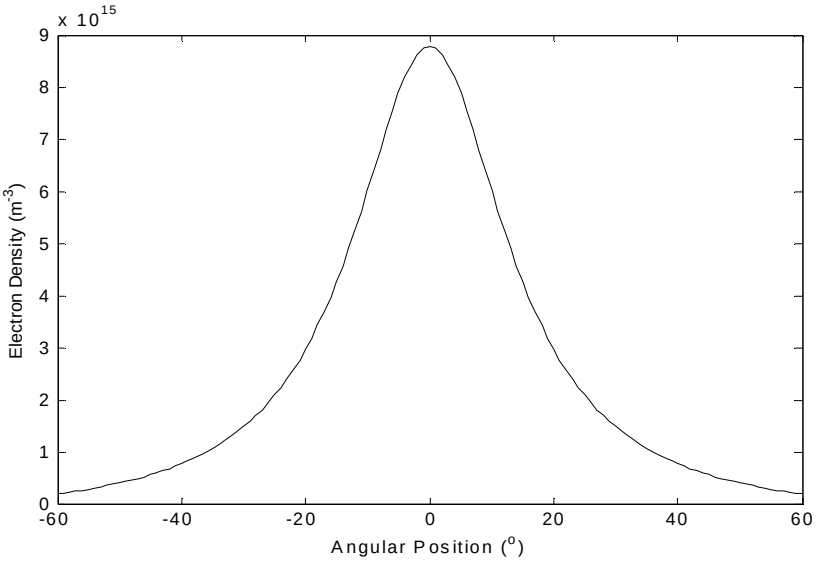

Figure 7.6 Electron density calculated using Faraday probe current density measurements at the center-line combined with the solutions of the self-similar model. V_D = 250V and sweep radius = 25cm.

From this electron density distribution, analyses similar to those explained in Section 7.2 can be performed to determine electron temperature and plasma potential. This plasma potential is compared to hot emissive probe plasma potential, as shown in Figure 7.7.

From Figure 7.7, relatively good data agreement is obtained. The good agreement between the self-similar and hot emissive probe plasma potential is a further indication that using a Faraday probe is reliable to determine electron density, electron temperature, and plasma potential. However, this agreement is only valid in regions where collisions do not dominate. At the wings where charge exchange collision products dominate, poor data agreement exists because the self-similar model does not account for collisional effects.

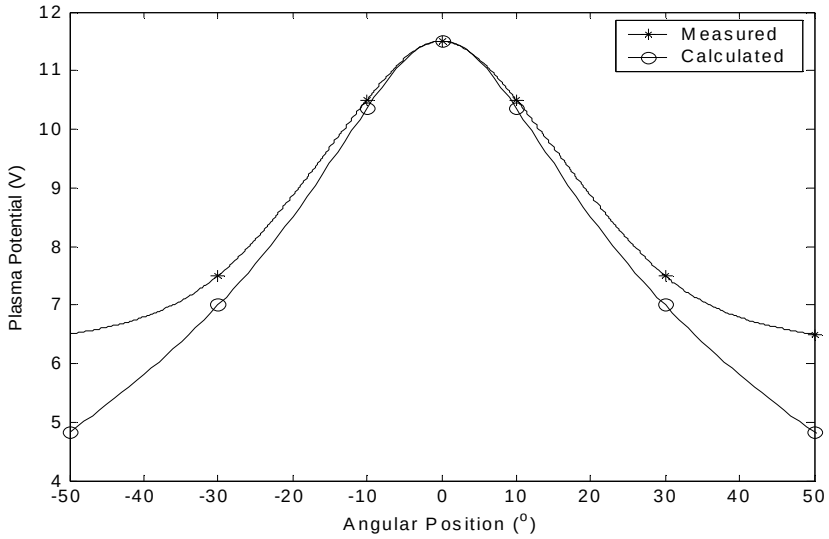

Figure 7.7 Comparison between the measured plasma potential from the hot emissive probe and the calculated plasma potential using the electron density distribution in Figure 7.6. V_D = 250V and sweep radius = 25cm

Chapter 8

CONCLUSION

To support ongoing computational models, plume diagnostic instruments were developed and used to characterize the BHT-200 Hall thruster plume. Plasma measurements consisted of studying facility and thruster effects on the plume. Facility effects included background pressure and sweep radius, while thruster effects included discharge voltage and flow rate. Miniature probes were shown to produce similar results to larger probes. The data repeatability was within 5%, which met the objectives of the research. Experimental results showed that current density is more sensitive to background pressure than to thruster effects, plasma potential is a more direct indicator of plasma density than current flux, and electron temperature and electron density vary substantially across the plume following a polytropic relationship.

Data analyses were performed using a consistency analysis of the experimental data by deducing plasma potential from Faraday and cold emissive probe data and comparing it to the measured plasma potential from the hot emissive probe. In addition, these experimental results were compared to solutions of a self-similar plume model. These analyses have shown that measurements of the Faraday probe current density and the hot emissive probe plasma potential are reliable, whereas measurements of cold emissive probe electron density are questionable. Furthermore, Faraday probe data were shown to yield good predictions of electron density when combined with the solutions of the self-similar model. In

conclusion, the experimental data shown in this research provide a valuable database of measurements that can be used to validate computational results.

REFERENCES

[1] Boyd, I. D., and R. Dressler. "Far Field modeling of the Plasma Plume of a Hall Thruster." *Journal of Applied Physics*, 92(4):1764-1774, August 2002.

[2] Brown, C. O., and E. Pinsley. "Further Experimental Investigations of a Cesium Hall-Current Accelerator." *AIAA Journal*, 3(5), May 1965.

[3] Cheng, S. Y., Computational Modeling of a Hall Thruster Plasma Plume in a Vacuum Tank, S.M. Thesis, Massachusetts Institute of Technology, February 2002.Fife, J. M., Hybrid-PIC Modeling and Electrostatic Probe Survey of Hall Thrusters, Ph.D. Thesis, Massachusetts Institute of Technology, September 1998.

[4] Fife, J. M., Hybrid-PIC Modeling and Electrostatic Probe Survey of Hall Thrusters, Ph.D. Thesis, Massachusetts Institute of Technology, September 1998.

[5] Haas, J. M., Low-perturbation Interrogation of the Internal and Near-field Plasma Structure of a Hall Thruster Using a High-Speed Probe Positioning System, Ph.D. Thesis, University of Michigan, 2001.

[6] Hruby, V., J. Monheiser, B. Pote, P. Rostler, J. Kolencik, and C. Freeman, "Development of Low Power Hall Thrusters," 30th Plasmadynamics and Lasers Conference, Norfolk, VA, July 1999.

[7] Hutchinson, I. H., *Principles of Plasma Diagnostics*, Cambridge University Press, Cambridge, 1987.

[8] Janes, G. S., and R. Lowder. "Anomalous Electron Diffusion and Ion Acceleration in a Low-Density Plasma." *Physics of Fluids*, 9. P.1115, 1966.

[9] Kemp, R. F., and J. Sellen. "Plasma Potential Measurements by Electron Emissive Probes." *The Review of Scientific Instruments*, 37(4):455-461, April 1966.

[10] Kim, V., "Plasma Parameter Distribution Determination in SPT-70 Plume," 28th International Electric Propulsion Conference, Toulouse, France, March 2003.

[11] Korsun, A. G., and E. Tverdokhlebova, "The Characteristics of the EP Exhaust Plume in Space," 33rd AIAA/ASME/SAE/ASEE Joint Propulsion Conference and Exhibit, Seattle, WA, July 1997.

[12] Morozov, A. I., Yu. Esipchuk, and A. Kapulkin. "Azimuthally Asymmetric Modes and Anomalous Conductivity in Closed Electron Drift Accelerators." *Soviet Physics Technical Physics*, 18, P.615, 1973.

[13] Oh, D. Y., Computational Modeling of Expanding Plasma Plumes in Space Using a PIC-DSMC Algorithm, Sc.D. Thesis, Massachusetts Institute of Technology, February 1997.

[14] Pacros, A., Instruments Design and Testing for a Hall Thruster Plume Experiment on the Space Shuttle, S.M. Thesis, Massachusetts Institute of Technology, June 2002.

[15] Pollard, J. E., K. Diamant, V. Khayms, L. Werthman, D. King, and K. de Grys, "Ion Flux, Energy, and Charge-State Measurements for the BPT-4000 Hall Thruster," 37th AIAA/ASME/SAE/ASEE Joint Propulsion Conference and Exhibit, Salt Lake City, Utah, July 2001.

[16] Santi, M. M., Hall Thruster Plume Simulation Using a Hybrid-PIC Algorithm, S.M. Thesis, Massachusetts Institute of Technology, September 2003.

[17] Smith, J. R., N. Hershkowitz, and P. Coakley. "Inflection-Point Method of Interpreting Emissive Probe Characteristics." *The Review of Scientific Instruments*, 50(2):210-218, February 1979.

[18] Thomas, S., Developing a Space Shuttle Experiment for Hall and Pulsed Plasma Thrusters, S.M. Thesis, Massachusetts Institute of Technology, February 1999.

[19] Walker, M. L. R., R. Hofer, and A. Gallimore, "The Effects of Nude Faraday Probe Design and Vacuum Facility Backpressure on the Measured Ion Current Density Profile of Hall Thruster Plumes," 38th AIAA/ASME/SAE/ASEE Joint Propulsion Conference and Exhibit, Indianapolis, IN, July 2001.

Appendix A

BHT-200 THRUSTER

A.1 Overview

The low power BHT-200 thruster, which was developed by the Busek Company, was used in this research for plume characterization [6]. The BHT-200 was developed for the Air Force and is slated for flight on the TechSat 21. Its design uses a unique magnetic circuit, which is able to create a high magnetic flux that is necessary in small size Hall thrusters. The magnetic circuit design consists of a single electromagnetic coil. Specifications of the thruster include a weight of approximately 900g, diameter of 100 mm, and length of 105 mm. It also has an acceleration chamber with a mid-diameter of 21 mm. An image of the BHT-200 thruster is shown in Figure A.1.

A.2 Cathode

A hollow thermionic cathode is used to provide a source of electrons to the anode. These high energy electrons collide with xenon inside the discharge cavity, creating ions that are electrostatically accelerated from the thruster. In addition, the cathode provides electrons to neutralize the exhaust plume. The discharge tube of the cathode is 3.2 mm in diameter and the emitter material has a low work function that easily ejects electrons. To operate the cathode, a flow rate of 0.08 mg/s is required. During operation, the cathode is self-sustaining and the keeper is maintained at 12V and 0.5A The cathode of the BHT-200 is portrayed in Figure A.2.

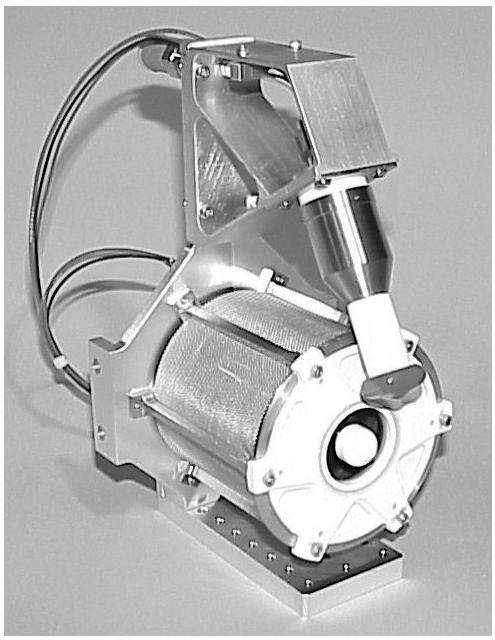

Figure A.1 The BHT-200 Hall thruster.

Figure A.2 The BHT-200 cathode.

A.3 Performance Measurements

The BHT-200 runs nominally at a discharge voltage of 250V, a discharge current of 0.8A, and a flow rate of 0.85 mg/s to the anode. It has a specific impulse of 1300s, a thrust of 12.4mN, and an efficiency of 42%. Performance measurements of the BHT-200 have been conducted and include thrust, specific impulse and efficiency.

A.3.1 Thrust

Figure A.3 shows the effect of discharge voltage on thrust at different xenon flow rates to the anode. The thrust of the BHT-200 varies from 10mN to 16mN. As can be seen in Figure A.3, the thrust increase as the flow rate of xenon is increased. In addition, increasing the discharge voltage also leads to an increase in thrust. This effect is due to the fact that more ionization occurs when either the flow rate or the discharge voltage is increased.

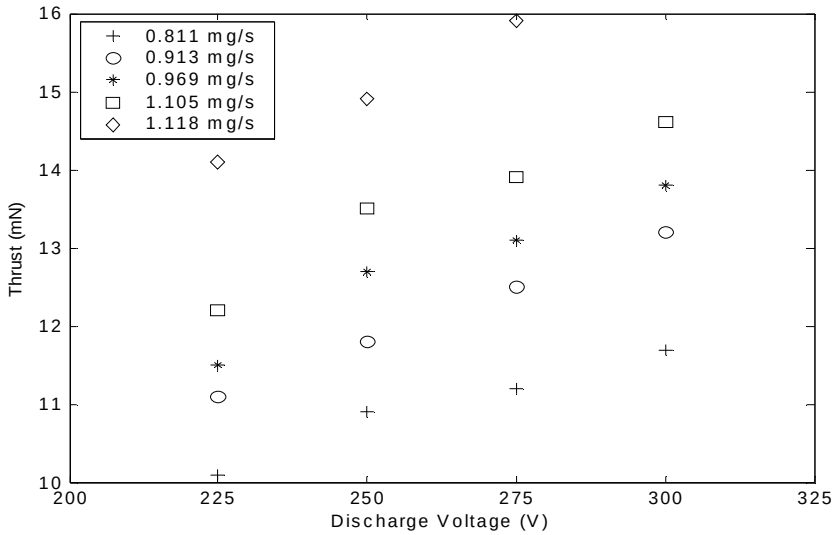

Figure A.3 Measured thrust vs. discharge voltage for the BHT-200 thruster at different xenon flow rates to the anode.

A.3.2 Specific Impulse

Figure A.4 portrays the effect of discharge voltage on specific impulse at different xenon flow rates to the anode. The specific impulse ranges from 1150s to 1350s. As the discharge voltage increases, the specific impulse increases due to higher ionization of xenon. However, the flow rate hardly affects the specific impulse. As the flow rate increases, the thrust also increases, which leads to a near cancellation effect of the flow rate on the specific impulse. Equation (A.1) relates specific impulse to thrust and flow-rate.

$$I_{sp} = \frac{T}{\dot{m}g} \tag{A.1}$$

where T is thrust and $\dot{m}$ is flow rate.

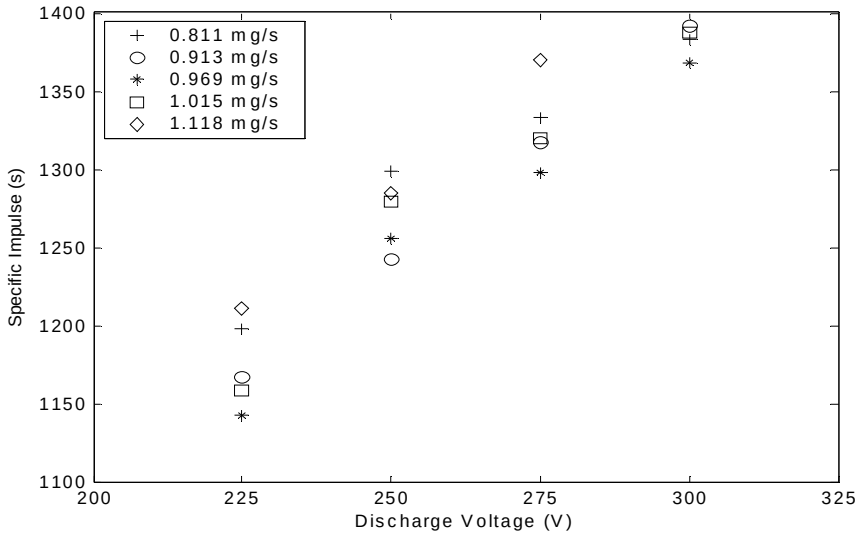

Figure A.4 Measured specific impulse vs. discharge voltage for the BHT-200 thruster at different xenon flow rates to the anode.

A.3.3 Efficiency

Figure A.5 shows the effect of discharge voltage on efficiency for different xenon flow rates to the anode. As can be seen from the figure, there is no clear trend as the discharge voltage or the flow rate is increased. The maximum efficiency is 45% at a discharge voltage of 250V and flow rate of 0.811 mg/s, which might explain the reason for choosing these parameters as the nominal operating conditions for the BHT-200. The efficiency is related to the thrust, power, and flow rate by equation (A.2).

$$\eta_t = \frac{T^2}{2\dot{m} I_D V_D} \tag{A.2}$$

where I_D and $_D$ are discharge current and discharge voltage respectively.

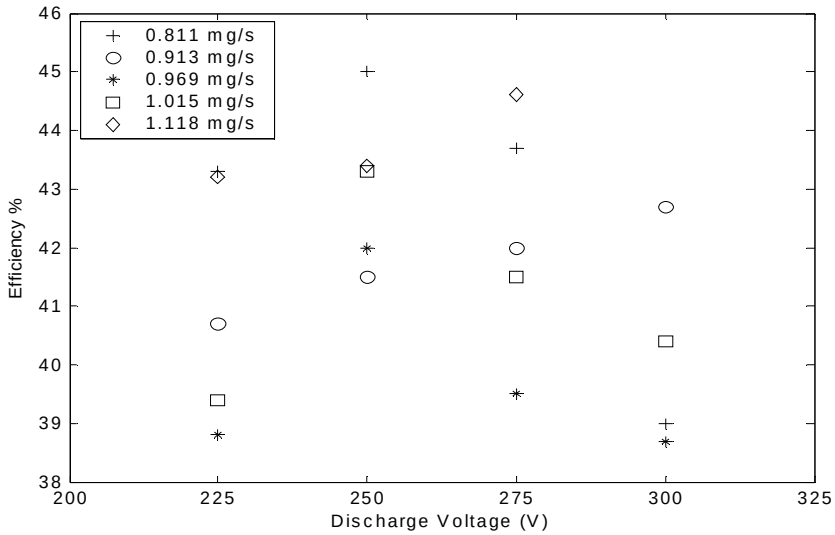

Figure A.5 Measured efficiency vs. discharge voltage for the BHT-200 thruster at different xenon flow rates to the anode.

A.4 BHT-200 Operational Procedures

A.4.1 Cathode Startup

Figure A.6 portrays the procedure necessary to start the cathode. The cathode emitter is very sensitive to moisture and oxygen. Therefore, it is important to condition the cathode in order not to damage it. Cathode conditioning first consists of flowing 0.1 mg/s of xenon through the cathode for half an hour to fill the lines connecting the xenon tank to the cathode. Then, the cathode heater is supplied with 2A of current for half an hour and then the heating current is increased by 0.5A every half an hour until the heating current reaches 6.5A. Next, the cathode keeper power supply is turned on and the voltage is increased until it switches from voltage mode to current mode. This step is very crucial as it may require being repeated several times until the power supply switches to current mode. The keeper power supply is then set to 0.5A. Finally, the cathode heater is turned off, and the cathode is in standby mode.

A.4.2 Thruster Startup

Thruster operation is begun once the cathode is on standby mode. The operation start-up procedure is outlined in Figure A.7. After following the thruster start-up procedures, it is necessary to wait at least half an hour before taking any data until the thruster reaches a thermal steady state.

A.4.3 Thruster/Cathode Shutdown

Figure A.8 outlines the process by which both the thruster and the cathode are turned off. It basically consists of reversing the start-up procedures. It should be noted that the thruster is turned off before the cathode. Furthermore, after turning off the Hall thruster, it is important to wait until the next day to open the vacuum chamber, because early opening of the chamber will result in damage of the cathode.

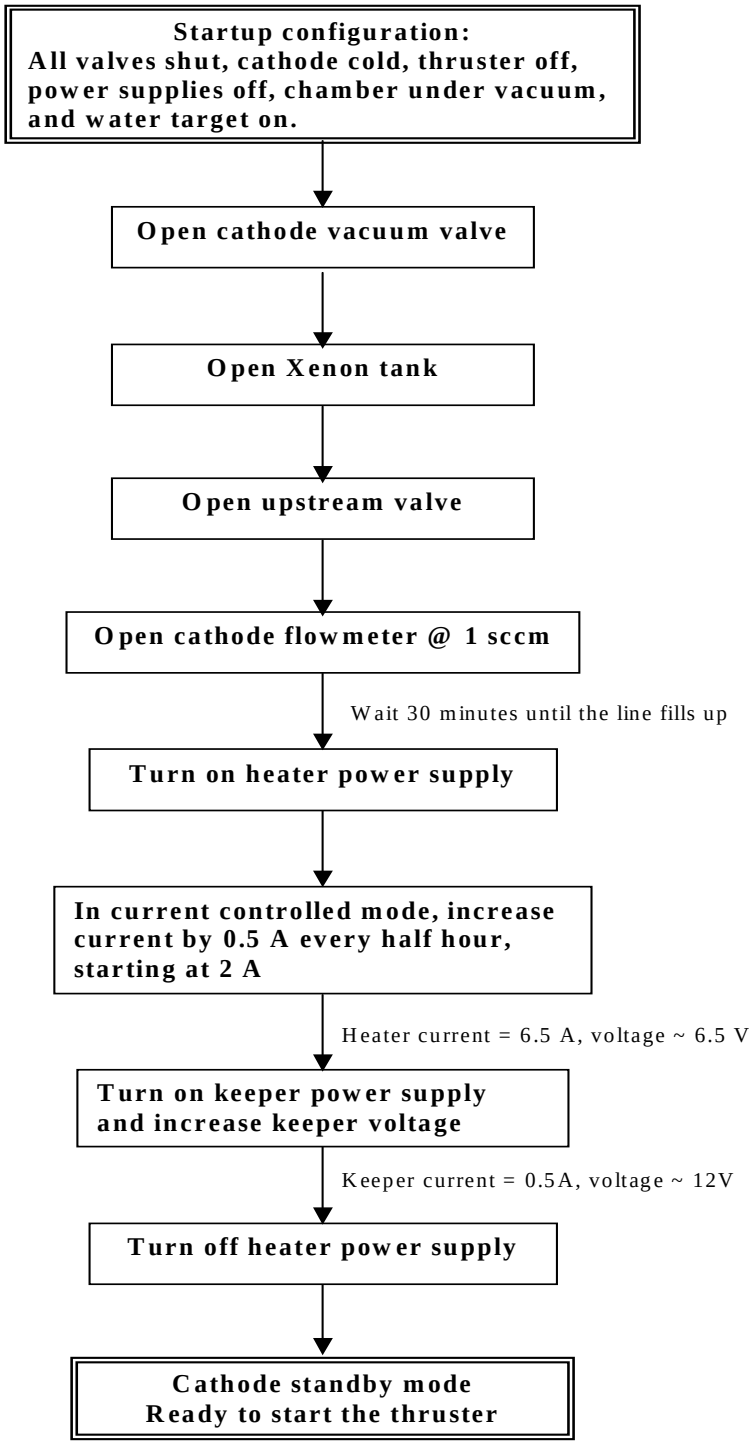

Figure A.6 Cathode startup procedures.

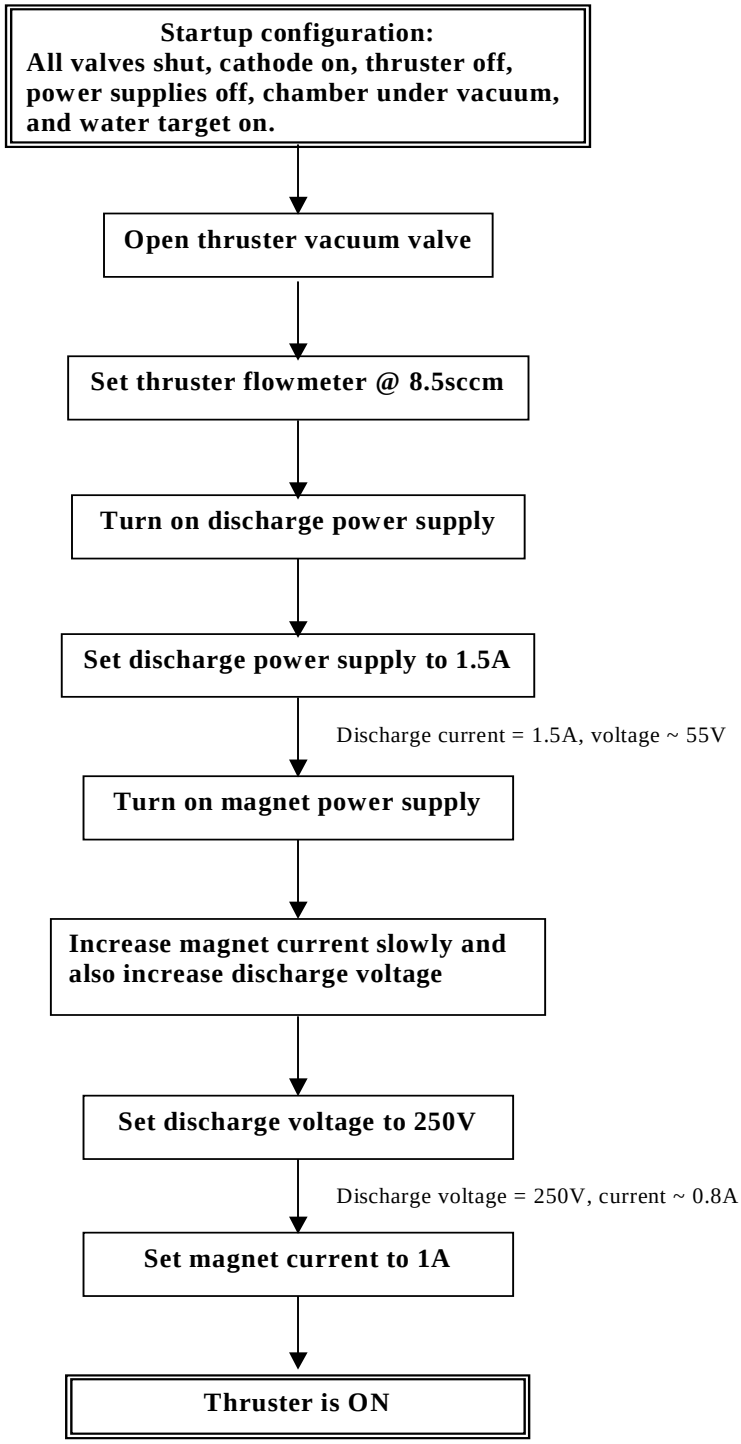

Figure A.7 Thruster startup procedures.

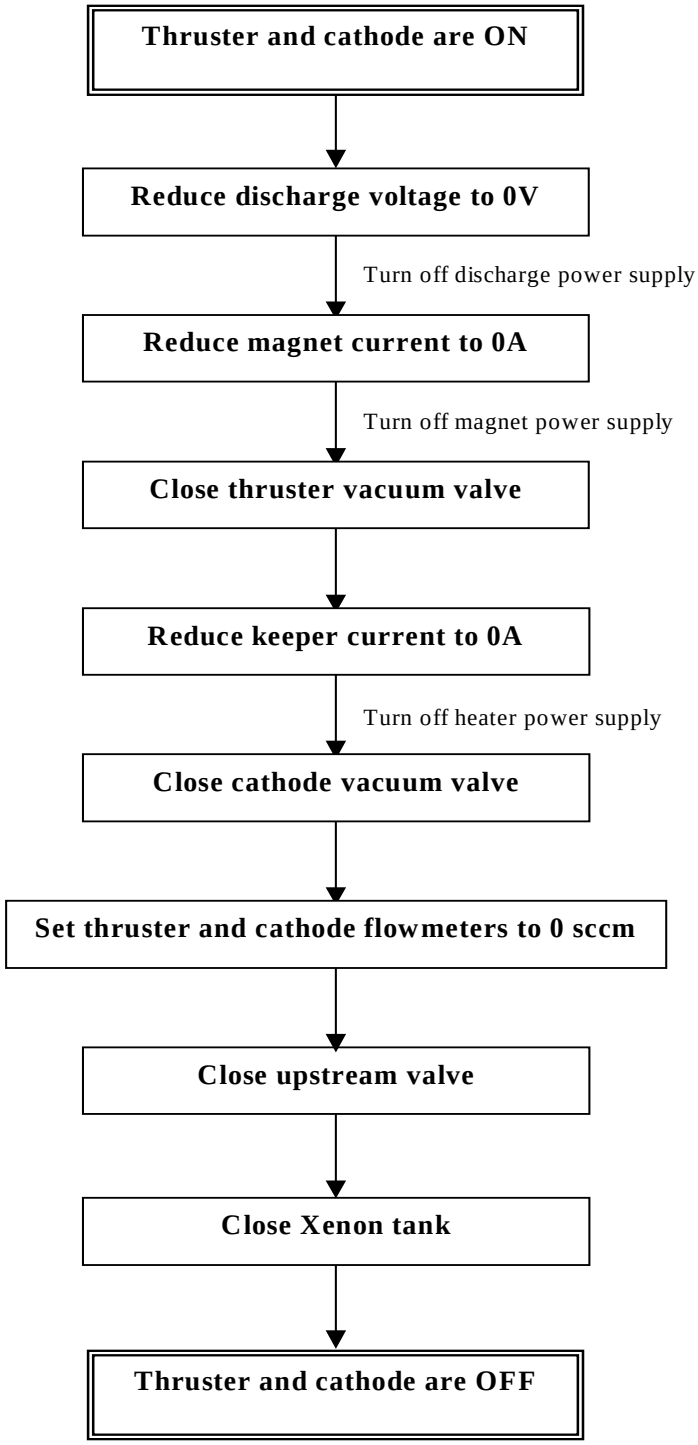

Figure A.8 Thruster and cathode shutdown procedures.

Appendix B

FLAWED FARADAY PROBE DESIGNS

B.1 Overview

This appendix presents testing results of a gridded and a nude Faraday probe, whose data were not reliable. The experimental setup and procedure for the probes are similar to the ones described in Chapter 3. The current density measurements were conducted at MIT. The thruster was operated at a discharge voltage of 300V, a xenon flow rate of 0.72 mg/s, and a background pressure of 2.9×10^{-5} Torr.

B.2 Gridded Faraday Probe

B.2.1 Description

The gridded Faraday probe is a diagnostic instrument that measures current density. The grid consists of a tungsten mesh with a 1 mm spacing. Its purpose is to repel low energy ions when it is positively biased. The gridded Faraday probe, shown in Figure B.1, consists of a 3.175 mm stainless steel collector and a 6.35 mm stainless steel guard ring.

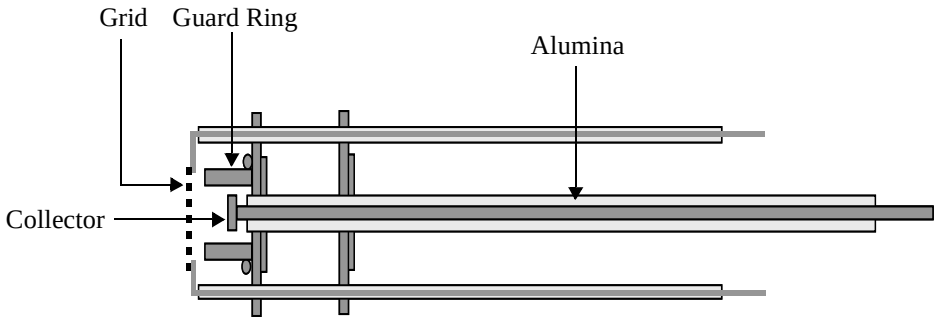

Figure B.1 Schematic of the gridded Faraday probe.

B.2.2 Results

The first experiment was conducted to study the influence of the grid bias on the current density. This investigation was achieved by comparing the current density with and without a 30V grid bias. The collector bias was −12V and the guard ring was floating, in both cases. Figure B.2 summarizes the results.

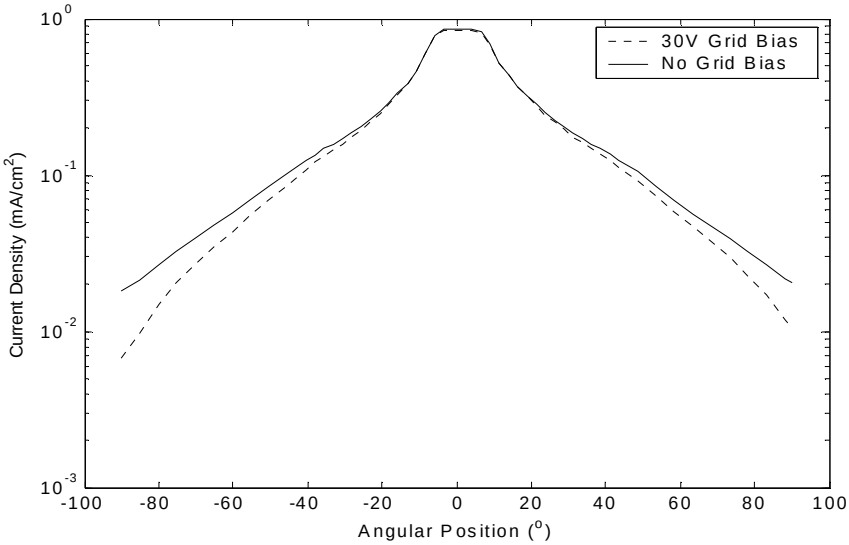

Figure B.2 Effect of grid bias on current density distribution of the gridded Faraday probe.

From Figure B.2, it can be concluded that the current density is independent of grid bias in the centerline region. At large angles, however, the probe collects less current when the grid is biased. Therefore, the effect of the grid bias is more apparent at large angles because low energy ions that are repelled by the grid bias dominate only at large angles.

Furthermore, the ratio of beam current to discharge current is around 34%. This low ratio could be a result of space charge limitation between the collector and the grid. This space charge limitation could also be the cause of the flatness of the current density distribution in the centerline region, as shown in Figure B.2.

Additional tests were conducted to study the influence of collector bias. Voltages of −12V, −20V, and −30V were applied to the collector while the grid was unbiased, and the guard ring was floating. Figure B.3 summarizes the results.

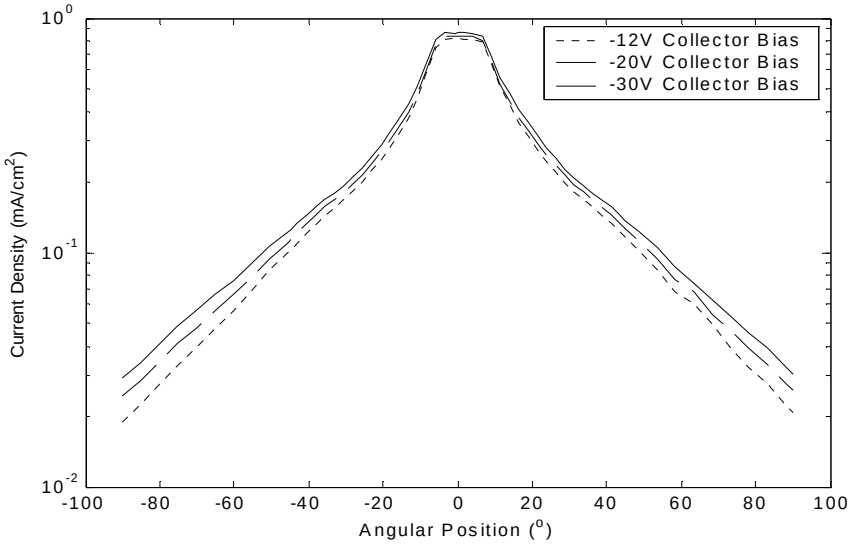

Figure B.3 Effect of collector bias on current density of the gridded Faraday probe.

As can be inferred from Figure B.3, the influence of the collector bias is similar to the influence of the grid bias. Close to the centerline, the voltage applied to the collector does not affect the collected current. At large angles, the more negative the voltage is, the more

current is collected. Also, the current density distribution at the centerline is still flat, suggesting that increasing the collector bias does not eliminate the space charge limitation.

It can be concluded that changing either the collector bias and/or the grid bias is not sufficient to achieve an appropriate ratio of beam current to discharge current. This ratio should be on the order of 67% [15]. In addition, as the collector voltage increases, the current measured, at large angles, increases by as much as a factor of 2. Because of this variation, it is uncertain which reading is correct. Therefore, the appropriate collector bias is unknown. An alternate design of the Faraday probe is necessary for two reasons. First, the saturation of the data in the centerline region must be eliminated. Secondly, the variation of the results associated with increasing the collector voltage needs to be reduced at large angles.

B.3 Nude Faraday Probe

B.3.1 Description

In an attempt to eliminate saturation of the current density distribution in the centerline region, the grid was removed from the probe, as shown in Figure B.4. This nude Faraday probe is similar to the gridded Faraday probe except for the absence of the grid. It consists of a 3.175 mm stainless steel collector and a 6.35 mm stainless steel guard ring.

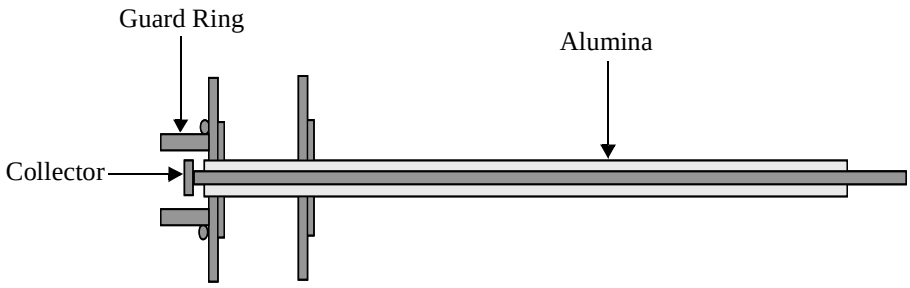

Figure B.4 Schematic of the nude Faraday probe.

B.3.2 Results

Voltages of −12V, −20V and −30V were applied to the collector. The guard ring was floating for all cases. The results shown in Figure B.5 represent the influence of collector bias on the current density using the nude Faraday probe.

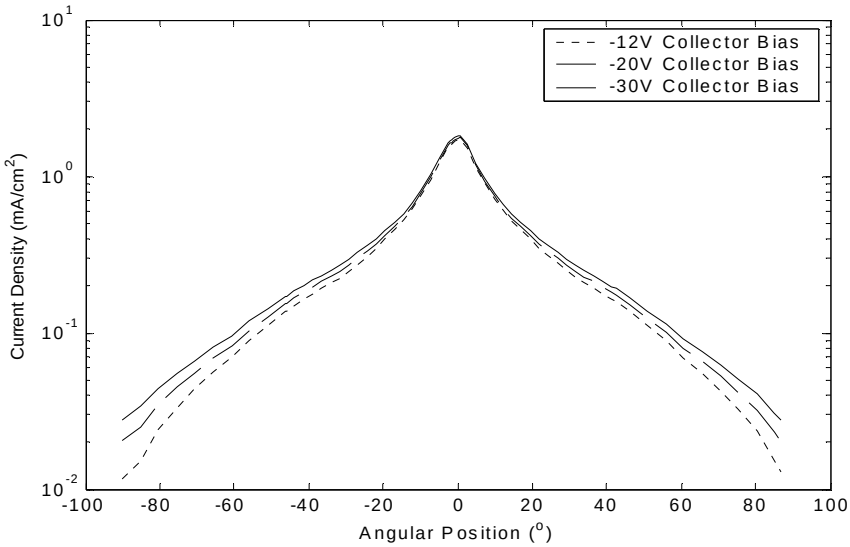

Figure B.5 Effect of collector bias on current density of the nude Faraday probe.

As shown in Figure B.5, the current density is independent of collector bias in the centerline region. In addition, the data at the centerline is not saturated, suggesting that removal of the grid eliminated the space charge limitation. The calculated beam current to the discharge current ratio is between 65% and 80%, which is in the desired range. At large angles, as the collector voltage increases in the negative direction, the current measured, at large angles, increases by as much as a factor of 2. Therefore, there still exists a large variation of the data at large angles when the collector voltage increases. It can be concluded that removing the grid is not enough to obtain accurate measurements of the current density. More design changes are necessary to achieve correct measurements.

B.4 Possible Design Flaws

The designs of both the gridded and nude Faraday probes did not meet spacing requirements, which are discussed in Chapter 3. The spacing between the collector and guard ring for both probes is 1 mm, which is larger than the 0.5 mm minimum spacing that was required to overlap the collector and guard ring sheaths. In addition, the guard ring was floating for both probes in all the measurements acquired, meaning a bumpy sheath was created around the collector, which may explain the reason current density measurements were very sensitive to changes in collector bias. These flawed Faraday probe designs were the groundwork that led to a better and more reliable design, which is discussed in Chapter 3.

Appendix C

A SELF-SIMILAR PLASMA JET INTO VACUUM

C.1 Governing Equations

Consider a jet of plasma of low density issuing at an initial Mach number (ion), $M_o = \upsilon_{ix(x=r=0)} / \sqrt{\gamma \frac{k}{m_i} T_{e(x=r=0)}}$, from a nozzle and expanding into a vacuum. The plume is characterized at x by a radius $a(x)$, as shown in Figure C.1, to be defined later more precisely.

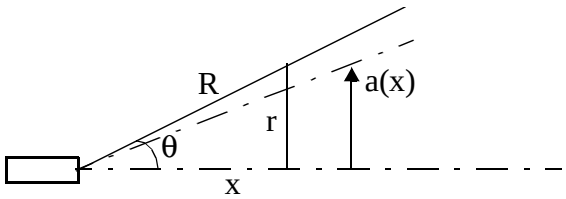

Figure C.1 Plasma jet expanding from a nozzle into vacuum

The collisionless fluid equations governing electrons and ions in the quasi-neutral region ($n_e = n_i$) are:

$$\nabla \cdot (n_e \vec{\upsilon}_i) = 0 \quad ; \quad \nabla \cdot (n_e \vec{\upsilon}_e) = 0 \tag{C.1}$$

$$\nabla (n_e k T_e) = \nabla \phi \tag{C.2}$$

$$m_i n_e(\vec{\upsilon}_i \cdot \nabla)\vec{\upsilon}_i + \nabla(n_e k T_i) = -e n_e \nabla\phi \tag{C.3}$$

$$\frac{n_e}{n_{eo}} = \left(\frac{T_e}{T_{eo}}\right)^{\frac{1}{\gamma-1}} \tag{C.4}$$

where equation (C.4) is regarded as an interpolating approximation between isentropic flow ($\gamma = 5/3$ for electrons) and isothermal flow ($\gamma = 1$). Experimental data appear to favor $\gamma \sim 1.2 - 1.3$. Since electron inertia is not included, the electron velocity, $\vec{\upsilon}_e$, appears only in equation C.1b, and that equation can be decoupled from the others.

C.2 Energy Integrals

Using equation (C.2) and (C.4), it can be shown that the potential is directly related to the electron temperature by

$$\phi = \phi_o + \frac{\gamma}{\gamma-1}\frac{k(T_e - T_{eo})}{e} \tag{C.5}$$

This can be interpreted as a statement of conservation of electron energy, composed of electrostatic energy $-e\phi$ per electron, and thermal energy $\frac{\gamma}{\gamma-1}kT_e$ per electron, where $\frac{\gamma}{\gamma-1}k$ is the specific heat per particle.

An ion energy conservation, similar to Bernoulli's equation, can also be derived. Adding equations (C.2) and (C.3), the ambipolar momentum equation is obtained:

$$m_i n_e\left[\nabla\left(\frac{\upsilon_i}{2}\right)^2 + (\nabla \times \vec{\upsilon}_i) \times \vec{\upsilon}_i\right] + \nabla[n_e k(T_e + T_i)] = 0 \tag{C.6}$$

Assuming $\frac{T_i}{T_e} \approx const$, equation (C.6) can be rewritten as

$$m_i\left[\nabla\left(\frac{\upsilon_i}{2}\right)^2 + (\nabla \times \vec{\upsilon}_i) \times \vec{\upsilon}_i\right] + \left(1 + \frac{T_i}{T_e}\right)e\nabla\phi \approx 0 \tag{C.7}$$

The projection of equation (C.7) along the ion trajectory is

$$\frac{\vec{\upsilon}_i}{\upsilon_i} \cdot \nabla \left[m_i \frac{\upsilon_i^2}{2} + \left(1 + \frac{T_i}{T_e}\right) e\phi \right] = 0 \tag{C.8}$$

which states that the sum of ion kinetic energy and a modified potential energy $\left(1 + \frac{T_i}{T_e}\right) e\phi$ per ion, remains constant along each streamline. The flow originated presumably by expansion from some uniform plenum, so we can assume that the constant is the same for all streamlines, giving,

$$m_i \left(\frac{\upsilon_i^2 - \upsilon_{io}^2}{2} \right) + \left(1 + \frac{T_i}{T_e}\right) e(\phi - \phi_o) = 0 \tag{C.9}$$

C.3 Self-Similarity Assumption for an Axi-symmetric Jet

In cylindrical coordinates, the ion continuity and momentum (ambipolar) equations are:

$$\frac{\partial}{\partial x}(e\upsilon_{ix}) + \frac{1}{r}\frac{\partial}{\partial r}(r n_e \upsilon_{ir}) = 0 \tag{C.10}$$

$$m_i \left(\upsilon_{ix}\frac{\partial \upsilon_{ix}}{\partial x} + \upsilon_{ir}\frac{\partial \upsilon_{ix}}{\partial r} \right) = -e\left(1 + \frac{T_i}{T_e}\right)\frac{\partial \phi}{\partial x} = -\left(1 + \frac{T_i}{T_e}\right) k \frac{\partial T_e}{\partial x}\frac{\gamma}{\gamma - 1} \tag{C.11}$$

$$m_i \left(\upsilon_{ix}\frac{\partial \upsilon_{ir}}{\partial x} + \upsilon_{ir}\frac{\partial \upsilon_{ir}}{\partial r} \right) = -e\left(1 + \frac{T_i}{T_e}\right)\frac{\partial \phi}{\partial r} = -\left(1 + \frac{T_i}{T_e}\right) k \frac{\partial T_e}{\partial r}\frac{\gamma}{\gamma - 1} \tag{C.12}$$

We will seek conditions under which the variables n_e, T_e, υ_{ix}, and υ_{ir} are each separable as a product of two functions, one giving the centerline value as a function of x, the other giving the radial shape as a function of $\eta \equiv r/a(x)$.

Following Korsun and Tverdoklebova [11], we attempt a decomposition of the specific form:

$$\upsilon_{ix} = u_c(x) y(\eta) \tag{C.13}$$

$$\upsilon_{ir} = \upsilon_{ix}\eta\frac{da}{dx} \tag{C.14}$$

$$T_e = T_c(x)\tau(\eta) \tag{C.15}$$

$$n_e\upsilon_{ix} = \nu\frac{\dot{N}}{\pi a^2}f(\eta) \tag{C.16}$$

where $\dot{N}$ is the net particle flow ($\dot{N} = I_b/e$ if I_b is the beam ion current), and ν is a constant selected so as to satisfy overall conservation:

$$\frac{1}{2\nu} = \int_0^\infty \eta f(\eta)d\eta \tag{C.17}$$

Substituting equations (C.13) through (C.15) into equations (C.11) and (C.12), we obtain:

$$m_i\frac{au_c}{T_c}\frac{d}{dx}\left(u_c\frac{da}{dx}\right) = C_1 \tag{C.18}$$

$$\frac{\tau}{y^2} = 1 + \frac{C_1}{C_2}\eta^2 \tag{C.19}$$

where C_1 and C_2 are constants to be determined later.

Performing this analysis to the limit $\frac{a}{a_o} \gg 1$ or $\frac{T_c}{T_{co}} \ll 1$, it can be shown that:

$$u_c(x) \approx u_{co} \tag{C.20}$$

$$C_2 = 2k\gamma\left(1 + \frac{T_i}{T_e}\right) \tag{C.21}$$

$$\frac{T_c}{T_{co}} = \left(\frac{a}{a_o}\right)^{-2(\gamma-1)} \tag{C.22}$$

C.4 Width Variation and the Radial Profiles

Neither C_1 nor the exact value of a have been defined so far. However, from equation (C.18), their definition is in fact arbitrary up to a constant factor: if C_1 were made N times larger, while defining $a(x)$ to be $\sqrt{N}$ larger everywhere, equation C.18 would not change. Looking at equation (C.19), a clean and convenient choice of the ratio of C_1/C_2 is unity:

$$C_1 = C_2 = 2k\gamma\left(1 + \frac{T_i}{T_e}\right) \tag{C.23}$$

Substituting C_1 into equation (C.18) and using the "asymptotic" approximation $u_c(x) = u_{co} = const$, the first integral of equation (C.18) is obtained and rearranged:

$$\frac{\mathrm{d}a}{\mathrm{d}x} = \sqrt{s^2 - \frac{2\left(1 + \frac{T_i}{T_e}\right)}{(\gamma - 1)M_{co}^2}\left[1 - \left(\frac{a}{a_o}\right)^{-2(\gamma-1)}\right]} \tag{C.24}$$

where s^2 is a constant of integration, whose meaning is the limiting slope for $\frac{a}{a_o} \to \infty$:

$$s = \left(\frac{\mathrm{d}a}{\mathrm{d}x}\right)_\infty \tag{C.25}$$

However, we observe that, in consistency with the asymptotic approximation for u_c, we should simply retain the part $\frac{\mathrm{d}a}{\mathrm{d}x} \approx s$. Therefore, neglecting a_o, we obtain:

$$a(x) = sx \tag{C.26}$$

with $\frac{C_1}{C_2} = 1$, the radial profile shapes are defined by

$$\begin{cases} -\dfrac{\gamma}{\gamma - 1}\left(1 + \dfrac{T_i}{T_e}\right)k\dfrac{\tau'}{y^2\eta} = 2k\gamma\left(1 + \dfrac{T_i}{T_e}\right) \\ \dfrac{\tau}{y^2} = 1 + \eta^2 \end{cases} \tag{C.27}$$

Therefore, it can be shown that

$$y = \frac{1}{(1+\eta^2)^{\gamma/2}} \tag{C.28}$$

$$\tau = \frac{1}{(1+\eta^2)^{\gamma-1}} \tag{C.29}$$

$$\frac{n_e}{n_{ec}} = \frac{1}{1+\eta^2} \tag{C.30}$$

Equation (C.30) provides the simplest interpretation of the variable $a(x)$: when $\eta = 1$ ($r = a(x)$), we have $n_e = \frac{n_{ec}}{2}$, namely, $a = sx$ represents the radial location at which density falls to half the centerline value at the same x.

Another useful relationship, from $\tan\theta = \frac{r}{x}$, is

$$\tan\theta_{1/2} = \frac{a}{x} = s \tag{C.31}$$

i.e., s represents the tangent of the angle for half-density.

The axial flux profile shape is

$$f(\eta) = y\tau^{\frac{1}{\gamma-1}} = \frac{1}{(1+\eta^2)^{1+\frac{\gamma}{2}}} \tag{C.32}$$

Substituting equation (C.32) into equation (C.17), the normalization factor, ν, is obtained:

$$\nu = \frac{\gamma}{2} \tag{C.33}$$

In many cases, flux or current density are measured with a Faraday probe placed perpendicular to the incoming ion flow. The measured quantity is then

$$j_i = en_e\sqrt{\upsilon_{ix}^2 + \upsilon_{ir}^2} = en_e\upsilon_{ix}\sqrt{1 + \left(\frac{\upsilon_{ir}}{\upsilon_{ix}}\right)^2} \tag{C.34}$$

Using equations (C.14) and (C.16) into equation (C.34):

$$j_i = \nu\frac{e\dot{N}}{\pi a^2}f(\eta)\sqrt{1 + \eta^2\left(\frac{da}{dx}\right)^2} \tag{C.35}$$

Equation (C.35) can be simplified since we know that

$$\sqrt{1 + \eta^2\left(\frac{da}{dx}\right)^2} = \sqrt{1 + \left(\frac{r}{a}\right)^2\left(\frac{a}{x}\right)^2} = \frac{1}{\cos\theta} \tag{C.36}$$

and so, using equations (C.32) and (C.33),

$$j_i = \gamma\frac{e\dot{N}}{2\pi a^2\cos\theta}\frac{1}{(1 + \eta^2)^{1 + \frac{\gamma}{2}}} \tag{C.37}$$

Also, $a^2 = s^2x^2 = s^2R^2\cos^2\theta$, and $e\dot{N} = I_b$ is the beam current, the current density can be rewritten as:

$$\begin{cases} j_i = \dfrac{j_{ic}(R)}{\cos^3\theta\left(1 + \dfrac{\tan^2\theta}{\tan^2\theta_{1/2}}\right)^{1 + \gamma/2}} \\ j_{ic} = \dfrac{\gamma I_b}{2\pi R^2\tan^2\theta_{1/2}} \end{cases} \tag{C.38}$$

It is to be noted here that the theory does not determine the slope s (or $\theta_{1/2}$). Equation (C.38) suggests an experimental way to extract $\theta_{1/2}$ from current density data, which at the same time provides a check on the validity of the theory: Plot (for a given R) the quantity $\left(\dfrac{j_{ic}}{j(\theta)\cos^3\theta}\right)^{2/(2+\gamma)}$ versus $\tan^2\theta$, the plot should a straight line, where slope is $\dfrac{1}{\tan^2\theta_{1/2}}$.

Of course, if instead one had a set of plasma density data $n_e(\theta,R)$, equation (C.30), in the form

$$\frac{n_{ec}}{n_e} = 1 + \frac{\tan^2\theta}{\tan^2\theta_{1/2}} \tag{C.39}$$

would provide an alternative determination of $\theta_{1/2}$.